Award Number: W81XWH-15-1-0571

TITLE: Prostate Cancer Grade Mapping with Transrectal Electrical Impedance Tomography

PRINCIPAL INVESTIGATOR: Ryan Halter

CONTRACTING ORGANIZATION: Trustees Of Dartmouth College
Hanover Nh 03755-4099

REPORT DATE: October 2018

TYPE OF REPORT: Annual

PREPARED FOR: U.S. Army Medical Research and Materiel Command
Fort Detrick, Maryland 21702-5012

REPORT DOCUMENTATION PAGE

Form Approved
OMB No. 0704-0188

1. REPORT DATE	2. REPORT TYPE	3. DATES COVERED
October 2018	Annual	15SEP2017 - 14SEP2018

4. TITLE AND SUBTITLE

Prostate Cancer Grade Mapping with Transrectal Electrical Impedance Tomography

5a. CONTRACT NUMBER

5b. GRANT NUMBER
W81XWH-15-1-0571

5c. PROGRAM ELEMENT NUMBER

6. AUTHOR(S)
Ryan Halter/Kofi Odame

E-Mail: ryan.halter@dartmouth.edu, kofi.odame@dartmouth.edu

5d. PROJECT NUMBER

5e. TASK NUMBER

5f. WORK UNIT NUMBER

7. PERFORMING ORGANIZATION NAME(S) AND ADDRESS(ES)

Trustees of Dartmouth College Office of Sponsored Projects 11 Rope Ferry Road #6210 Hanover, NH 03755-1404

8. PERFORMING ORGANIZATION REPORT NUMBER

9. SPONSORING / MONITORING AGENCY NAME(S) AND ADDRESS(ES)
U.S. Army Medical Research and Materiel Command
Fort Detrick, Maryland 21702-5012

10. SPONSOR/MONITOR'S ACRONYM(S)

11. SPONSOR/MONITOR'S REPORT NUMBER(S)

12. DISTRIBUTION / AVAILABILITY STATEMENT
Approved for Public Release; Distribution Unlimited

13. SUPPLEMENTARY NOTES

14. ABSTRACT

The primary objective of this research is to combine advanced integrated electronics with transrectal electrical impedance tomography (TREIT) and electrical impedance sensing biopsy (EIS-Bx) devices to improve TRUS-guided prostate biopsy procedures and help to address the challenge of distinguishing aggressive from indolent disease in men newly diagnosed with prostate cancer. The novelty in this program falls into two categories: 1) we aim to couple our single point EIS-Bx measurement device with an array of electrodes adhered to a standard *end-fired* TRUS probe (Halter's team) and 2) we aim to develop a custom application specific integrated circuit (ASIC) that will enable us to measure these electrical properties over a *wide frequency range* (optimal for discriminating high from low-grade prostate cancer) and *at high frame rates* (required for real-time prostate biopsy procedures) (Odame's team). During the third year of this program we have continued to 1) optimize and validate our initial ASIC device and small form-factor EIT system, 2) optimize finite element method meshing approaches and reconstruction algorithms for imaging the electrical properties of prostate during an TREIT + EIS-Bx procedure, 3) conducted phantom and ex vivo animal tissue studies in preparation for ex vivo prostate studies, and 4) completed submission and received approval for human subjects testing. Over the next year, our plans are to primarily focus on conducting the ex vivo prostate study, while continuing to optimize the hardware and image reconstruction algorithms.

15. SUBJECT TERMS
NONE LISTED

16. SECURITY CLASSIFICATION OF:			17. LIMITATION OF ABSTRACT	18. NUMBER OF PAGES	19a. NAME OF RESPONSIBLE PERSON
a. REPORT	b. ABSTRACT	c. THIS PAGE			USAMRMC
U	U	U	UU	98	19b. TELEPHONE NUMBER *(include area code)*

Table of Contents

	Page
Introduction	**2**
Body	**3**
Key Research Accomplishments	**8**
Reportable Outcomes	**8**
Conclusion	**9**
Appendices	**10**
Appendix 1: IEEE TMI Publication	**11**
Appendix 2: Phys Meas Murphy Publication	**22**
Appendix 3: IEEE Trans BIOCAS Publication	**36**
Appendix 4: Phys Meas Murphy Submission	**46**
Appendix 5: Phys Meas Rao Submission	**62**
Appendix 6: BMES Abstract – Fused-data EIT	**77**
Appendix 7: BMES Slide Deck – Fused-data EIT	**78**
Appendix 8: EIT Conference Abstract – Fused Data	**85**
Appendix 9: EIT Conference Abstract – EIT/US Muscle	**86**
Appendix 10: SPIE Conference Paper – EIT-biopsy	**87**

INTRODUCTION

No clinical test or imaging modality is currently able to accurately discriminate between aggressive and indolent prostate cancer. As a result, there are a significant number of men unnecessarily treated with radical, life-altering, therapies including external beam radiation, brachytherapy, and radical prostatectomy. The primary reason for this is that the definitive method for diagnosing prostate cancer and determining treatment strategies depends primarily on histological assessment of tissue cores obtained during a transrectal ultrasound (TRUS) guided biopsy; a *typical procedure extracting 12 cores samples less that 0.5% of a typical prostate gland (~50cc)*. Because of the small volume of tissue sampled, it is difficult to determine with certainty how aggressive or indolent the disease is.

Electrical properties of tissue are largely morphology dependent. We have shown significant ($p<0.001$) electrical property contrast between benign and malignant prostate in a number of published studies. This contrast arises because of large structural difference in tissue architecture between benign and malignant tissues. We have also shown significant electrical property differences between cancers of different Gleason grades. The sensitivity (SN) and specificity (SP) for distinguishing high (Gleason score > 7, SN=0.93, SP=0.81) and low (Gleason score < 7, SN=0.7, SP=0.8) prostate cancers are similar to that of magnetic resonance imaging based alternatives, currently the most promising technologies for grading disease.

This program is focused on enhancing a standard clinically used TRUS-guided biopsy procedure by imaging the electrical properties of prostate. The hypothesis is that these electrical property images will provide surrogate measures of disease aggressiveness. Our specific objective is to couple a dual-modality TRUS and electrical impedance tomography (EIT) system with an electrical property sensing biopsy instrument to better guide biopsy sampling and to provide improved staging criteria with more specific imaging studies. This program is specifically designed to augment clinically accepted devices (TRUS-guided biopsy) with the aim of rapidly translating this highly cancer specific technology to the clinic.

Much of the third year of this program has continued to focus on optimizing and validating our hardware systems (electrode array, custom biopsy needles, instrument tracking), optimizing the protocol used to capture TRUS images and produce anatomically accurate meshes of the prostate, further optimization of image reconstruction algorithms for prostate imaging, and optimizing our custom ASIC device and integrating into a small form-factor benchtop system specifically designed for transrectal EIT (TREIT) imaging of the prostate. In addition we submitted and received approval for our human subjects protocol. The final year of this program will primarily focus on conducting the ex vivo study. In addition, we will continue to optimize hardware and reconstruction algorithms through additional phantom experiments. Finally, we will continue to prepare publications and proposals focused on our technical developments and clinical data acquisition and evaluation.

BODY

The following research summary is presented in terms of the approved Statement of Work, with each task being discussed separately. Detailed discussion of developments over the past year can be referenced in the manuscripts published, submitted, or in preparation which are provided in the Appendix. All tasks have been accomplished at Dartmouth College's Thayer School of Engineering. Major Tasks are marked as KO (Kofi Odame) or RH (Ryan Halter) to denote the responsible PI. Note that future task and objectives to be completed are marked as **TBC**.

SPECIFIC AIM 1: TO DEVELOP NOVEL TREIT HARDWARE FOR PROSTATE IMAGING

Major Task 1: Design and fabricate an ASIC for EIT applications (KO)

a) Design and fabricate ASIC v1 w/ ADC, current drive, and multiplexing
Completed in 2015-16 reporting period.

b) Design and fabricate an optimized ASIC v2 w/ additional digital control circuitry
Completed in 2016-17 reporting period.

Task 1 Milestones:

1. *ASIC v1 designed and fabricated –* ***Completed***
2. *ASIC v2 designed and fabricated –* ***Completed***
3. *First complete ASIC (v2) optimized for EIT –* ***Completed***

Major Task 2: Integrate EIT-ASIC into a complete small form-factor EIT system (KO)

a) Design small form-factor PCB to house the ASIC and support circuitry.
Completed in 2016-17 reporting period.

b) Write microcontroller code to control small form-factor EIT system
Completed in 2016-17 reporting period.

c) Write LabView code to communicate between EIT-system and laptop
Completed in 2016-17 reporting period.

d) Construct an enclosure to house the EIT system integrated to the TRUS probe
Enclosure will be constructed after the electronics of the 20 channel system have been validated. The dimensions of the envisioned enclosure are: 5.5"(W) x 8.25"(L) x 3.25" (H) (see Fig. 1).

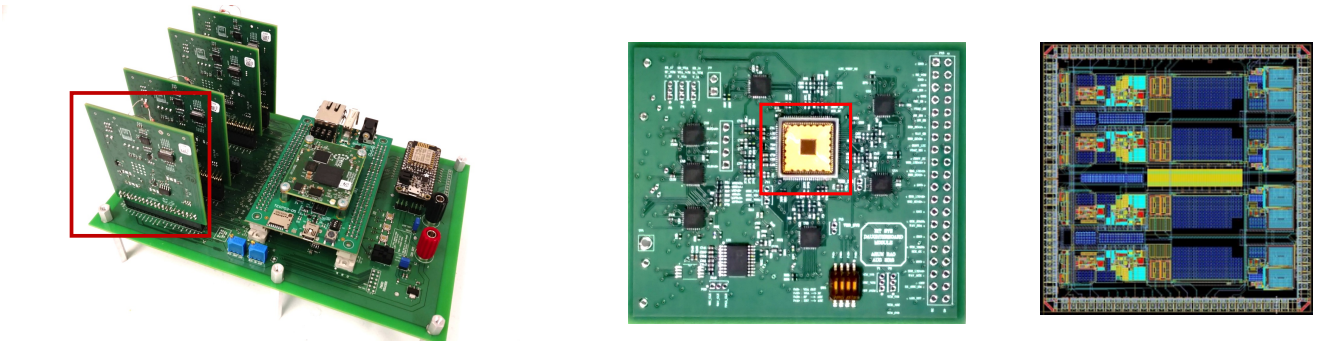

(a) **(b)** **(c)**

Figure 1: (a) Miniaturized EIT system. Photograph depicts horizontal motherboard and 4 of the 5 daughter boards (red border) that comprise the system. Total dimensions are 5.5"(W) x 8.25"(L) x 3.25" (H) (b) Detail of daughter board, showing 4-channel ASIC (red border) and peripheral components. (c) Internal layout of ASIC, showing 4 channels of analog/mixed-signal circuitry for current injection and voltage readout.

Task 2 Milestones:

1. *Fully functional small form-factor EIT system (month 18)* ***– Completed, minus enclosure***

Major Task 3: Validate ASIC-based EIT system (KO)

a) Bench-top electrical evaluate of ASIC v1
Completed in 2015-16 reporting period.

b) Bench-top evaluation of ASIC v2
Completed in 2016-17 reporting period.

c) Bench-top evaluation of small form-factor ASIC-based EIT system
The system has been evaluated using standard electrical metrics and phantom imaging to demonstrate potential of using this device for EIT. As an example, end-to-end evaluation of small form-factor ASIC based system was performed to measure the signal-to-noise ratio (SNR) of the system. Figure 2 depicts SNR for two representative channels, from 200 Hz to 1 MHz. Details regarding full system evaluation can be found in Appendix 5.

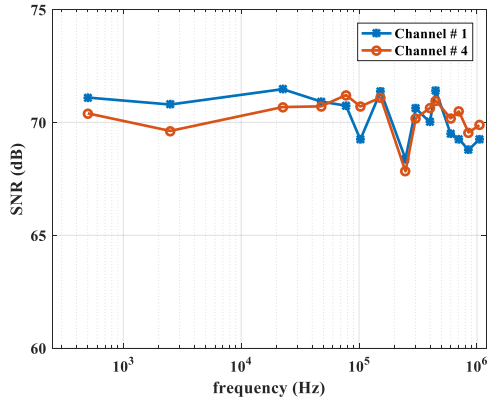

Figure 2: One of the main system specification requirements of an EIT device is the precision, or signal-to-noise ratio (SNR). We measure the SNR of the ASIC by performing hundreds of load impedance measurements under nominally-identical conditions. The SNR is calculated as the ratio of the mean squared over the variance of these repeated measurements.

Task 3 Milestones:

1. *Validation that our small form-factor ASIC-based EIT system provides sufficient electrical characteristics to enable EIT imaging* ***– Mostly complete, final validation is TBC***
2. *1 peer-reviewed publication submitted* ***– Completed, See Appendix 3 & 5***

SPECIFIC AIM 2: TO DEVELOP TREIT IMAGING ALGORITHMS FOR PROSTATE IMAGING
Major Task 1: Optimize and manufacture TREIT electrode arrays and EIT-Bx needles (RH)

a) Design, fabricate, and evaluate TREIT electrodes arrays
Completed in 2015-16 reporting period.

b) Construct EIS-Bx needles
Primary tasks completed in 2015-16 reporting period.
We have continued to fabricate more EIS-Bx needles over the past year. In addition, we have developed a novel 8-electrode EIS-Bx needle (as compared to the 4-electrode device we have used in the past) (Figure 3). The four additional electrodes provide more intraprostatic measurements, which helps to improve accuracy of image reconstruction. We will be using this 8-electrode device for our ex vivo study during the final year of this program.

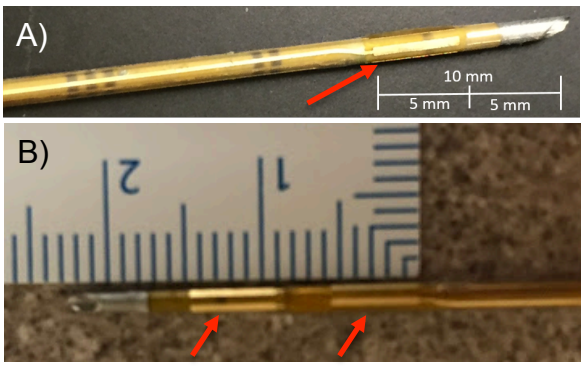

Figure 3: A) shows four-electrode biopsy needle we have typically been using. B) shows additional row of four electrodes added to the biopsy needle for addition intraprostatic measurements. Red arrows point to the electrode arrays.

Task 1 Milestones:

1. *TREIT electrode arrays fabricated for use in phantom and ex vivo experiments* ***– Completed (additional electrode arrays will be fabricated as needed for the remainder of this project)***

2. *EIS-Bx needles fabricated for use in phantom and ex vivo experiments.* – ***Completed (additional EIS-Bx devices will be fabricated as needed for the remainder of this project)***

Major Task 2: Develop 3D prostate meshing through EM-tracked TRUS (RH)

a) Integrate EM tracking with TRUS image acquisition
Completed in 2015-16 reporting period.

b) Write software to extract prostate point cloud from 3D tracked US images
Completed in 2015-16 reporting period.

c) Developing meshing algorithms to create 3D prostate mesh for TREIT reconstruction
Completed in 2015-16 reporting period.

Task 2 Milestones:

1. *Hardware and software capable of producing a 3D FEM mesh of the prostate based on EM-tracked TRUS images* ***– Completed***

Major Task 3: Customize image reconstruction software for TREIT-based prostate biopsy (RH)

a) Write code to specify EIS-Bx needle electrodes within the 3D prostate mesh
Completed in 2016-17 reporting period.
While already completed, we have continued to optimize our tracking approach to ensure we can accurately identify the needle location during biopsy. We have designed a new 3D printed housing to hold the biopsy needle and are tracking both the TRUS probe and Biopsy needle (Figure 4).

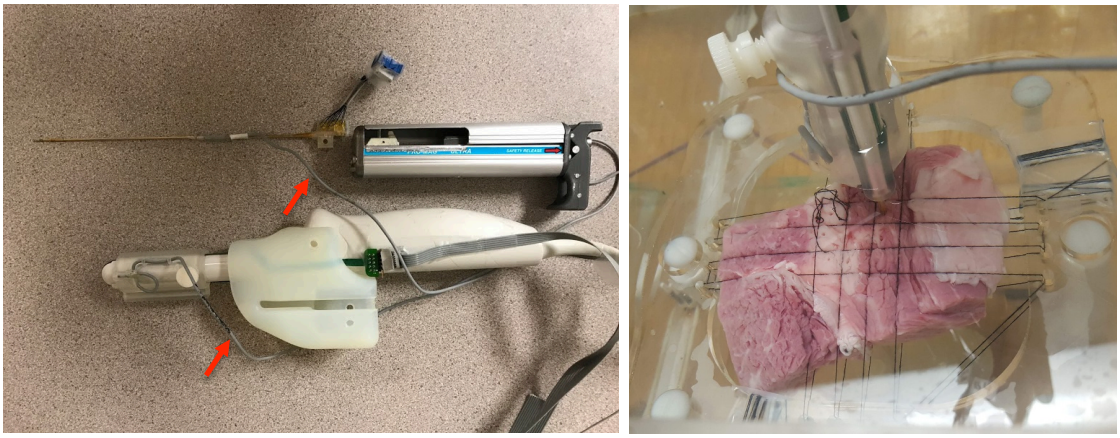

Figure 4: Left) Rigid housing coupled to TRUS probe to ensure accurate placement of biopsy needle relative to the TRUS probe. This configuration is being used for our ex vivo data collection. Gray single-core wires (red arrows) leaving biopsy needle and tip of TRUS probe are interfaced to our EM tracker. Right) Example imaging session of the probe being used to record data from an ex vivo bovine tissue sample.

b) Write code to couple probe surface and EIS-Bx electrodes in TREIT reconstructions
Completed in 2016-17 reporting period.

c) Validate the new meshing and reconstruction algorithms through software simulations
Completed in 2016-17 reporting period.

Task 3 Milestones:

1. *Validation of mesh generation code and TREIT + EIS-Bx image reconstruction code* ***– Completed***
2. *1 peer-reviewed publication submitted* ***– Completed – manuscript published in Physiological Measurement (Appendix 2, 6, 7, 8)***

Major Task 4: Submit documents for IRB and MRMC HRPO approval (RH)

a) Draft and submit IRB protocol revisions for ex vivo study
We received Dartmouth IRB approval in Spring 2018

b) Draft and submit documentation for MRMC HRPO approval
We received MRMC HRPO approval in Summer 2018

Task 4 Milestones:

1. *Obtain IRB and MRMC HRPO approval for ex vivo cohorts* ***– Completed***

SPECIFIC AIM 3: TO VALIDATE TREIT THROUGH PHANTOM STUDIES

Major Task 1: Evaluate TREIT through use of liquid phantoms (RH)

a) Construct a tank for phantom studies
Completed in 2015-16 reporting period.

b) Perform saline based phantoms with bench-top EIT system (software validation)
Completed in 2016-17 reporting period.

c) Perform saline-based phantoms with new small form-factor EIT system (hardware validation)
While the small form-factor EIT system continues to be under development, we have been leveraging our previously developed EIT system to carry out these saline phantom experiments.

Task 1 Milestones:

1. *Validation that meshing and image reconstruction software functions as expected* ***– Completed***
2. *Validation that ASIC-based small form-factor EIT system performs better than bench-top EIT systems* ***– TBC (once hardware is fully integrated)***

Major Task 2: Evaluate TREIT through use of anatomically accurate phantoms (KO/RH)

a) Perform anatomically accurate phantom imaging with bench-top EIT system (software validation)
We have performed several anatomically accurate phantom studies using gelatin prostates with multiple inclusions. These have been presented at the International Conference on Biomedical Applications of Electrical Impedance Tomography (Appendix 8) and the 2018 Biomedical Engineering Society Annual meeting (Appendix 6 & 7). An additional manuscript to be submitted to IEEE Transactions of Medical Imaging is currently in preparation. We have also conducted several imaging session using ex vivo bovine tissue containing both adipose and muscle tissue in preparation for ex vivo prostate imaging (Figure 5).

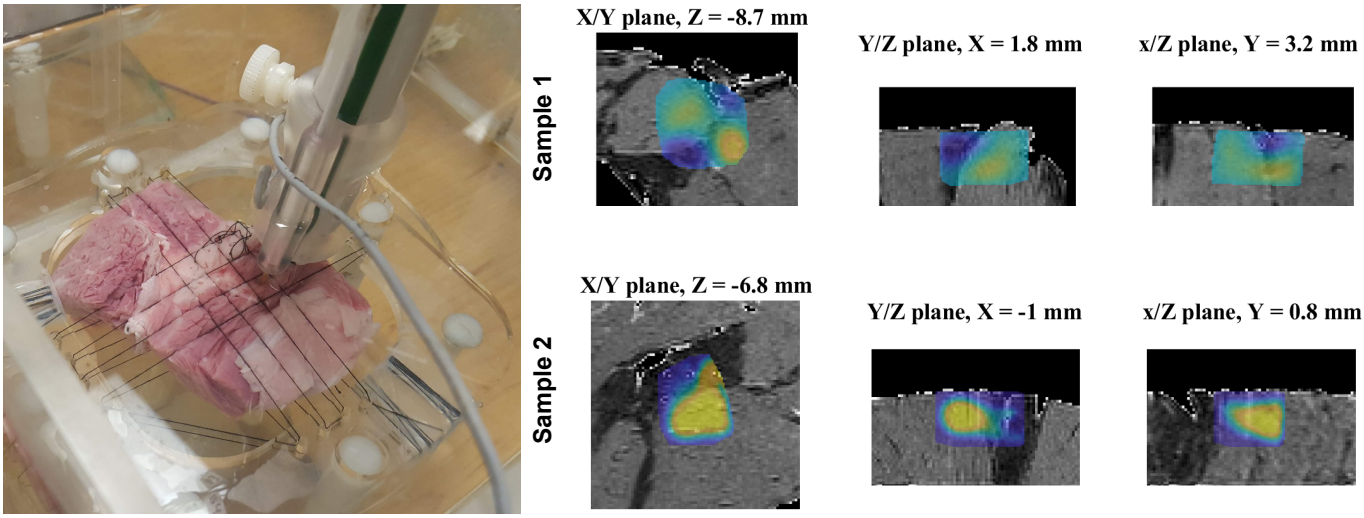

Figure 5: Left) Ex vivo bovine tissue imaging configuration. The thin electrical transparent cables secure the tissue in place. The square grid (created by the cables) indicates where biopsy cores are extracted. The TRUS probe and biopsy needle guide are placed right above the tissue. The tissue samples is submerged within a bath of 0.1 S/m saline solution to mimic the tissue surround this prostate. Right) Magnetic Resonance (MR) images are acquired of the tissue sample and registered with EIT imaging. Two tissue samples were images on different days (Sample 1 and Sample 2). The conductivity maps are overlaid (blue/yellow) regions on the MR images. These results are very promising and highlight the strong adipose/muscle contrast visible in EIT images (yellow = muscle, blue = adipose). Note the concordance between MR muscle regions (gray) and high conductivity (yellow) regions in the EIT images and the MR adipose regions (black) and low conductivity (blue) regions in the EIT images.

b) Perform anatomically accurate phantom imaging with new small form-factor EIT system (hardware validation)

While the small form-factor EIT system continues to be under development, we have been leveraging our previously developed EIT system to carry out these phantom experiments. We will use our previously developed EIT system to carry out our ex vivo studies.

Task 2 Milestones:

1. *Validation of EIS-Bx + TREIT + TRUS procedure that will ultimately be used in ex vivo studies* – ***Completed***
2. *Validation that meshing and image reconstruction software functions as expected* – ***Completed***
3. *Validation that ASIC-based small form-factor EIT system performs better than bench-top EIT systems* – ***TBC (once hardware is fully integrated)***

SPECIFIC AIM 4: TO EVALUATE TREIT USING A SAMPLE OF EX VIVO PROSTATES

Major Task 1: Evaluate TREIT/EIT-Bx in a cohort of ex vivo prostates (RH)

a) Record TRUS/TREIT (+ EIS-Bx) images of *ex vivo* prostates

This step is in progress. To date we have collected data from 3 prostates. We expect to record data from ~1 prostate per week over the next 6 months in order to meet our recruitment objective of 25 ex vivo prostates. Figure 6 shows an example of an ex vivo prostate in our custom tank and details the orientation and core locations that will be used for analysis. This information is being use by pathology to ensure accurate mapping between electrical impedance images and pathological metrics for the study. In addition, we are capturing an MRI image of each prostate (similar to our ex vivo bovine tissue protocol described above). This will help to ensure accurate registration between pathology, MR, ultrasound, and EIT data and images.

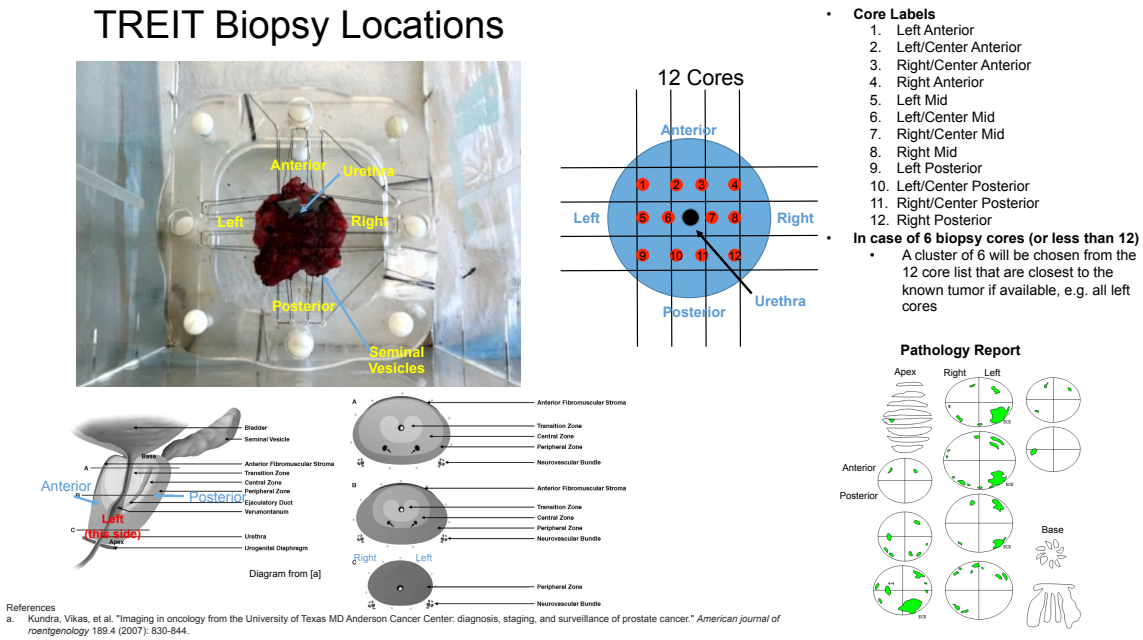

Figure 6: Ex vivo prostate positioned within our imaging tank. Core location description defined and anatomic configuration specified. Example pathology map to be generated for each ex vivo prostate. This approach was developed and refined over the past year and will be used for remaining prostates as part of our ex vivo protocol.

b) Perform post-imaging pathological assessment of ex vivo prostates and biopsy cores

To be completed during final year of this program

c) Statistically analyze TREIT-based images and pathological metrics

To be completed during final year of this program

Task 1 Milestones:

1. *Preliminary clinical statistics defining utility of TREIT+EIS-Bx combined with TRUS* – ***TBC***
2. *Initial parameter threshold values for use in detecting and staging prostate cancer* – ***TBC***
3. *1 peer-reviewed publication submitted* – ***TBC***

KEY RESEARCH ACCOMPLISHMENTS (over the past year)

- Developed a new 8-electrode biopsy needle to provide additional intraprostatic electrical property measurements and incorporated this new device into our imaging algorithms
- Designed and fabricated a 20-channel version of the small form-factor EIT system. End-to-end functionality has been validated, and phantom testing continues to be underway.

- Further optimized our data acquisition (EM-tracking, EIT data collection) for use in phantoms and the ex vivo study planned for this year.

- Demonstrated strong concordance between MR and EIT images in ex vivo bovine tissue samples in preparation for ex vivo prostate study to take place this year.

- Published and submitted several manuscripts and conference abstracts associated with hardware development and EIT imaging for this prostate application (as well as other applications that have been realized as a results of the developments made as part of this effort)

REPORTABLE OUTCOMES

Manuscripts

Murphy EK, Skinner J, Martucci M, Rutkove S, Halter RJ, "Towards Electrical Impedance Tomography Coupled Ultrasound Imaging for Assessing Muscle Health," IEEE TMI, *accepted December 2018.* (doi: 10.1109/TMI.2018.2886152) ***(Appendix 1 – accepted)***

Murphy EK, Wu X, Halter RJ, "Fused-data transrectal EIT for prostate cancer imaging," Physiological Measurement, 39(5): 054005, May 2018 (doi: 10.1088/1361-6579/aabf22) ***(Appendix 2 – published)***

Rao A, Teng YC, Schaef C, Murphy EK, Arshad A, Halter RJ, Odame KM, "An Analog Front End ASIC for Cardiac Electrical Impedance Tomography," IEEE Trans. BioCAS, 12(4): 729-738, 2018 (doi: 10.1109/TBCAS.2018.2834412) ***(Appendix 3 – published)***

Murphy EK, Amoh J, Arshad SH, Halter RJ, Odame K, "Noise-robust Bioimpedance Approach for Cardiac Output Measurement," Physiological Measurement, submitted December 2018. ***(Appendix 4 – submitted)***

Rao A, Murphy EK, Shahghasemi M, Odame KM, "Current Conveyor Based Wide-band Current Driver for Electrical Impedance Tomography," Physiological Measurement, submitted December 2018. ***(Appendix 5 – submitted)***

Presentations/Abstracts

Halter RJ and Murphy EK "Multimodal Electrical Impedance Tomography (EIT): Advances in EIT-coupled Ultrasound Imaging," Invited Symposium Participant: Recent innovations and new health-related applications of electrical bioimpedance at 40th International Conf IEEE EMBS July, 2018.

Murphy E, Wu X, Halter RJ "Fused-data Transrectal Electrical Impedance Tomography for Prostate Cancer Imaging," BMES Annual Meeting, October 18, 2018.

Murphy EK, Skinner J, Martucci M, Rutkove S, Halter RJ, "A Coupled US/EIT System for Assessing Muscle Health", EIT conference 2018, University of Edinburgh, June 2018

Murphy EK, Wu X, Halter RJ, "Absolute Phantom Reconstructions using Fused-Data EIT," EIT conference 2018, University of Edinburgh, June 2018

Everitt A, Manwaring P, Halter RJ. "A real-time 4-bit imaging electrical impedance sensing biopsy needle for prostate cancer detection", Proc. SPIE Medical Imaging 2018: Biomedical Applications in Molecular, Structural, and Functional Imaging, Houston, TX, February 10-15, 2018.

CONCLUSIONS

It is a daily challenge for clinicians to determine whether a man recently diagnosed with prostate cancer has aggressive disease requiring immediately radical therapy or indolent disease requiring a more passive watchful waiting or active surveillance approach. This program is focused on developing Transrectal Electrical Impedance Tomography (TREIT) specifically for prostate imaging. Over the past year we have further explored and optimized both the hardware and image reconstruction algorithms developed in the first three years of this program to better characterize and improve the resolution and accuracy of TREIT. A novel 8-electrode biopsy needle has been developed to improve imaging accuracy. A number of more complex, anatomically accurate phantom and ex vivo tissue studies have been conducted to demonstrate feasibility of image acquisition and to validate and refine our image reconstruction algorithms. Finally, we have implemented the initial bench-top EIT system we envision using for data acquisition in clinical study to follow this program and we demonstrated its capabilities for EIT imaging through phantom studies. Over the course of the next year, we will be focusing on completing the ex vivo clinical study to evaluate this approach for prostate cancer detection and grading. In addition, we will continue to refine and optimize our hardware and image reconstruction algorithms.

APPENDICES

Appendix 1: IEEE TMI Publication
Appendix 2: Phys Meas Murphy Publication
Appendix 3: IEEE Trans BIOCAS Publication
Appendix 4: Phys Meas Murphy Submission
Appendix 5: Phys Meas Rao Submission
Appendix 6: BMES Abstract – Fused-data EIT
Appendix 7: BMES Slide Deck – Fused-data EIT
Appendix 8: EIT Conference Abstract – Fused Data
Appendix 9: EIT Conference Abstract – EIT/US Muscle
Appendix 10: SPIE Conference Paper – EIT-biopsy

Towards Electrical Impedance Tomography Coupled Ultrasound Imaging for Assessing Muscle Health

Ethan K. Murphy, Joseph Skinner, Maria Martucci, Seward B. Rutkove, and Ryan J. Halter

***Abstract*—This study establishes for the first time that a coupled Ultrasound (US) and Electrical Impedance Tomography (EIT) system can serve as a non-invasive, spatially-localized approach to extract clinically-relevant muscle properties. The US/EIT system represents a potential enhancement to Electrical Impedance Myography (EIM), which has shown promise as a non-invasive technology that may have important clinical use in indicating neuromuscular disease status and as a diagnostic tool. A 2.5D EIT algorithm evaluated on simulation, measured phantoms, and measured patient data was studied to evaluate US/EIT's ability to distinguish different aspects of muscle tissue. Simulated and phantom experiments revealed depths of distinguishability of 3.2 and 4.2 mm in simulation for 10% and 20% changes in muscle properties, respectively, and 3.6 mm in measured phantom experiments assuming a 12% muscle conductivity change. Reconstructions from patient data established that there were consistent differences 1) between longitudinal (along) and transverse (across) muscle conductivity reconstructions at frequencies of 40 and 80 kHz, and 2) side-by-side comparison between healthy and diseased tissue in terms of conductivity, permittivity, and phase at 40 and 80 kHz. Comparisons were made between the EIT reconstructed values and electrical impedance spetroscopy (EIS) measurements (an available surrogate in place of standard EIM measurements) made with the US/EIT system, wherein 1) EIS and EIT show similar sensitivity to longitudinal and transverse differences and 2) EIT showed a more consistent ability to differentiate healthy and diseased tissue. These results suggest that US/EIT appears very promising for non-invasive and spatially localized diagnosis of muscle health.**

***Index Terms*— Data fusion, electrical impedance tomography, electrical impedance myography, inverse problem.**

I. Introduction

Electrical impedance myography (EIM) is a non-invasive, painless method that assesses muscle health through measurement of broadband electrical impedance signatures. EIM studies using four-electrode linear arrays have noninvasively quantified healthy muscle anisotropy below the skin and adipose-tissue layer [1], and demonstrated significant impedance phase differences between healthy and diseased muscle for amyotrophic lateral sclerosis, myopathies, and radiculopathy [2]. Its noninvasive nature makes EIM attractive especially in comparison to conventional needle electromyography techniques. However, there are a number of potential limitations to EIM, such as: dependence on skin/adipose-tissue thickness, an inability to distinguish closely spaced muscle groups, and an inability to assess heterogeneity of muscle [3].

Here we describe a novel approach that couples electrical impedance tomography (EIT) with co-registered ultrasound (US) imaging with the intent of addressing and overcoming these limitations. In comparison to EIM, EIT relies on an array of electrodes, usually ranging from 16-32, to record a series of impedance measurements from numerous sets of current patterns (each current pattern is composed of a selected source and sink electrode). A reconstruction algorithm uses these measured impedances to create a complex conductivity image of the region under study. Conventional EIT reconstruction algorithms require solving a non-linear ill-posed inverse problem to estimate the spatial distribution of electrical properties within a domain partially bounded by the set of electrodes. The challenge with these problems is that the noisy and limited boundary measurements can significantly influence the estimation of the internal complex conductivity distribution. The coupled US/EIT system developed here leverages segmented US data to constrain the EIT image reconstruction algorithm and provide a more accurate estimate of the internal electrical properties. Since EIT spatially reconstructs electrical properties it implicitly accounts for the skin/adipose-tissue layers, can potentially separate contributions from individual muscles, and provides a map of tissue heterogeneity, overcoming several of EIM's limitations.

The simulation, phantom, and pre-clinical human studies conducted here demonstrate that complex conductivity images reconstructed through use of a coupled US/EIT system can successfully capture different physiological and pathological muscle characteristics. The simulated and phantom experiments characterize the *depth of distinguishability* assuming changes in a muscle's electrical properties, i.e. the maximum depth at which muscle of two different electrical properties can be distinguished. Specifically, simulations suggest that muscle conductivity changes of 10% and 20% can be detected at depths of 3.2 and 4.2 mm, respectively, and phantom experiments demonstrate that a 12% change in conductivity can be detected at a depth of 3.6 mm.

This work was supported in part by the U.S. National Institutes of Health under Grant 1R01CA143020–01A1 and DoD Congressionally Directed Medical Research Program under Grant W81XWH-15-1-0102.

*E. K. Murphy is with the Thayer School of Engineering, Dartmouth College, Hanover, NH 03755, USA (email: ethan.k.murphy@dartmouth.edu).

R. J. Halter is affiliated with the Thayer School of Engineering and Geisel School of Medicine at Dartmouth College, Hanover, NH 03755 USA (e-mail: ryan.halter@dartmouth.edu).

US/EIT reconstructions evaluated on 46 data sets recorded bilaterally from the legs of 3 patients with radiculopathy established that there were consistent differences between 1) longitudinal (along) and transverse (across) muscle conductivity at frequencies of 40 and 80 kHz, and 2) in side-by-side comparisons conductivity, permittivity, and phase at 40 and 80 kHz for healthy and diseased muscle tissues. To the best of our knowledge, this appears to be the first reported study demonstrating these relationships using EIT. In comparison to EIT reconstructions without using US data, this coupled approach revealed substantial improvements in image accuracy and clearly demonstrates the benefit of incorporating US data. These results suggest that EIT may represent a promising approach for non-invasive, spatially localized assessment of muscle health.

A comparison between electrical impedance spectroscopy (EIS) and US/EIT is also performed, which revealed 1) EIS and EIT show similar sensitivity to longitudinal and transverse differences and 2) EIT showed a more consistent ability to differentiate healthy and diseased tissue. We do not refer to the EIS measurements as EIM measurements, because our US/EIT probe does not provide adequate electrode spacing required for standard EIM measurements. Specifically, the current-drive and voltage-measurement electrode spacing for the EIS patterns in this study were 2.1 cm and 0.7 cm, respectively, whereas the spacing for standard EIM is 6 cm and 3 cm, respectively [4]. Thus the EIS results presented here are likely less sensitive to muscle and more sensitive to skin/adipose-tissue variability than standard EIM measurements.

The paper is structured as follows. Section 2 describes the coupled US/EIT system, EIS measurements, the forward and inverse problems required for EIT image reconstruction, data collection approaches, data processing steps, metrics and additional parameters. Section 3 describes the results of the simulation, phantom, and initial in vivo human experiments. Section 4 discusses the comparisons of EIS and EIT results to EIM results from literature, and future approaches for refining the US/EIT system. We note all usages of impedance in this manuscript refer to *electrical* impedance and not *acoustic* impedance.

II. Methods

A. Coupled US/EIT System

The coupled US/EIT system consisted of a Terason t3000 ultrasound imaging system (Burlington, MA, USA) and custom-designed EIT data acquisition system [5] with a 5 to 12 MHz (12L5V) US probe and sonolucent electrode array wrapped around the active face of the US probe (Fig. 1). The electrode array included thirty 2 mm x 5 mm gold-plated electrodes printed on a 1 mil polyamide substrate with 1 mm and 2 mm spacing between electrodes. Due to limitations in the EIT system hardware, only 20 of the electrodes were used for data acquisition. The US probe was placed in a custom-designed 3D printed housing that secured the electrode array and cable in place and provided an electrode array to skin gap of 2 mm. During data acquisition, this gap was filled with US gel to ensure a uniform electrical contact between the electrodes and the skin; specifically, this limited the variation in pressure and contact area between the skin and the different electrodes since the only patient contacting point was the rim of the 3D printed housing. Minimal degradation in US image quality was observed with this additional 2 mm layer of US gel.

Electrical impedance data was recorded at 10, 20, 40, and 80 kHz using exhaustive, non-flip tetrapolar impedance patterns associated with the 20 electrodes. Each tetrapolar pattern, denoted as an IIVV pattern, is defined by the 4 electrodes involved in the impedance measurement, i.e. II represents the current injection electrode pair (I1,I2) and VV represents the differential voltage sensing pair of electrodes (V1,V2). Flip patterns consist of an IIVV pattern in which the current drive or voltage sense electrodes are interchanged, e.g. for an IIVV = [1 2 3 4], the flip patterns would include [1 2 4 3], [2 1 3 4], and [2 1 4 3]. A total of 29,070 IIVV impedance patterns were recorded for each frequency: 4-electrode combinations from 20 possible (20 choose 4) x 6 IIVV electrode orderings per combination = 29,070 patterns. All patterns were recorded in ~5.4 second per image frame with each impedance measurement based on an average of 64 wavelengths. The number of patterns actually used for image reconstruction were reduced by removing bad patterns (based on the noise filter described in [6]) and bad electrodes. Bad electrodes are defined as those electrodes in which the histogram of the difference between measured and simulated impedances for a specific electrode were qualitatively different from the expected distribution, where a 'good' distribution is represented as a single mode near zero, and a 'bad' histogram is bimodal with one mode centered away from zero. This histogram metric uncovered a consistent connection issue with electrodes 16-20. Thus only electrodes 1-15 were used (green electrodes in Fig 1D). Electrical impedance data recorded from this system can be reported as discrete EIS measurements or as complex conductivity images based on EIT reconstruction approaches.

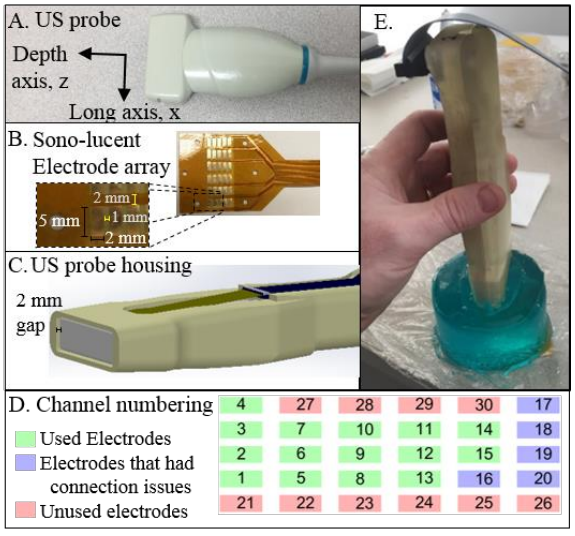

Fig. 1. A. The Ultrasound (US) probe (Terason, Inc, Burlington, MA), B. sonolucent electrode array, C. the US housing used in data collection, which provides a 2 mm gap between skin and electrodes, D. diagram showing the electrodes used, and E. US/EIT system in use for a gel phantom experiment. A mock, 3D printed, US probe was used during gel experiments.

B. EIS Measurements

All EIS measurements were collected using the same custom-designed system used for EIT-data acquisition [5]. These EIS measurements are defined as a specific set of IIVV impedances recorded at the 4 signal frequencies. The average of the following IIVV patterns were used to define a discrete or bulk EIS measurement: [1 13 5 8], [2 12 6 9], [3 11 7 10] (see Fig 1D). These patterns should provide consistent impedance values based on their similar geometry and based on our EIM experience should be minimally effected by variations of the skin/adipose-tissue layer thickness ([7]).

C. EIT Image Reconstruction

1) Forward Problem

The forward problem computes the electric potential within the domain and the electrode voltages on the boundary given a specified injected current on boundary electrodes. The complete electrode model (CEM) is used [8], based on a 3D finite element method (FEM) implementation [9]. The CEM realistically accounts for the contact impedance and shunting of electrodes. The US/EIT geometry is an open domain geometry, which is accurately modeled by expanding the modeled domain so that effectively no current flows near the open boundaries. Gmsh [10] is used to construct the 3D FEM mesh (~200k nodes and 1M elements).

2) Inverse Problem

The inverse problem is based on a standard Gauss-Newton algorithm that employs a generalized Tikhonov regularization scheme. After a linearization step ([11]) about an initial estimate of the conductivity, $\boldsymbol{\sigma}_0$, the error to be minimized, E($\delta\boldsymbol{\sigma}$), is

$$E(\boldsymbol{\delta\sigma}) = \|\mathbf{J}\boldsymbol{\delta\sigma} - \Delta\boldsymbol{v}\|_2^2 + \lambda\|\mathbf{L}(\boldsymbol{\sigma_0} + \boldsymbol{\delta\sigma} - \boldsymbol{\sigma}_{REF})\|_2^2 \quad (5)$$

where $\delta\boldsymbol{\sigma}$ is the conductivity update, **J** is the Jacobian, **L** is the regularization matrix, λ is the Tikhonov regularization factor, $\boldsymbol{\sigma}_{REF}$ is a reference conductivity, and $\Delta\boldsymbol{v}$ is the vector difference between measured, $\boldsymbol{v}_{Meas}$, and simulated voltages, $\boldsymbol{v}_{Sim}(\boldsymbol{\sigma}_0)$. The least squares solution to (5) is

$$\boldsymbol{\delta\tilde{\sigma}} = (\mathbf{J}^T\mathbf{J} + \lambda\mathbf{L}^T\mathbf{L})^{-1}(\mathbf{J}^T\Delta\boldsymbol{v} - \lambda\mathbf{L}^T\mathbf{L}(\boldsymbol{\sigma}_0 - \boldsymbol{\sigma}_{REF})). \quad (6)$$

The updated estimate of the conductivity is $\tilde{\boldsymbol{\sigma}}_1 = \boldsymbol{\sigma}_0 + \beta\boldsymbol{\delta\tilde{\sigma}}$, where β is chosen using a parabolic line-search algorithm [12]. The process is iterated to obtain an absolute reconstruction of the conductivity distribution.

The algorithm performs 2.5D reconstructions utilizing the dual-mesh method [12], which allows one to solve the Jacobian on a fine FEM mesh while estimating the conductivity on a much coarser inverse mesh. 2D reconstructions were chosen to match the dimension of the US data; this assumption is reasonable considering the minimal depth of sensitivity expected in the short axis due to the small electrode spacing along this axis (Fig. 1). The coarse mesh was 2D in the depth (z) and long axes (x) plane of the US probe (see Fig. 1A), and this was associated with a 3D fine FEM mesh that had constant conductivity values defined along the short-US probe axis (y).

The open domain is modeled in the inverse problem by constructing a mega-node (MN) consisting of all fine nodes outside of a prescribed region of interest (ROI). This ROI includes the region that heuristically has sufficient sensitivity to produce spatially varying conductivity images and a transition zone to allow for transition to the MN without effecting the inner conductivity values; see [13] for more details.

Soft Regularization: Standard Tikhonov (SR-ST). Spatial information from US imaging can be incorporated into the inverse problem through augmentation of the **L** matrix ([14]–[16]) or through incorporation into the reference conductivity, $\boldsymbol{\sigma}_{REF}$ **(**[17]**)**. Here we leverage the latter approach and refer to it as Soft Regularization: Standard Tikhonov. The reference conductivity, $\boldsymbol{\sigma}_{REF}$, is assigned a single frequency-dependent complex conductivity value from literature ([18]) for each segmented region. The regularization matrix, **L**, is defined to be a diagonal matrix with components equal to the relative maximum Jacobian value for each coarse node. Similar approaches have been used in EIT ([19], [20]) and in geophysical applications [21]. Specifically, a vector, $\boldsymbol{s}$**,** of maximum Jacobian values across all measurement patterns, N_M, for each coarse node, j, was assembled (i.e. $\mathbf{s}_j = \max_{1\le i\le N_M}(\mathbf{J}_{i,j})$). The relative sensitivity, $\boldsymbol{s}_{Rel} = \boldsymbol{s}/\max(\boldsymbol{s})$ is then used as the diagonal of **L**. This scaling penalizes large conductivity changes in high sensitivity regions, while allowing for larger conductivity changes in regions of low sensitivity. Heuristically, this approach produced images with similar spatial variation in the high sensitivity areas near to the probe surface (US gel and skin/adipose-tissue regions) to that of regions of lower sensitivity far from the probe surface (muscle) while biasing the overall reconstructed value from each region towards the values from literature.

A standard approach for EIT reconstruction (i.e. with no US data) is also considered as a means for demonstrating the benefits of US-coupled EIT. Specifically, this approach referred to as the *standard approach* uses a $\boldsymbol{\sigma}_{REF}$ vector that is identically zero and the same sensitivity-based regularization matrix used in the SR-ST approach.

D. Data Collection Approaches

Three experiments using simulated, measured phantom, and measured patient data were conducted to evaluate the potential of using US/EIT imaging for assessing muscle health.

Simulated Patient Data. Simulated data was generated from 50 segmented profiles of the US gel, skin, adipose tissue, and muscle regions extracted from patient US images. These profiles (x/z-plane) were extended in the y-axis and meshed using Gmsh to produce a 3D volumetric representation of the anatomy (assuming no spatial variation in the y-axis). Boundary voltages were simulated on this mesh by solving the 3D FEM forward problem assuming injection currents of 0.3 mA and conductivity profiles that varied only in the US imaging plane. The simulated conductivities were 0.10 S/m, 0.022 S/m, 0.024 S/m for the US gel, skin, and adipose-tissue layers, respectively. The muscle conductivities were 0.35 S/m,

0.385 S/m, and 0.42 S/m, which correspond to healthy muscle at 40 kHz [18], and a 10% and 20% increase to simulate muscle disease, respectively. The skin and adipose-tissue conductivities also corresponded to values reported at 40 kHz [18]. No noise was added to the simulated voltages, but different FEM meshes were used for simulating the voltages and performing image reconstruction to ensure no inverse crime was committed.

Measured Phantom Data. Multiple heterogeneous phantoms, consisting of stacked layers of tissue-simulating gelatin slabs, were used to evaluate the impact of skin/-adipose-tissue thickness and varying electrical properties of muscle (see Fig. 1E and Fig. 2). Phantom data consisted of 54 sets of measurements recorded from 9 skin/adipose-tissue gels ranging from 1.6 to 5.6 mm thick, 2 muscle gels, and 3 repeated measurements per gel configuration. Each repeated measurement involved removing the US/EIT probe, reapplying US gel, and placing it back on the gel phantom. The conductivities were 0.183 S/m, 0.191 S/m, 1.15 S/m and 1.02 S/m for the US gel (Sonigel), skin/adipose-tissue layer, muscle 1, and muscle 2, respectively. These conductivity values were assigned to the reference conductivity vector for SR-ST-based inversion. Drops of 0.1 S/m saline were used to remove air bubbles between gel layers. The gels were produced using a 7:1 saline to gelatin mixture (Sigma-Aldrich, 175 g Bloom strength). The thin gel layers were set in petri dishes to ensure uniform thickness. The larger conductivity values used in these experiments were chosen to maintain a large ratio between the skin/adipose-tissue layer and muscle. The conductivity ratios were smaller in this phantom work than in the simulation and patient experiments due to the minimum achievable conductivity for gel-based tissue phantoms (gel phantoms have a minimum conductivity of ~0.1 S/m even when deionized water is used as the solvent).

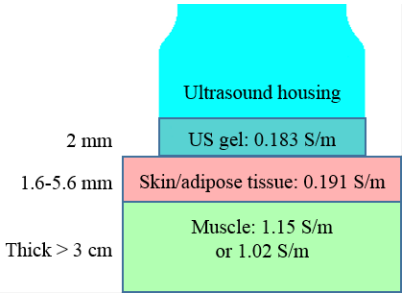

Fig. 2. Phantom experimental setup showing the US housing that has a 2 mm thick US gel (0.183 S/m) that is placed on top of skin/adipose tissue (0.191 S/m with thickness of 1.6-5.6 mm) and muscle tissue (1.15 S/m or 1.02 S/m with thickness > 3 cm).

Measured Patient Data. US/EIT data was recorded from the leg muscles on both sides of three patients with unilateral radiculopathy. The data was collected at Beth Israel Deaconess Medical Center, Boston, MA and was conducted under an IRB-approved protocol from consenting individuals. For each patient, US gel (Gamma Pharmaceutical Innovations Inc, Newark, NJ, ~0.1 S/m) was applied directly to the US probe, the electrode array was then taped down over the probe face, the US housing was installed around the US/EIT probe, and more US gel was applied in the 2 mm gap. Data acquisition was performed by Drs. Rutkove and/or Martucci. Three repeated longitudinal (in the direction of muscle fibers) and transverse measurements (across muscle fibers) were made at multiple sites on these individuals. Each repetition involved removing the US/EIT probe, reapplying US gel, and placing it back on the patient. The data was analyzed in terms of longitudinal versus transverse (similar to the analysis from [1]) and healthy versus diseased sides from each site of each individual.

E. Image and Data Processing

The US gel/skin and adipose-tissue/muscle interfaces in US images were segmented using a custom-built Matlab (MathWorks, Natick, MA) graphical user interface (Fig 3A). All segmentations were reviewed by Dr. Martucci for accuracy. The skin/adipose-tissue interface was not reliably distinguishable due to artifacts near the surface. Because skin and adipose tissue have similar conductivities (e.g. 0.22 S/m vs 0.24 S/m at 40 kHz [13]) these tissues were grouped into a single layer. The adipose-tissue/muscle interface is then linearly extended on both ends (i.e. past the left and right side of the yellow box in Fig. 3B) and encoded into a FEM mesh to account for current flowing outside the region directly below the probe face. A single coarse mesh is used (see Fig. 3B) that has increased nodal spacing as a function of distance from the electrode array (a common design for open domain geometries [22]). The coarse nodes are separated into the US gel, skin/adipose-tissue layer, and muscle regions (Fig. 3B). Further, the coarse nodes are mapped only to FEM nodes in the same region, e.g. notice the smooth top and bottom boundaries of the fine FEM mesh elements (red tetrahedra) that are associated to the skin/adipose-tissue region in Fig. 3B. To analyze the muscle properties, we computed the average nodal complex conductivity values in a region extending to a maximum depth of 10 mm and spanning the width of the US image (purple box in Fig. 3), which is a conservative estimate of where we expect to be able to produce accurate, spatially-varying reconstructions. This is based on the heuristic of estimating depth of sensitivity as half of the maximum extent of electrodes, which is 28 mm in this study (the span of electrodes 2 to 15, see Fig 1D).

F. Metrics

The average reconstructed complex conductivities were calculated for each region including the US gel layer, skin/adipose-tissue layer, and muscle region. For the patient data the repeated measurements were averaged together to improve noise characteristics. Descriptive statistics, review of example images, and comparison of individual patient imaging studies are used to evaluate the clinical potential of this imaging modality.

Within the simulation and phantom experiments, a *depth of distinguishability* was defined to evaluate how far below the surface different muscle conductivities could be detected with US/EIT. The depth of distinguishability was calculated by determining the depth at which the +/-1 SD (standard deviation) envelope of the linear fits to the different muscle reconstructions intersect. An illustration depicting the depth of distinguishability from simulation results of a 20% change in muscle conductivity shows the +/-1 SD regions (cyan and green regions) intersect at 4.6 mm (Fig. 4).

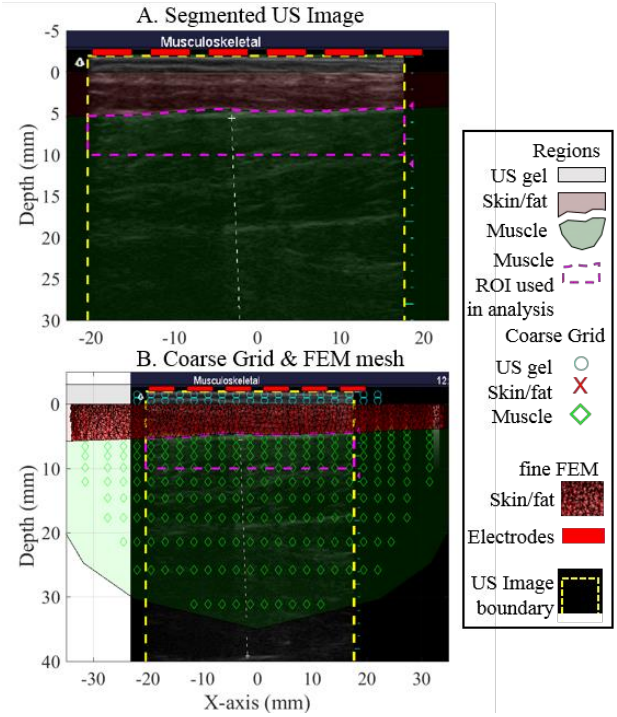

Fig. 3. A. The segmented US image where the skin/adipose-tissue layer is colored red and the muscle region is colored green, and B. the coarse nodes illustrating the reconstructed points and the separate region (US gel is cyan circles, skin/adipose tissue is red x's and muscle are green diamonds. A cross section of the segmented FEM mesh in the skin/adipose-tissue layer is shown. The yellow box shows the US image extent and the purple box is the region used for analysis of the muscle.

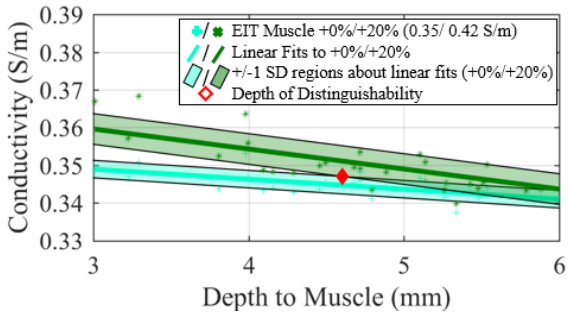

Fig. 4. Illustration of how the *depth of distinguishability* is calculated. The cyan and green boxes represent +/-1 SD regions about linear fits to two different types of muscle (+0% and +20% change). The intersection of these regions represents a depth where these two muscle property differences could be distinguished.

G. Additional Measurement Parameters

In all measured reconstructions a data calibration step was performed after noise filtering using a homogenous gel phantom (~0.1 S/m) [23]. A Tikhonov value of 1×10^5 was heuristically determined through visual evaluation of patient data reconstructions. The injected current in EIT and EIS measurements was approximately 0.23 mA, 0.26 mA, 0.30 mA, 0.33 mA for the 10 kHz, 20 kHz, 40 kHz, and 80 kHz measurements, respectively. To give a practical measure of the EIT system signal quality (incorporating noise from cables, electrode array, holding the probe, etc.) Signal-to-Noise Ratio (SNR) values for the EIS patterns considered in this study were computed using repeated EIT measurements recorded from a phantom (0.1 S/m saline with 10% gelatin and 20% graphite as in [24]) with a complex conductivity of ~0.25+0.07i S/m (15º phase); yielding SNR values of 30 dB, 35 dB, and 27 dB for the real, imaginary, and phase components, respectively.

III. Results

All results were evaluated using the soft-regularization (SR-ST) and standard approaches. Unless explicitly stated otherwise all results shown use the SR-ST technique.

A. Simulated and Phantom Experiments

SR-ST reconstructions from the different layers of simulated and phantom experiments (Figs. 5A & 6A, respectively) show the expected conductivity relationships (i.e. $\sigma_{muscle} > \sigma_{skin}$ & $\sigma_{adipose}$) and a generally downward trend in muscle conductivity as a function of skin/adipose-tissue thickness. The depth to muscle was defined as the average distance between the skin surface and start of muscle tissue. In simulation, muscle depth varied along the long-axis of the US probe, whereas in phantom experiments all gels were flat (Figs. 1E & 2). Magnified views (Figs. 5B & 6B) reveal that the different muscle conductivities (simulated and measured) are clearly distinguishable at shallow depths and appear to intersect at deeper depths. The variability in the muscle conductivities from simulation are attributed to the differently shaped skin/adipose-tissue/muscle interfaces. The depths of distinguishability (Figs. 5B & 6B) for the simulated data were 3.2 and 4.6 mm for the 10% and 20% muscle conductivity change, respectively, and for the measured phantom experiment was 3.4 mm, where the two muscles varied by ~12% in conductivity. Differencing the muscles reconstructions (Figs. 5C & 6C) reveals that although the differences reduce as depth increases, the order is almost always correct (50 out of 50 for simulation, and 45 out of 54 for phantoms), i.e. the higher conductivity muscle is consistently reconstructed as being more conductive.

Standard-approach reconstructions (without soft regularization) were markedly different. The muscle reconstructions from the simulated patient data decreased in value till approximately 6 mm then increased, and the reconstructed muscle in phantom data increased. In both simulated and phantom reconstructions the depth of distinguishability was negative (implying that the different muscle properties could not be reliably distinguished at any depth). Additionally, 30 out of 50 and 45 out of 54 cases for the simulated and phantom experiments had muscle changes in the correct direction, respectively.

Three examples of measured phantom SR-ST reconstructions (Figs. 7A-C) from three muscle depths highlight the clear separation between skin/adipose-tissue and muscle layers and show minimal change in estimated muscle conductivity down to ~10 mm (2.8% change in σ_{muscle} between 2.01 mm and 4.82 mm skin/adipose-tissue layer thicknesses). There is a slight decrease in conductivity values as muscle depth increases, and one can observe an increase in artifacts as the depth increases (bottom portions of Figs. 7B-C). In

comparison, the standard reconstructions on the same phantom examples (Figs 8A-C) show profiles that resemble the true layered structure, but there is significant blurring across layers. Further, the estimated muscle conductivity changes much more than the SR-ST reconstructions (+14.6% between 2.01 mm and 4.82 mm skin/adipose-tissue layer thicknesses). Based on the quantitative and qualitative analysis, the SR-ST approach appears to produce far superior reconstructions compared to the standard approach.

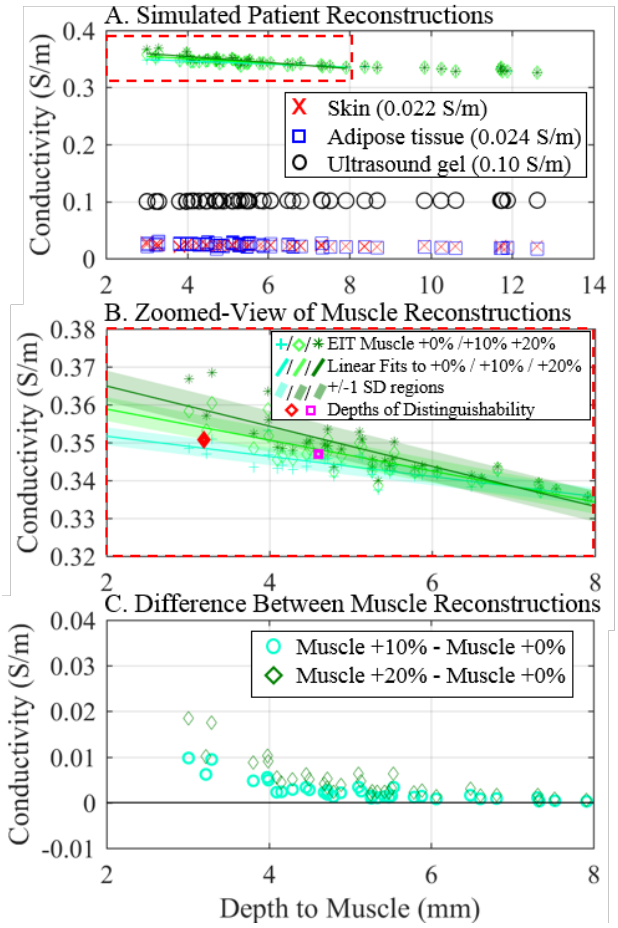

Fig. 5. A. Reconstructions of the US gel, skin, adipose-tissue, and muscle layers for 50 simulated cases, B. a zoomed in view of the muscle results, and C. conductivity differences of muscle reconstructions. The muscle conductivity was increased from a standard literature value (0.35 S/m) by 0%, 10%, and 20%. The colored regions in B represent +/-1 SD bounds, which are used to calculate the depth of distinguishability between 0% and 10% and 0% and 20% muscle changes, respectively.

B. Patient Data: US/EIT-based muscle imaging

A total of 8 sites were measured across the three patients, resulting in 46 EIT reconstructions (3 EIT per site) at each frequency. Two datasets could not be reconstructed because the US images were missing, and one additional reconstruction at 10 kHz was not included because no inverse step was taken (β from the parabolic line-search was found to be zero). Table I shows the patient information (age, sex, depth to muscle, location of measurement site/s). Each site had measurements taken in the longitudinal and transverse direction. The minimum and maximum depths to muscle in Table I plus US image cross sections from Figs. 9, 12, and 14 reveal the variability within patients and across patients of the depth to muscle. Since each patient was only affected on one side, the healthy side was used for the side-by-side healthy versus diseased comparison. In all cases, the US image was not corrupted by the presence of the electrode array and was sufficient for segmenting the adipose-tissue/muscle interface (Fig. 9).

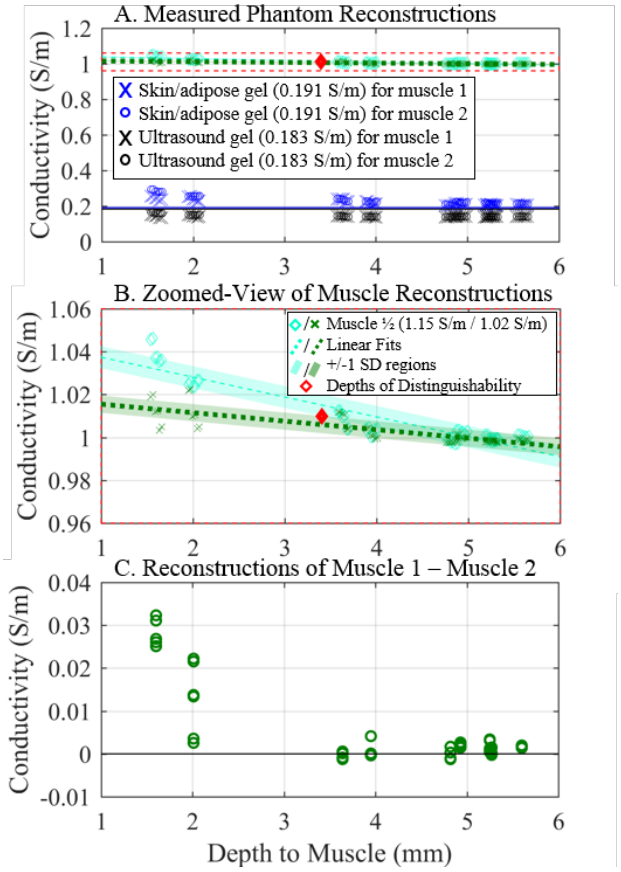

Fig. 6. A. Reconstructions of the US gel, skin/adipose gel, and muscle gel layers for 54 measured datasets (18 gel combinations and 3 repetitions per combination), and B. a zoomed in view of the muscle results, and C. conductivity difference of the two muscle reconstructions. The colored regions in B represent +/-1 SD bounds, which are used to calculate the depth of distinguishability between the two muscles.

The conductivity, permittivity, and phase SR-ST EIT reconstructions of the US gel, skin/adipose tissue, and muscle tissue of all 8 patient cases across all frequencies (Fig. 10) are compared against the (true) literature values. The EIT and literature values are in good agreement for conductivity (all regions), permittivity and phase for muscle. Specifically, the muscle conductivity (mean+/-SD = 0.36+/-0.018 S/m) is significantly different from the skin/adipose-tissue conductivity (mean+/-SD = 0.071+/-0.027 S/m), $p << 0.01$. The coupled skin/adipose-tissue EIT values differ from literature values due to the largely different permittivity ($Im(\sigma_{skin})$ = 0.016-0.078 S/m, $Im(\sigma_{adipose})$ = 0.005-0.006 S/m) and phase ($Ph(\sigma_{skin})$ = 56.4-79.8°, $Ph(\sigma_{adipose})$ = 1.1-1.5°) for skin and adipose. Thus the EIT algorithm is forced to effectively split the difference. Further the US gel is expected

to have nearly zero permittivity/phase, but the EIT values are much higher, similar to skin, which implies that skin is likely pushed into the US gel gap. All of these observations are consistent with our expectations of the tissue properties when considering our current segmentation limitations (see Section IV for more details).

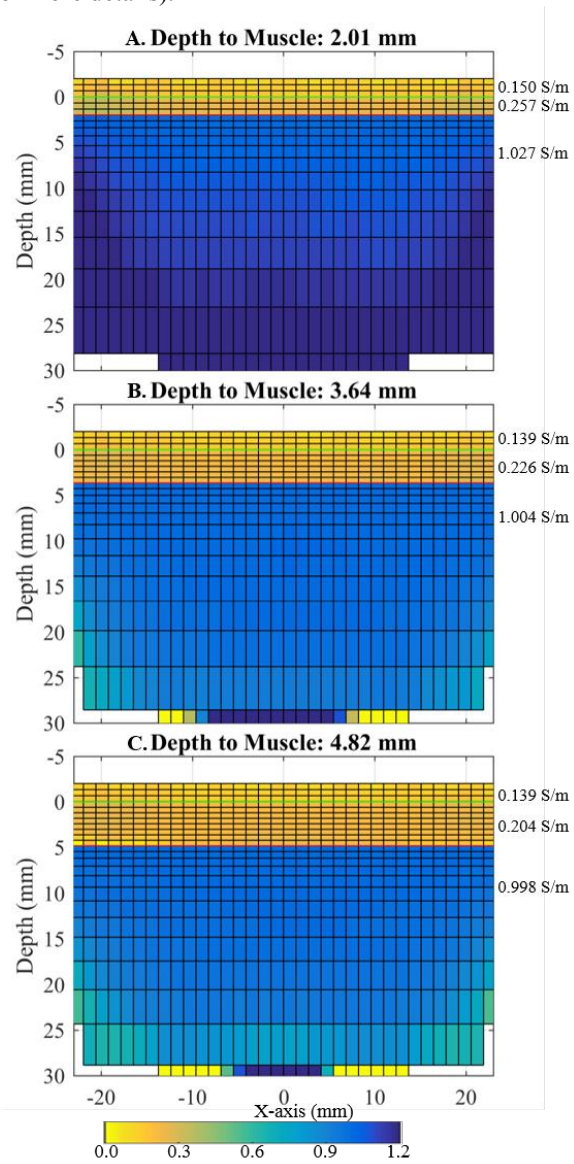

Fig. 7. Example phantom gel reconstructions of where the adipose-gel layer (depth to muscle) was A. 2.01 mm, B. 3.65 mm, and 4.82 mm where the true US gel, skin/adipose-gel, and muscle conductivities were 0.183 S/m, 0.191 S/m, and 1.15 S/m, respectively.

TABLE I. PATIENT INFORMATION

Patients	Age	Sex	Ave. Depth to Muscle (min/max) mm	Probed Site/s
1	67	M	3.18 (2.06/3.83)	Tibialis Anterior
2	65	M	5.02 (3.93/5.82)	Tibialis Anterior
3	47	M	A. 4.19 (3.45/4.88) B. 4.46 (3.91/5.65)	A. Lateral Gastrocnemius B. Medial Gastrocnemius

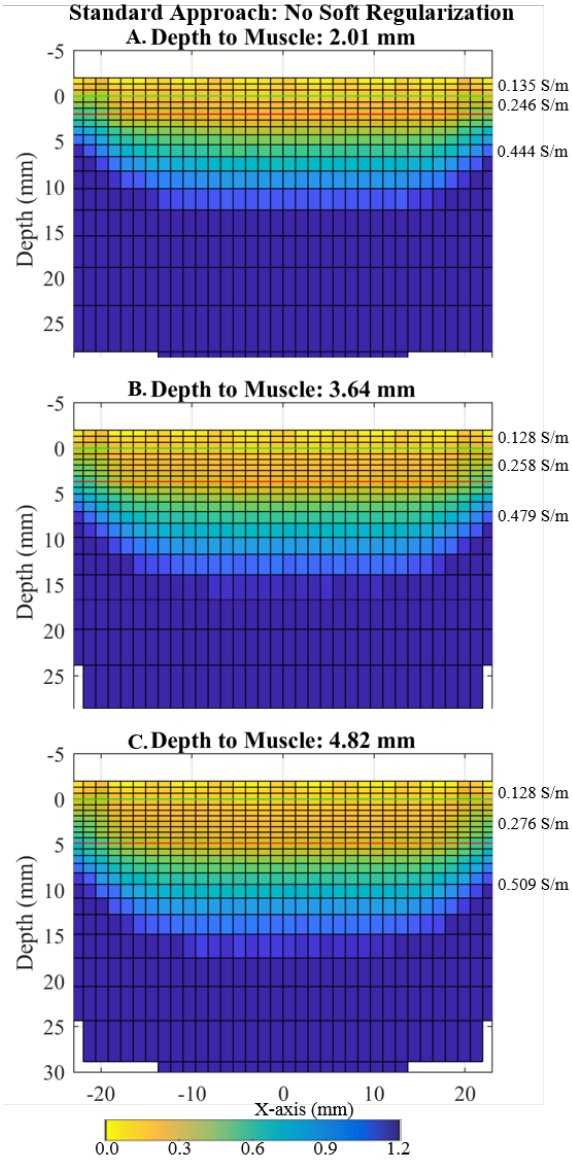

Fig. 8. Example phantom gel reconstructions using the standard approach (no soft regularization). The adipose-gel layer (depth to muscle) was A. 2.01 mm, B. 3.65 mm, and 4.82 mm where the true US gel, skin/adipose-gel, and muscle conductivities were 0.183 S/m, 0.191 S/m, and 1.15 S/m, respectively.

C. Patient Data: Longitudinal versus Transverse

Comparisons between the longitudinal and transverse muscle conductivities on the healthy (unaffected) side (Fig. 11) reveal that: 1) EIS measurements show consistent differences between longitudinal and transverse measurements (in the correct direction; i.e. $R_{long} < R_{trans}$) for 10 and 20 kHz with small change at 40 and 80 kHz in the wrong direction, and 2) EIT shows mostly consistent muscle differences (in the correct direction; i.e. $\sigma_{long} > \sigma_{trans}$) at 40 and 80 kHz. Although, the differences are small, the EIT values result in σ_{long} greater than σ_{trans} in all 40 and 80 kHz cases. Note that the higher conductivity longitudinal values (σ) should correspond to lower resistance values (R) observed in EIS. The muscle fibers should appear more anisotropic at lower

frequencies (see Fig. 2 in [25]), which is consistent with the trends shown in the EIS data (Fig. 11A). It is unexpected that the EIT reconstructions show less directional differentiation at lower frequencies. However, we hypothesize this is due to anisotropy not being modeled in the inverse problem. Although in this small set of samples there is no threshold that can be used to discriminate longitudinal and transverse electrical impedances or conductivities (see Fig. 11), it is observed that the EIT differences at 40 and 80 kHz vary less than the EIS differences at 10 and 20 kHz; specifically, the coefficient of variation were 0.34 and 0.95 for the EIT and EIS differences, respectively. Standard approach reconstructions (no soft regularization) could not definitively discriminate longitudinal from transverse cases, i.e. only 1, 2, and 1 cases were in the correct direction at 20, 40, and 80 kHz, respectively – *no inverse steps were taken for reconstructions at 10 kHz so no comparison was possible there*. Overall, this analysis reveals that EIT coupled with US can image the muscle under the skin/adipose-tissue layer with less variability than EIS (when using this US-coupled electrode array).

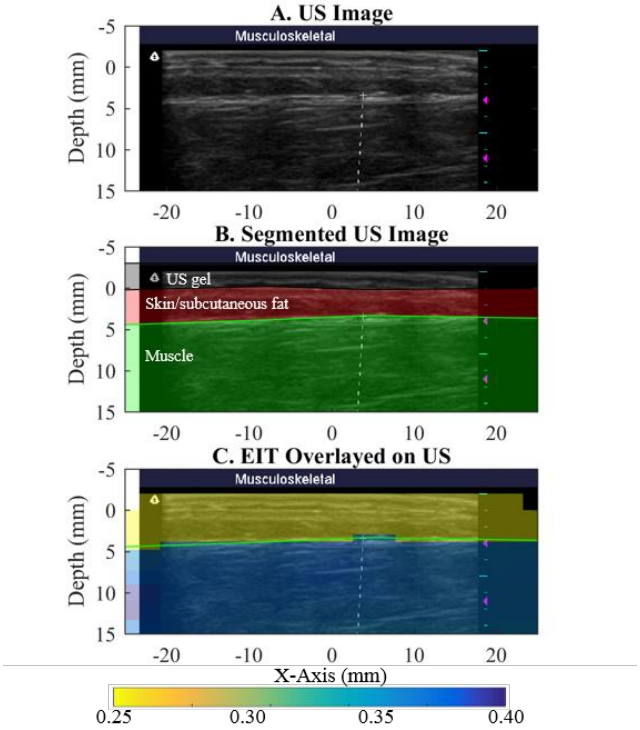

Fig. 9. A) Ultrasound image acquired with US/EIT probe, B) Segmented US image, C) overlaid conductivity image.

Example longitudinal and transverse EIT (real) conductivity reconstructions (Fig. 12) overlaid on the US image, which correspond to P1 at 80 kHz, show the expected results of 1) low conductivity US gel and skin/adipose-tissue layers with higher conductivity muscle layers and 2) a higher conductivity in the muscle layer in the longitudinal compared to the transverse images.

D. Patient Data: Healthy versus Diseased side

Healthy-side versus diseased-side EIS and EIT muscle values are presented in Fig. 13 separated by longitudinal and transverse measurements, and their differences (healthy minus diseased sides) are presented in Fig. 14. Only 10 and 20 kHz are shown for EIS and 40 and 80 kHz for EIT because these were found to yield consistent differences in the correct direction in the longitudinal versus transverse analysis. There are several trends in the EIT data. In the longitudinal measurements, conductivity is generally lower in healthy muscle as compared to diseased tissue, while the permittivity and phase of healthy sides are higher than in diseased sides. The opposite trend is observed in the transverse EIT cases. In the longitudinal measurements, the average phase reduction between healthy and diseased muscle was 26% and 38% for 40 and 80 kHz, respectively; in the transverse case, there was an increase of 29% and 37% for 40 and 80 kHz, respectively. In terms of standard approach reconstructions, no clear trends were found between healthy and diseased sides. Examples of healthy and diseased EIT phase reconstructions of longitudinal cases, corresponding to P3B, overlaid on the US image are shown in Fig. 15. The blocky discontinuities near the electrodes appear to be common near-electrode artifacts, and as these do not appear in Fig. 12 may indicate that the phase data has a higher sensitivity to model-mismatch than conductivity, especially near the electrode array.

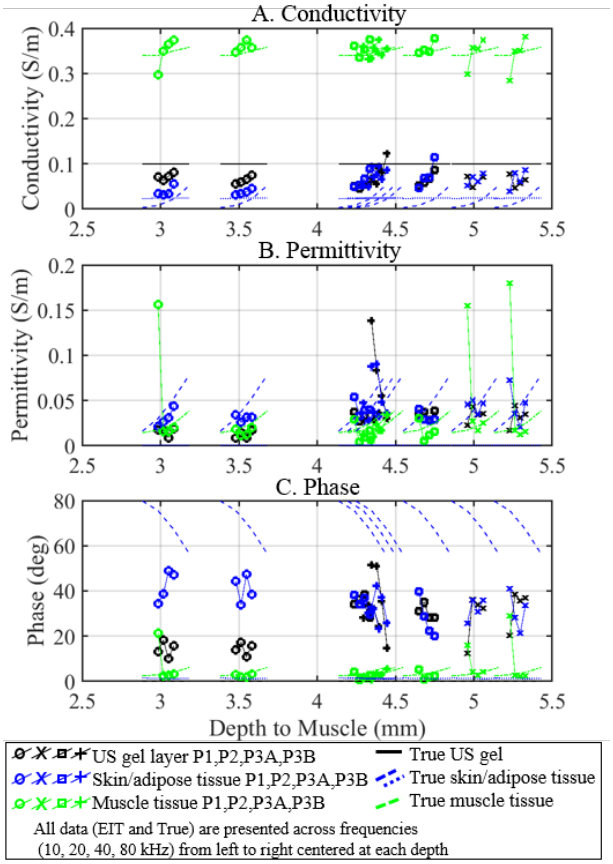

Fig. 10. All patient A. Conductivity, B. Permittivity, and C. Phase EIT reconstructions of the US gel, skin/adipose tissue, and muscle tissue considered in this study with (True) literature curves included for comparison at the 4 frequencies (10, 20, 40, and 80 kHz) plotted versus muscle depth.

Trends are less clear in the EIS data. It appears that the healthy sides tend to have larger resistance and smaller phase than diseased sides. Based on literature, one would expect the resistance and phase of the healthy side to be larger than the

diseased side ([26]). Our hypothesis for the less clear trends and inconsistency with literature of the EIS results are discussed.

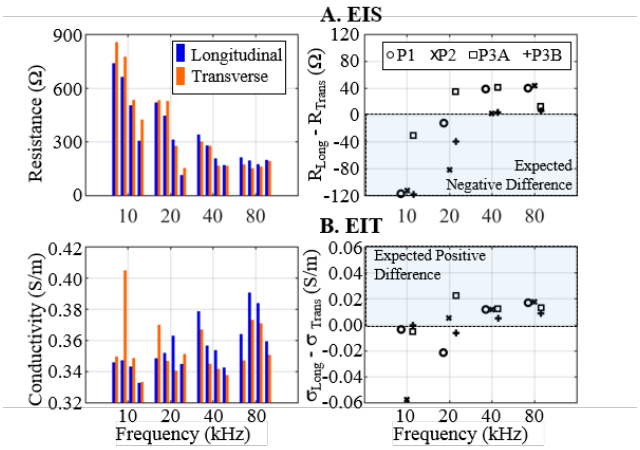

Fig. 11. Comparisons between longitudinal and transverse muscle impedances (A) and reconstructed conductivities (B) across all healthy patient sides. The left-side plots show measurement/reconstruction values ordered left to right from P1 to P3B, whereas the right-side plots show differences.

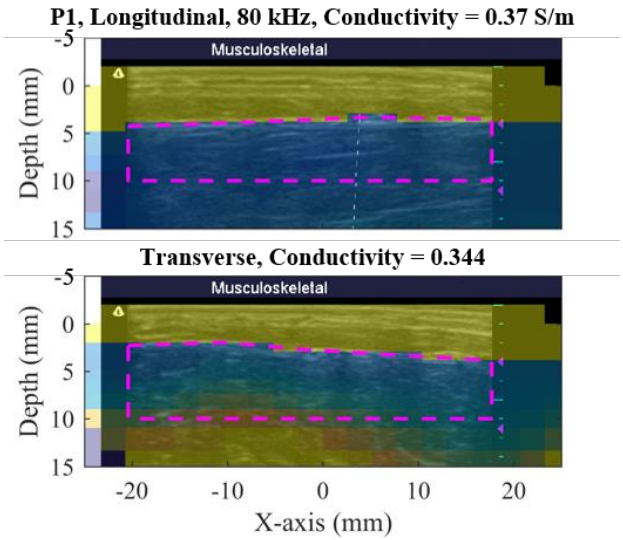

Fig. 12. Example EIT reconstructions of the longitudinal and transverse directions from 80 kHz images of P1 overlaid on their respective US images. The average value of the muscle conductivities (averaged within the purple boxes) are noted in the image titles, which show as expected the longitudinal direction is higher than the transverse.

IV. Discussion

This study suggests that US/EIT has the potential to consistently detect differences between longitudinal and transverse muscle and healthy and diseased muscle tissue in an in vivo setting and that incorporation of US data into the EIT reconstruction is necessary to achieve this. These findings represent an important step in establishing EIT as an extension of EIM. In addition to these results there are two important points of discussion: 1) Comparisons between past EIM and our current EIS results to the US/EIT results. 2) Methods to improve the performance of the US/EIT system.

Comparison between EIM, EIS and US/EIT. It is important to note that the EIS results reported here are based on electrodes more closely spaced than normally considered in EIM (distances are noted in Section I). Since current does not flow as deeply into the muscle for closely spaced electrodes, EIS's sensitivity to differences in skin/adipose-tissue thickness is amplified in this system, resulting in a less accurate assessment of muscle. Use of US/EIT, however, can account for the skin/adipose-tissue layer thickness and suggests trends similar to those found with standard EIM [2]. Specifically, the 26%-38% decrease in diseased muscle phase observed for US/EIT trends in the same direction as the 15% phase decrease observed for EIM when comparing healthy patients to those with radiculopathy [27]. Although this study could not find fixed thresholds to discriminate longitudinal from transverse cases and to discriminate healthy from diseased cases, smaller variations were found in EIT compared to EIS. This is viewed as an important step toward showing that EIT has the potential to provide more reliable tissue classification than EIM.

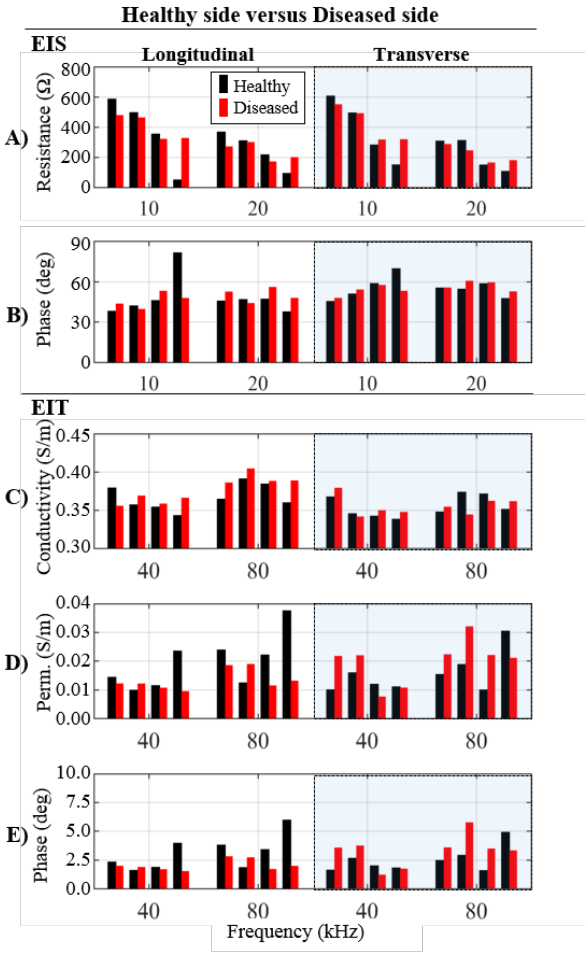

Fig. 13. Comparison between the healthy versus diseased sides in terms of EIS A. resistance and B. phase measurements and the average muscle C. conductivity, D. permittivity, and E. phase from the EIT reconstructions. The two best EIS and EIT frequencies were selected based on the longitudinal versus transverse analysis. The bar plots are ordered left to right from P1 to P3B.

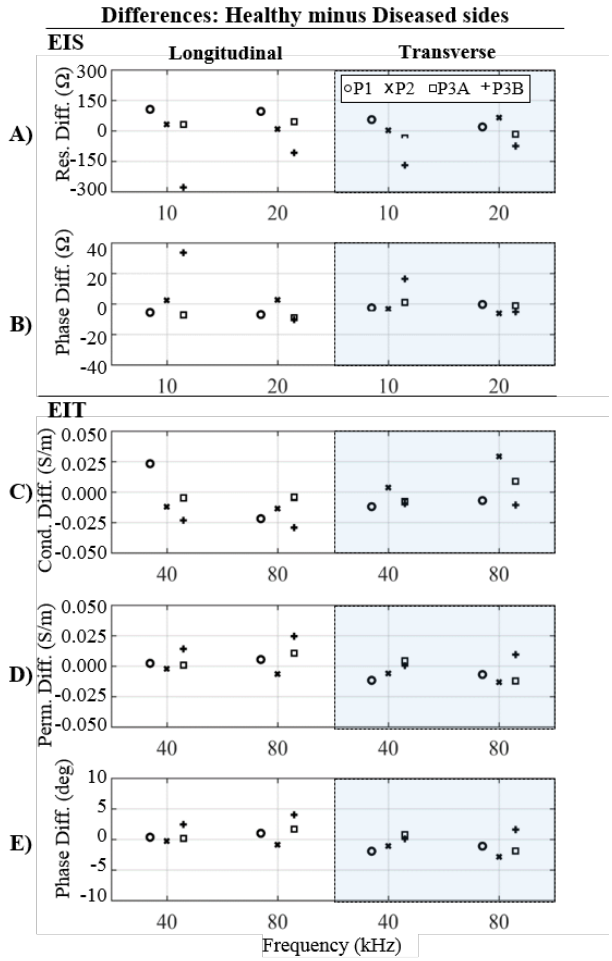

Fig. 14. Differences between the healthy and diseased sides in terms of EIS A. resistance and B. phase measurements and the average muscle C. conductivity, D. permittivity, and E. phase from the EIT reconstructions. The two best EIS and EIT frequencies were selected based on the longitudinal versus transverse analysis.

Methods to improve the performance of the US/EIT system. Two aspects of the system that could enhance imaging accuracy would be to increase the depth of sensitivity and to improve segmentation quality. **Sensitivity**. A wider electrode spacing could be adopted to sense deeper muscle. This could be implemented by using a larger on-probe electrode array (i.e. having the electrode array extend beyond the probe face or ensuring that all channels on the current system are functional). **Segmentation.** The surface reflection artifacts of the US images left the top skin surface and the skin/adipose-tissue interface challenging to segment, which appear to cause the discrepancies observed between reconstructions and literature (Fig. 10). The top skin surface could be accurately constrained by introducing a semi-solid gel layer in the US housing so that the 2 mm gap is maintained and US segmentation of this layer is not needed. Alternatively, a larger gap could be considered, in which the optimal gap thickness is one that produces US images with negligible reflection artifacts at the skin interface while providing maximum sensitivity to the muscle's electrical properties.

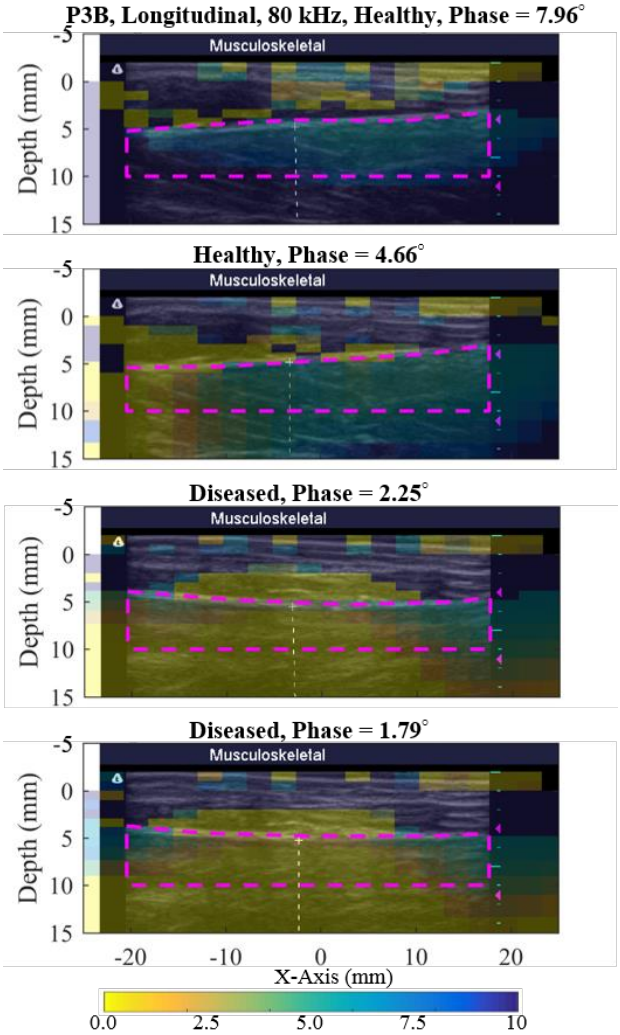

Fig. 15. Example EIT phase reconstructions of healthy and diseased sides corresponding to P3B, overlaid on the associated US image. The muscle average phase values (averaged within the purple boxes) are noted in the image titles.

Algorithmic Improvements. In addition to system changes, algorithm modifications may improve sensitivity and mitigate segmentation errors. Incorporation of anisotropy and adding full 3D reconstructions into the inverse problem could improve EIT results. The lack of anisotropic modeling could explain the poor performance at the low frequencies (10 and 20 kHz) for the longitudinal and transverse comparison (Fig. 11). We could extract estimates of the anisotropic direction based on the probed region's anatomy and recorded US images. This directional information coupled with literature-based estimates of in-fiber and across-fiber properties can be incorporated into the EIT reconstruction framework using methods developed for anisotropic brain imaging ([28], [29]). Because healthy muscle is highly anisotropic, this approach could significantly improve model accuracy and overall sensitivity to changes in muscle. Further, investigating the depth variation in the short axis could be important for determining the need for 3D reconstructions; transitioning to a full 3D reconstruction framework would likely require 3D US information be acquired and more widely spaced electrodes in

the short-axis direction. In terms of segmentation, alternative strategies such as a fuzzy soft-regularization techniques could help to reduce uncertainty in the segmentation of the skin/adipose-tissue interface [30], and improve model accuracy and overall quality of EIT images. Other regularization approaches could also be considered, such as using $(\mathbf{L}^T\mathbf{L})^p$ in (6) with an optimally chosen p value [19].

V. Conclusions

This study establishes for the first time that a coupled Ultrasound/Electrical Impedance Tomography system can be used to spatially map the electrical properties of subsurface skin and adipose tissue and the underlying musculature. In addition, this system provides consistent differences between 1) longitudinal and transverse muscle conductivity reconstructions, and 2) healthy and diseased muscle tissue (in terms of conductivity, permittivity, and phase). After minor system and algorithm upgrades, a larger in vivo patient study is needed to more definitively determine 1) optimal algorithmic approaches, 2) improvements offered by EIT over EIM, and 3) the clinical potential of this technology.

Acknowledgements

This work was supported in part by the U.S. National Institutes of Health under Grants K24 NS060951 and 1R01CA143020–01A1 and DoD CDMRP Grant W81XWH-15-1-0102. We would also like to thank Xiaotian Wu for his design and 3D printing of the US housing and mock US probe.

References

[1] R. Aaron, M. Huang, and C. A. Shiffman, “Anisotropy of human muscle via non-invasive impedance measurements,” *Phys. Med. Biol.*, vol. 42, no. 7, pp. 1245–1262, 1997.

[2] S. B. Rutkove, P. M. Fogerson, L. P. Garmirian, and A. W. Tarulli, “Reference values for 50-kHz electrical impedance myography,” *Muscle and Nerve*, vol. 38, no. 3, pp. 1128–1132, 2008.

[3] S. B. Rutkove, “Electrical impedance myography: Background, current state, and future directions,” *Muscle and Nerve*, vol. 40, no. 6, pp. 936–946, 2009.

[4] P. Narayanaswami, A. J. Spieker, P. Mongiovi, J. C. Keel, S. C. Muzin, and S. B. Rutkove, “Utilizing a handheld electrode array for localized muscle impedance measurements,” *Muscle and Nerve*, vol. 46, no. 2, pp. 257–263, 2012.

[5] S. Khan, P. Manwaring, A. Borsic, and R. Halter, “FPGA-Based Voltage and Current Dual Drive System for High Frame Rate Electrical Impedance Tomography,” *IEEE Trans. Med. Imaging*, vol. 34, no. 4, pp. 888–901, 2015.

[6] E. K. Murphy, X. Wu, and R. J. Halter, “Fused-data transrectal EIT for prostate cancer imaging,” *Physiol. Meas.*, 2018.

[7] M. Jafarpoor, J. Li, J. K. White, and S. B. Rutkove, “Optimizing electrode configuration for electrical impedance measurements of muscle via the finite element method,” *IEEE Trans. Biomed. Eng.*, vol. 60, no. 5, pp. 1446–1452, 2013.

[8] E. Somersalo, M. Cheney, and D. Isaacson, “Existence and Uniqueness for Electrode Models for Electric Current Computed Tomography,” *SIAM J. Appl. Math.*, vol. 52, no. 4, pp. 1023–1040, 1992.

[9] A. Borsic, A. Hartov, K. D. Paulsen, and P. Manwaring, “3D electric impedance tomography reconstruction on multi-core computing platforms,” *Conf. Proc. Int. Conf. IEEE Eng. Med. Biol. Soc.*, vol. 2008, no. 1557–170X (Print), pp. 1175–1177, 2008.

[10] T. Lee, M. Leok, and N. H. McClamroch, “Geometric numerical integration for complex dynamics of tethered spacecraft,” *Proc. 2011 Am. Control Conf.*, no. May, pp. 1885–1891, 2011.

[11] W. R. B. Lionheart, “EIT reconstruction algorithms: pitfalls, challenges and recent developments,” *Physiol. Meas.*, vol. 25, no. 1, pp. 125–142, 2004.

[12] A. Borsic, R. Halter, Y. Wan, A. Hartov, and K. D. Paulsen, “Electrical impedance tomography reconstruction for three-dimensional imaging of the prostate,” *Physiol. Meas.*, vol. 31, no. 8, pp. S1–S16, 2010.

[13] E. Murphy, A. Mahara, and R. Halter, “A Novel Regularization Technique for Microendoscopic Electrical Impedance Tomography,” *IEEE Trans. Med. Imaging*, vol. 35, no. 7, pp. 1593–1603, 2016.

[14] G. Steiner, M. Soleimani, and D. Watzenig, “A bio-electromechanical imaging technique with combined electrical impedance and ultrasound tomography.,” *Physiol. Meas.*, vol. 29, no. 6, pp. S63–S75, 2008.

[15] P. M. Meaney, A. H. Golnabi, N. R. Epstein, S. D. Geimer, M. W. Fanning, J. B. Weaver, and K. D. Paulsen, “Integration of microwave tomography with magnetic resonance for improved breast imaging,” *Med. Phys.*, vol. 40, no. 10, p. 103101, 2013.

[16] E. K. Murphy, A. Mahara, X. Wu, and R. J. Halter, “Phantom Experiments using Soft-Prior Regularization EIT for Breast Cancer Imaging,” *Physiol. Meas.*, vol. 38, pp. 1262–1277, 2017.

[17] B. A. Brooksby, H. Dehghani, B. W. Poque, and K. D. Paulsen, “Near-infrared (NIR) tomography breast image reconstruction with a priori structural information from MRI: Algorithm development for reconstructing heterogeneities,” *IEEE J. Sel. Top. Quantum Electron.*, vol. 9, no. 2, pp. 199–209, 2003.

[18] D. Andreuccetti, R. Fossi, and C. Petrucc, “Dielectric Properties of Body Tissues: HTML clients.” [Online]. Available: http://niremf.ifac.cnr.it/tissprop/htmlclie/htmlclie.php. [Accessed: 09-Nov-2017].

[19] A. Adler, T. Dai, and W. R. B. Lionheart, “Temporal image reconstruction in electrical impedance tomography,” *Physiol. Meas.*, vol. 28, no. 7, 2007.

[20] M. Cheney, D. Isaacson, J. C. Newell, S. Simske, and J. Goble, “NOSER: An algorithm for solving the inverse conductivity problem,” *Int. J. Imaging Syst. Technol.*, vol. 2, no. 2, pp. 66–75, 1990.

[21] M. H. Loke and R. D. Barker, “Practical techniques for 3D resistivity surveys and data inversion,” *Geophys. Prospect.*, vol. 44, pp. 499–523, 1996.

[22] M. H. Loke, “Tutorial : 2-D and 3-D electrical imaging surveys,” *Geotomo Softw. Malaysia*, no. July, p. 127, 2013.

[23] N. K. Soni, H. Dehghani, A. Hartov, and K. D. Paulsen, “A novel data calibration scheme for electrical impedance tomography.,” *Physiol. Meas.*, vol. 24, no. 2, pp. 421–435, 2003.

[24] T. J. Kao, G. J. Saulnier, D. Isaacson, T. L. Szabo, and J. C. Newell, “A versatile high-permittivity phantom for EIT,” *IEEE Trans. Biomed. Eng.*, vol. 55, no. 11, pp. 2601–2607, 2008.

[25] B. R. Epstein and K. R. Foster, “Anisotropy in the dielectrc properties of skeletal muscle,” *Med. Biol. Eng. Comput.*, vol. 21, no. January, pp. 51–55, 1983.

[26] A. J. Spieker, P. Narayanaswami, L. Fleming, J. C. Keel, S. C. Muzin, and S. B. Rutkove, “Electrical impedance myography in the diagnosis of radiculopathy,” *Muscle and Nerve*, vol. 48, no. 5, pp. 800–805, 2013.

[27] S. B. Rutkove, G. J. Esper, K. S. Lee, R. Aaron, and C. A. Shiffman, “Electrical impedance myography in the detection of radiculopathy,” *Muscle and Nerve*, vol. 32, no. 3, pp. 335–341, 2005.

[28] J.-F. P. J. Abascal, S. R. Arridge, W. R. B. Lionheart, R. H. Bayford, and D. S. Holder, “Validation of a finite-element solution for electrical impedance tomography in an anisotropic medium.,” *Physiol. Meas.*, vol. 28, no. 7, pp. S129-40, 2007.

[29] J. F. Abascal, S. R. Arridge, D. Atkinson, R. Horesh, L. Fabrizi, M. De Lucia, L. Horesh, R. H. Bayford, and D. S. Holder, “Use of anisotropic modelling in electrical impedance tomography: description of method and preliminary assessment of utility in imaging brain function in the adult human head,” *Neuroimage*, vol. 43, no. 2, pp. 258–268, 2008.

[30] B. Deng, D. H. Brooks, D. A. Boas, M. Lundqvist, and Q. Fang, “Characterization of structural-prior guided optical tomography using realistic breast models derived from dual-energy x-ray mammography,” *Biomed. Opt. Express*, vol. 6, no. 7, p. 2366, 2015.

PAPER

Fused-data transrectal EIT for prostate cancer imaging

IOP Publishing Physiol. Meas. 39 (2018) 054005 (13pp) https://doi.org/10.1088/1361-6579/aabf22

Physiological Measurement

IPEM Institute of Physics and Engineering in Medicine

PAPER

Fused-data transrectal EIT for prostate cancer imaging

Ethan K Murphy[1], Xiaotian Wu[1] and Ryan J Halter[1,2]

[1] Thayer School of Engineering, Dartmouth College, Hanover, NH 03755, United States of America
[2] Geisel School of Medicine, Dartmouth College, Hanover, NH 03755, United States of America

E-mail: Ethan.K.Murphy@dartmouth.edu

RECEIVED
15 December 2017

REVISED
6 April 2018

ACCEPTED FOR PUBLICATION
18 April 2018

PUBLISHED
24 May 2018

Keywords: electrical impedance tomography, measurement sensitivity, data fusion, prostate cancer

Abstract

Objective: Prostate cancer is a significant problem affecting 1 in 7 men. Unfortunately, the diagnostic gold-standard of ultrasound-guided biopsy misses 10%–30% of all cancers. The objective of this study was to develop an electrical impedance tomography (EIT) approach that has the potential to image the entire prostate using multiple impedance measurements recorded between electrodes integrated onto an end-fired transrectal ultrasound (TRUS) device and a biopsy probe (BP). *Approach*: Simulations and sensitivity analyses were used to investigate the best combination of electrodes, and measured tank experiments were used to evaluate a fused-data transrectal EIT (fd-TREIT) and BP approach. *Main results*: Simulations and sensitivity analysis revealed that (1) TREIT measurements are not sufficiently sensitive to image the whole prostate, (2) the combination of TREIT + BP measurements increases the sensitive region of TREIT-only measurements by 12×, and (3) the fusion of multiple TREIT + BP measurements collected during a routine or customized 12-core biopsy procedure can cover up to 76.1% or 94.1% of a nominal 50 cm^3 prostate, respectively. Three measured tank experiments of the fd-TREIT + BP approach successfully and accurately recovered the positions of 2–3 metal or plastic inclusions. *Significance*: The measured tank experiments represent important steps in the development of an algorithm that can combine EIT from multiple locations and from multiple probes—data that could be collected during a routine TRUS-guided 12-core biopsy. Overall, this result is a step towards a clinically deployable impedance imaging approach to scanning the entire prostate, which could significantly help to improve prostate cancer diagnosis.

1. Introduction

Prostate cancer is a significant problem for men. One of every seven men will be diagnosed with the disease, and in 2016 over 180 000 newly diagnosed cases were reported in the US (Siegel *et al* 2016). Detecting prostate cancer non-invasively is clinically challenging. Prostate-specific antigen (PSA)-based screening has a high sensitivity, but low specificity due to numerous benign processes elevating PSA levels in the blood (Walsh 2007). Men with elevated levels of PSA routinely undergo an image-guided biopsy procedure for more accurate diagnosis (Shariat and Roehrborn 2008). During these procedures, transrectal ultrasound (TRUS) is used to visualize the prostate and a series of 6–20 biopsy cores are typically extracted from standard locations within the prostate (TRUS alone is not sufficiently sensitive and specific for targeted biopsy (Harvey *et al* 2012)). Unfortunately, TRUS-guided biopsies miss 10%–30% of all cancers (Walsh 2007); these low detection rates stem largely from the small volume of tissue sampled during these biopsy procedures (typically <1% of the prostate volume) (Harnden *et al* 2008).

Our overall goal is to improve the accuracy of prostate cancer diagnosis using transrectal electrical impedance tomography (TREIT) so that cancers of clinical significance can be identified earlier through targeted biopsy. Numerous *ex vivo* studies have found that electrical impedance can be used to differentiate cancerous from benign prostate tissue (Lee *et al* 1999, Halter *et al* 2007, Salomon *et al* 2009). Furthermore, TREIT has been described as a potential adjunct to TRUS (Wan *et al* 2010, Syed *et al* 2012), and one study considered the fusion of TREIT and a biopsy probe (BP) electrode (though the development was very preliminary) (Wan *et al* 2012). The early work in TREIT-based imaging systems relied on the use of a *side-fired* TRUS probe which provided 3D ultrasound images of the prostate. While having the 3D prostate image was useful for mesh generation in EIT, this

geometry was not compatible with routine clinical biopsy procedures in which an *end-fired* TRUS probe is the standard-of-care; the side-fired TRUS probe required men to be in a more exposed and uncomfortable lithotomy position as opposed to a lateral position used for an end-fired probe. In addition to being more commonly used, end-fired probes also yield significantly higher rates of cancer detection (Ching *et al* 2009). Here we explore how TREIT might be coupled to an *end-fired TRUS probe* and optimized for imaging during prostate biopsy procedures.

The challenge in transitioning to an end-fired probe is that the surface area available for electrodes is significantly less than that available on a side-fired device. As a result, fewer or smaller electrodes must be used and the maximum electrode spacing will be reduced; this reduced spacing directly impacts the depth of sensitivity (e.g. section 2.5.2 of (Loke 2013)). Comparing the region of sensitivity between the two geometries reveals that the side-fired probe is sensitive to 21× more volume of a nominal prostate (50 cm^3) than an end-fired probe (12.6% compared to 0.6%). Here we show that coupling electrodes on the TRUS probe with distant electrodes embedded on a BP placed within the prostate increases the region of sensitivity to 94.6% and 7.2% for the side- and end-fired probes, respectively. While sensitivity for the coupled approach using the end-fired geometry is still too small, we hypothesize that fusing EIT data recorded from multiple states (i.e. BP positions) will provide sufficient sensitivity for imaging the entire prostate with a standard-of-care end-fired TRUS probe. For the remainder of this manuscript, TRUS and TREIT will refer to the end-fired geometry unless explicitly defined to be referencing a side-fired probe.

This study presents a simulated experiment, sensitivity analysis, and three measured tank experiments to (1) illustrate why it is necessary and advantageous to combine BP with TREIT data and (2) demonstrate *for the first time* that recording TREIT + BP impedance data from multiple locations in a saline filled tank can be successfully fused to produce accurate reconstructions of conductivity. Through the simulated experiment, we show that the end-fired TREIT probe by itself can accurately detect a 2 mm metal inclusion (without noise) out to a maximum distance of only 12–13 mm from the probe face. While combining TRUS + BP measurements together increased the sensitive region of TRUS-only measurements by 12×, this volume is still insufficient to image the entire prostate. To overcome this, we have developed a fused-data (fd) approach to couple multiple TREIT + BP measurements together.

Three saline tank experiments were conducted to validate specific aspects of the fd-TREIT + BP approach. Specifically, 2–3 metal and plastic inclusions were submerged in the tank and multiple impedance measurements were recorded from the TREIT + BP device when it was (1) rotated at a fixed radius around a set of inclusions, (2) randomly translated around the inclusions in a single x/y-plane, and (3) randomly translated in four x/y-planes about the inclusions. Electromagnetic (EM) tracking was used to record the TRUS-probe state (position and orientation) for the latter two experiments. These three experiments were each important validation steps towards a generalized fusion of 3D state data for EIT and were used to establish that (1) fd-EIT is feasible (rotation experiment), (2) fd-EIT using EM tracking is feasible (single z-plane experiment), and (3) fd-EIT using EM tracking can produce accurate 3D reconstructions (four z-plane experiment). Reconstructions were successful in all three experiments, yielding average position errors of 1.27, 2.49, and 2.56 mm, respectively. The fd-TREIT + BP algorithm was investigated through exploration of (1) the size of the reconstructed region of interest (ROI) over which the conductivity distribution was allowed to vary, (2) the voxel sizes of the reconstruction mesh, and (3) the data used in the reconstruction algorithm.

Here we demonstrate the potential improvements that can be realized in EIT when multiple probes are combined to image a volume of interest. In particular, this work demonstrates the feasibility of fusing data extracted from an end-fired TRUS-based prostate biopsy procedure. Tank experiments specifically suggest that by combining end-fired TREIT electrodes with four electrodes embedded on a BP and sampling from multiple positions (as would be done in a multi-core prostate biopsy procedure), one can produce spatially accurate images able to identify inclusions ~2× beyond the sensitivity region of the TREIT probe alone. A final contribution is the description of the open-domain fusion algorithm which can be considered for other applications with similar constraints.

The paper is structured as follows. Section 2 describes the forward and inverse EIT problems, instrument tracking, the experiments conducted, and the measurement system, parameters and metrics used for analysis. Section 3 describes the results of the simulated experiment, sensitivity and measurement analysis, and three measured tank experiments. Section 4 discusses the likely approaches to overcome the sensitivity of the current algorithm to parameter values, and describes steps towards clinical evaluation of the method.

2. Methods

2.1. Forward problem

The forward problem relies on solving the Laplace equation, $\nabla \cdot \sigma \nabla u = 0$, over an open domain, where σ is the conductivity and u is the electric potential. The complete electrode model (CEM) is used to realistically

account for discrete electrodes (Somersalo *et al* 1992). The forward problem calculates the electric potential distribution throughout the domain and voltages on the electrodes assuming the conductivity distribution and applied currents on the electrodes are known. The CEM boundary conditions specify no current flows in or out of the domain except through the electrodes. The open domain is modeled by expanding the modeled domain sufficiently so that effectively no current is flowing near the boundaries representing open portions of the domain. The solution to the forward problem is calculated in 3D using the finite element method (FEM) with linear basis functions.

2.2. Inverse methods

The inverse method considered here is the standard Gauss–Newton algorithm employing a Laplace-smoothing Tikhonov regularization scheme. At a given state, standard EIT data, which we refer to as a frame of data, is collected on the TREIT array and BP electrodes (TREIT + BP). Here we considered fused-data EIT which combines frames from multiple states of the TREIT + BP data. Similar to the approach in Murphy *et al* (2017a), the aim is to minimize the following objective function:

$$E(\boldsymbol{\delta\sigma}) = \sum_{n=1}^{N_S} \|\boldsymbol{J_n}\boldsymbol{\delta\sigma} - \boldsymbol{\Delta v_n}\|_2^2 + \lambda \|\boldsymbol{L}(\boldsymbol{\sigma}_0 + \boldsymbol{\delta\sigma})\|_2^2, \tag{1}$$

where N_S is the number of states of data fused together, $\mathbf{J}_n$ is the Jacobian corresponding to the nth state, $\boldsymbol{\Delta v_n}$ is the voltage differences of the nth state, λ is the Tikhonov factor, $\mathbf{L}$ is the regularization matrix, σ_0 is the initial guess of the conductivity distribution, and $\boldsymbol{\delta\sigma}$ is the perturbation we aim to solve for at each iteration. Note each $\mathbf{J_n}$ and $\boldsymbol{\Delta v_n}$ are size $N_P \times N_C$ and $N_P \times 1$, respectively, where N_P is the number of measurement patterns and N_C are the number of coarse inverse voxels. One can rewrite (1) equivalently as

$$E(\boldsymbol{\delta\sigma}) = \|\boldsymbol{J_{FD}}\boldsymbol{\delta\sigma} - \boldsymbol{\Delta v_{FD}}\|_2^2 + \lambda \|\boldsymbol{L}(\boldsymbol{\sigma}_0 + \boldsymbol{\delta\sigma})\|_2^2, \tag{2}$$

where $\boldsymbol{J_{FD}}$ and $\boldsymbol{\Delta v_{FD}}$ are concatenated matrices and vectors from all the states. This formulation allows one to use the standard updating formula:

$$\boldsymbol{\delta\widetilde{\sigma}} = \left(\boldsymbol{J_{FD}^T J_{FD}} + \lambda \boldsymbol{L}^T\boldsymbol{L}\right)^{-1}\left(\boldsymbol{J_{FD}^T \Delta v_{FD}} - \boldsymbol{\lambda L}^T\boldsymbol{L\sigma}_0\right). \tag{3}$$

Only difference images are considered in this study. Thus $\boldsymbol{\Delta v}_{FD}$ is the difference between a test measurement and a reference measurement of homogeneous conductivity.

Our inverse implementation uses the dual-mesh method (Borsic *et al* 2010), which allows one to solve the Jacobian on a fine mesh while estimating the conductivity on a much coarser inverse mesh. This approach yields an electric potential with high accuracy throughout the domain and enables a convenient approach to fuse data from different states. For difference imaging, assuming a homogeneous conductivity, the coarse Jacobian for any state is calculated by the following: (1) a fine Jacobian, $\mathbf{J}_{F,0}$, is computed on the fine mesh in a untransformed state (e.g. State 1, figure 1); (2) a single coarse mesh is chosen (red, uniform grid in figure 1); (3) the fine mesh (FEM mesh) is transformed to a specific measured state (e.g. State 2 or 3, figure 1) and a coarse-to-fine matrix is constructed, $\mathbf{P}_n$; and (4) the coarse Jacobian of the nth state is then computed by $\boldsymbol{J}_n = \mathbf{J}_{F,0}\mathbf{P}_n$. Note that $\mathbf{P}_n$ is size $N_F \times N_C$, where N_F and N_C are the number of fine (FEM) and coarse voxels, respectively, and that the ith column of $\mathbf{P}_n$ is zeros except for 1's at rows corresponding to associated fine nodes of the ith coarse voxel. For example, the cyan fine nodes highlighted in figure 1, which are different for each of the three states, are associated to the fixed coarse voxel (blue box). The computational cost is primarily due to the untransformed fine Jacobian, which is solved using the formulation derived in Geselowitz (1971). Thus, for difference imaging where $\mathbf{J}_{F,0}$ could be computed previously, the computational time is very minimal for all coarse Jacobians.

The open domain is modeled in the inverse problem via a mega-node, which has been used in Syed *et al* (2012) and Murphy *et al* (2016). In practical terms, the coarse mesh that we define encompasses a region in the domain, a reconstructed ROI, where we expect sufficient sensitivity to resolve spatially varying conductivity. Outside of this region a single conductivity value is reconstructed, and this is referred to as a mega-node.

2.3. Instrument tracking

In order to specify the TRUS probe location and orientation within our imaging domain (i.e. the different states in figure 1), EM tracking was used to localize the TRUS/TREIT probe. An Aurora V2 EM tracking system (Northern Digital Inc., Ontario, Canada) was used to track a 1 × 5 mm six degree-of-freedom sensor attached directly to the TRUS probe via heat shrink (see figure 2(D)) and a second similar sensor embedded in a 85 mm long pointing stylus. The EM-tracked stylus pointed to five known locations on the TRUS probe to register the probe in EM-space. The BP was affixed to the TRUS probe and the stylus pointed to the electrodes on the BP for registration. The stylus was also used to determine the location of the inclusions by pointing to the surface of the inclusions and then subtracting the respective radii. All tracking data in the form of Cartesian 3D coordinates

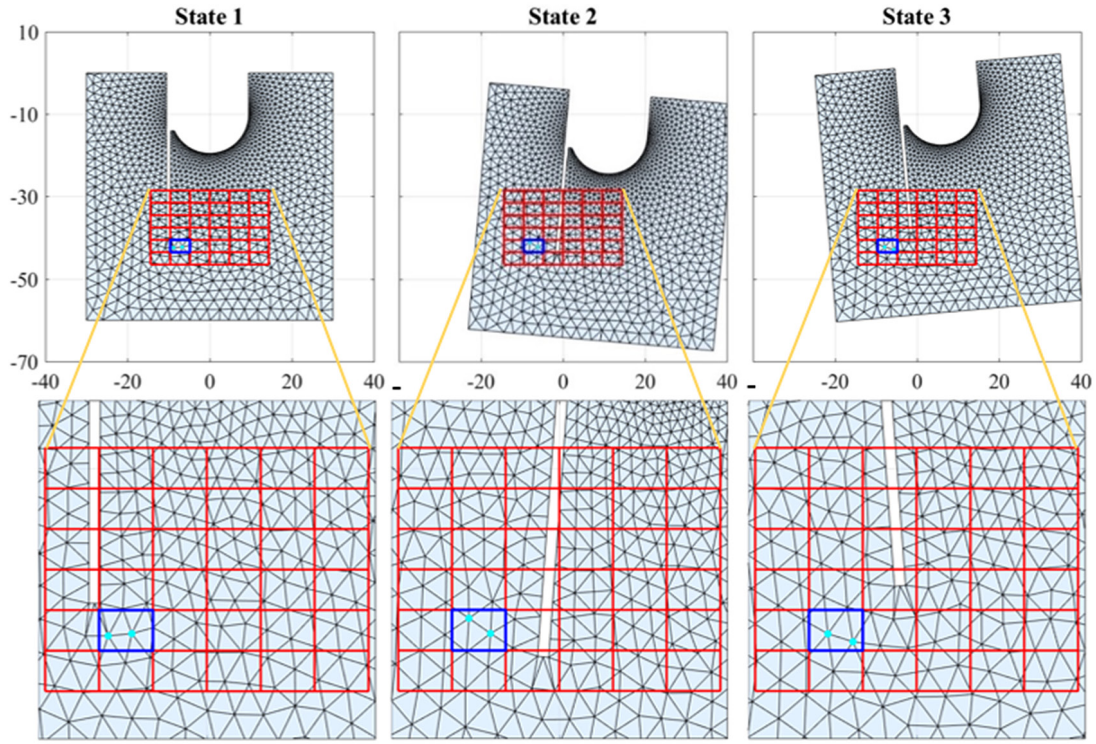

Figure 1. 2D illustration of coarse-to-fine fusing process, which involves a fixed coarse mesh (red uniform grid) and a fine FEM mesh that is translated and rotated to the state of each measurement. A coarse voxel is highlighted in blue and associated fine FEM nodes are highlighted as cyan nodes for each state. The TRUS probe and biopsy needle are cut-out of the domain because they represent boundaries in terms of electrode modeling.

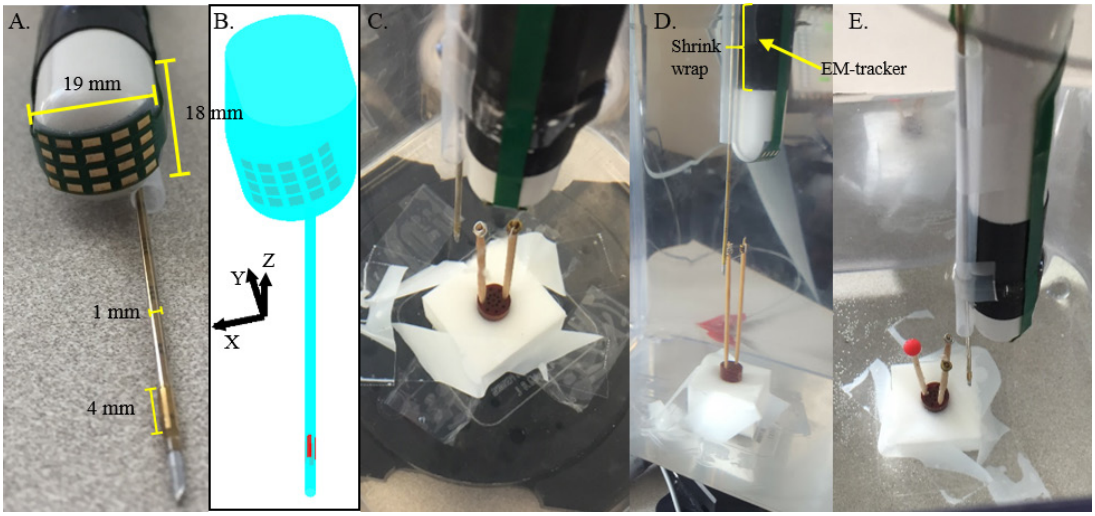

Figure 2. The TRUS and BPs (A) compared to its modeled counterpart (B), and photographs from the rotation experiment with two metal inclusions (C), the 1 *z*-plane, *x*/*y*-translation experiment also with two metal inclusions (D), and the four *z*-plane, *x*/*y*-translation experiment and three inclusions (one plastic and two metal) (E).

(translation) and quaternions (orientation) was acquired via serial communication with the Aurora system in MATLAB. A planar phantom consisting of a checkerboard pattern with 25.4 mm squares was used to evaluate the EM tracking system accuracy. The stylus was tracked while pivoting (20 times) at each corner from a chosen set of grid corners. This yielded average distances of 25.725 mm between adjacent sides with a standard deviation of 0.55 mm (n = 209). At least two EM measurements were used to determine each inclusion position, which implies position accuracy within $0.39 = 0.55/\sqrt{2}$ mm (assuming error within ± 1 SD and the error is unbiased and normally distributed). The errors in BP and TRUS registration should be smaller due to averaging over four and five points, respectively.

Table 1. Details of Experiments.

Experiment	BP used	No. of states/frames	Inclusions	Diameters
Simulated inclusions	No	1	1 metal	2 mm
Measured rotations	Yes	18	2 metal	3 mm
Measured 1 Z-plane, x/y-translations	Yes	25	2 metal	3 mm
Measured 4 Z-plane, x/y-translations	Yes	60 (15-per slice)	2 metal, 1 plastic	3 and 5 mm

2.4. Experiment and modeling details

All experiments were based on the dimensions of a Phillips C9-EC TRUS probe and all tank experiments incorporated a BP (figure 2(A)). Twenty gold-plated electrodes (size 1.5 mm $\times$ 2.0 mm) configured in a 4 $\times$ 5 grid were printed on a 1 mil polyamide substrate and secured with a pressure sensitive adhesive over the active element of the TRUS probe; the electrode array is sonolucent to provide multi-modal imaging with both TRUS and TREIT (Wan *et al* 2012). Four gold-plated electrodes (size 4 mm $\times$ 0.6 mm) were similarly printed on 1 mil thick polyamide substrate and secured around the BP (Everitt *et al* 2018). A 3D FEM mesh that matched the probe and electrode dimensions, which had roughly 500k nodes and 3M elements, (figure 2(B)) was produced using gmsh (Geuzaine and Remacle 2009). To model the open domain, the mesh was extended 80 mm in the x- and y-directions from the probe face and 20 mm behind and 70 mm in front of the tip of the TRUS probe; along the z-direction (see figure 2(B) for axes orientations). The remainder of this section details the experiments conducted and the modeling choices made for the coarse meshes.

2.4.1. Experiment descriptions

The BP is held fixed relative to the TRUS probe for all measured tank experiments with the BP electrodes always 37 mm in front of the probe face. There was one simulation experiment and three measured tank experiments. The tank experiments (figures 2(C)–(E)) include rotations, x/y-translations in a single plane, and x/y-translations at four different depths (or z-planes) of the TRUS probe. Table 1 details the experimental parameters.

2.4.1.1.Simulation experiment

Simulations were performed to provide an estimated depth of sensitivity that the TRUS probe can achieve without the presence of the BP electrodes. Simulated data was produced corresponding to a single metal inclusion with 2 mm diameter placed 3–20 mm from the TRUS probe in 1 mm steps at angles spanning from $-45°$ to 45° degrees with respect to the TRUS probe axis.

2.4.1.2.Measured rotation experiment

The TREIT + BP system was held fixed and the saline tank (positioned on a rotation stage) was rotated in 20° increments. This yielded 18 frames of TREIT + BP data for reconstruction. The inclusions were centered about the rotation axis and were separated by 12 mm. The TRUS probe was also centered on the rotation axis with the BP offset 11 mm from the rotation axis and in the same direction; the BP electrodes were located 37 mm in front of the TRUS probe face. The metal inclusions were tightly wound copper wire of 3 mm diameter, and were placed on ~2 mm diameter wooden posts that were soaked in saline overnight to minimize their effect on measurements.

2.4.1.3.Measured 1 Z-plane, x/y-translation experiment

Twenty-five frames of TREIT + BP data were recorded from random translations of the TRUS probe at a fixed depth within the saline tank. Two 3 mm diameter metal inclusions spaced 10 mm apart were used for this experiment (see figures 2(D) and 6(B)). The states (position and orientation) of the TRUS probe were recorded with the EM tracker.

2.4.1.4.Measured 4 Z-plane, x/y-translation

Sixty frames of EIT data were recorded from random translations of the TRUS probe at four different depths or z-planes (15 frames per z-plane) (see figures 2(E) and 6(C)). There were three inclusions; two 3 mm diameter metal inclusions and a 5 mm diameter plastic bead. The three inclusions were placed in different x/y-locations and at different depths (z). The true locations were determined via the pointing stylus using the EM tracker.

2.4.2. Coarse mesh descriptions

Two types of coarse meshes were considered: (1) a cylindrical-based mesh that fans out from the TRUS probe face in the simulation experiment, and (2) a Cartesian-based mesh within a cylinder representing the ROI about the inclusions in the three measurement experiments.

2.4.2.1.Simulation experiment's coarse mesh

The cylindrical coordinates extended from the probe face (a radius of 8 mm from an origin chosen within the TRUS probe) to 32 mm, angles $\pm 60°$ from the axis of the TRUS probe (z-axis in figure 2(B)), and the cylinder height is in the y-axis (see figure 2(B)). There are a total of 1401 voxels centered at 10, 20, and seven equally spaced points in the radial, angular, and y-axis directions, respectively, and a single mega-node modeled the remaining domain.

2.4.2.2.Measurement experiments' coarse mesh

The coarse meshes for the measured tank experiments were all Cartesian based in a cylindrical ROI centered on the mean of the inclusions. It was important to explore how large of an ROI can be used, since the aim is to image the entire prostate. To investigate this, reconstructions were performed by varying (1) the voxel sizes from $1.5 \times 1.5 \times 2.7$ mm to $3.0 \times 3.0 \times 2.7$ mm in 0.5 mm steps, and (2) the radius of the ROI's from 5 to 20 mm in variable step sizes (~2–3 mm). This resulted in coarse meshes ranging from 209 to 4712 voxels.

2.5. Sensitivity and measurement analysis

The region of sensitivity and the effective number of independent measurements were investigated to characterize the impact of probe geometry and individual measurement patterns. Regions of sensitivity recorded from multiple states were grouped to evaluate how accurately the electrical properties can be estimated throughout an entire prostate. Here, measurement patterns are specified as IIVV groupings for each impedance measurement where II represents the current injection electrode pair (I1,I2) and VV represents the differential voltage sensing pair of electrodes (V1,V2).

2.5.1. Regions of sensitivity

The regions in which measurements were deemed to have sufficient sensitivity for imaging were analyzed for the previously used side-fired TRUS probe (Syed *et al* 2012) and the end-fired TRUS and BP probes for different sets of IIVV patterns. The region of sensitivity was determined by collecting all coarse mesh voxels whose maximum relative sensitivity (given by the Jacobian) were greater than a specified tolerance, e.g. the relative sensitivity of the ith coarse voxel, $(\mathbf{j}_{\boldsymbol{Rel}})_{\boldsymbol{i}}$, is defined as

$$(\mathbf{j}_{\boldsymbol{Rel}})_{\boldsymbol{i}} = \left(\max_{1 \leqslant m \leqslant N_P} |\boldsymbol{j}_{\boldsymbol{m,i}}| \right) / \left(\max_{1 \leqslant i \leqslant N_C} \left[\max_{1 \leqslant m \leqslant N_P} |\boldsymbol{j}_{\boldsymbol{m,i}}| \right] \right), \tag{4}$$

where $\boldsymbol{j}_{\boldsymbol{m,i}}$ is the (m, i)th component of the Jacobian matrix, $\mathbf{J}$. A tolerance of 1/500 was used; this tolerance has previously been demonstrated to provide a good estimate of the region of sensitivity (Murphy *et al* 2016). If fused-data is considered, then the maximum calculation in (4) represents the highest sensitivity over all the patterns and all the considered states for each coarse node. A nominal prostate with volume 50 cm^3 (assumed spherical), and placed 0.5 cm away from the probe to account for the rectal wall, was used to quantify how much of the prostate was encompassed by the region of sensitivity.

2.5.2. Imaging the entire prostate using 12-core biopsy data

The region of sensitivity about the BP electrodes on the end-fired BP analysis was used to determine the percentage of the prostatic volume that could be imaged by fusing together data recorded during a 12-core biopsy procedure of a nominal 50 cm^3 prostate; this analysis assumes that TREIT + BP data can be recorded at one or two depths by simply translating the BP during needle insertion or removal. Three methods were used to determine BP locations: (1) standard probe sites determined from diagrams in Numao *et al* (2008) and Baumann *et al* (2012), (2) two optimal depths per core assuming BP needle trajectories from a standard 12-core biopsy, (3) two optimal depths per core with optimal BP needle trajectories that are within T_D degrees of the standard. The optimization method utilized Matlab's genetic algorithm (*ga*), which is a heuristic optimization method that can quickly find near-optimal solutions.

2.5.3. Number of independent measurements

The effective number of independent measurements was investigated using Picard's condition (Hansen 1998). Assuming the Jacobian is decomposed into its singular value decomposition, $\mathbf{J} = \mathbf{USV}^T$, the Picard condition determines the effective number of singular values by finding where the singular values (diagonal of $\mathbf{S}$) drops to the level of noise (determined via the Fourier coefficients $|\boldsymbol{u}_{\boldsymbol{n}} \cdot \boldsymbol{v}_{\boldsymbol{FD}}|$, where $\boldsymbol{u}_{\boldsymbol{n}}$ is the nth columns of $\mathbf{U}$). Two examples of singular value curves and Fourier coefficients are given in section 3.2 (figure 5(A)) to illustrate the process. The effective the number of singular values is essentially the number of independent measurements.

Table 2. Reconstruction parameters.

Experiment	Patterns per frame/state	Max. patterns used in reconstructions	Tik. factor	Threshold tolerance
Simulated inclusions	29 070	29 070	1×10^1	0.75
Measured rotations	64	1152	1×10^3	0.8
Measured 1 Z-plane, x/y-translations	107	2675	1×10^5	0.7
Measured 4 Z-plane, x/y-translations	19	1140	1×10^3	0.8 metal, −0.8 plastic

2.6. Measurement system, additional parameters, and metrics

Impedance data was recorded using a custom designed EIT system (Khan *et al* 2015). All data was sampled at 10 kHz. Data was recorded on exhaustive, non-flip, non-bipolar IIVV sets of 22 electrodes (18 from TRUS probe and four from the BP), which totaled 43 890 (($C_4(22)$ 4-electrode combinations) × (six IIVV electrode orderings per combination) = 43 890 patterns). Here flip patterns, e.g. for an IIVV = [1 2 3 4], refer to [1 2 4 3], [2 1 3 4], and [2 1 4 3]. In the tank experiments only data that had patterns with 2-TRUS and 2-BP electrodes were used, which numbered 3672. The number of patterns used for image reconstructions were further reduced using a highly restrictive filter that removed any 'bad' patterns, which were determined from homogeneous saline measurements recorded on the day of the experiment. These bad patterns were defined as those that (1) exceeded a noise threshold based on the noise filter described in Murphy *et al* (2017b), (2) reported impedances more than 10% greater than or less than a scalar-best fit to simulated data (patterns where $(\gamma \boldsymbol{v}_{Meas} - \boldsymbol{v}_{Sim})/\boldsymbol{v}_{Sim} > 10\%$, where γ is a scalar that minimizes the impedance differences), (3) had a (log-base 10) coefficient of variation (CoV) that was more than 0.08 away from a log-linear fit, and (4) that had a best fit slope (impedance per sample) that was over 0.03. The CoV constraint was heuristically chosen and was developed to remove measurements that had a CoV that was too high (small voltages likely corrupted by noise) or too low (possibly saturated measurements with unrealistically small standard deviations). The last requirement aimed at removing patterns that experienced a drift, which has intermittently been observed in some measurement patterns in our system. After the overall noise filtering there were 64, 107, and 19 patterns at each BP location for the rotation, 1 z-plane, x/y-translation, and 4 z-plane, x/y-translation experiments, respectively. The average standard deviations from these good patterns for these three experiments were 0.135 mV, 0.134 mV, and 0.096 mV, respectively. In all experiments the saline was 0.1 S m^{-1}, and in all measured reconstructions a saline calibration step was performed after noise filtering (Soni *et al* 2003).

The remaining parameters used in the reconstructions (Tikhonov factor) and data analysis (threshold tolerance) are shown in table 2. Note that the simulated experiment assumed 20 TRUS electrodes, did not use BP electrodes, and the 29 070 patterns represents the full set of exhaustive, non-flip, non-bipolar IIVV patterns for 20 electrodes, i.e. ($C_4(20)$ 4-electrode combinations) × (six IIVV electrode orderings per combination). The threshold tolerance multiplied by the absolute maximum of each reconstruction was used to determine if a coarse voxel was declared a reconstructed conductor or insulator. Both the Tikhonov factor and threshold tolerance were heuristically determined.

The metrics used to evaluate the reconstructions were (1) the center of mass of the reconstructed conductivities exceeding a specified tolerance, and (2) the mean position error of the connected conductive or insulative regions. In the second metric, the position error was averaged over the position error of each reconstructed conductive or insulative region by calculating the minimum distance to the true position of the metal inclusions or plastic bead, respectively.

3. Results

This section presents the results for (1) the single-inclusion simulation experiment, (2) the sensitivity and measurement analysis of the TRUS and BP electrode measurements, and (3) the three saline tank experiments.

3.1. Single-inclusion simulation TREIT experiment (TRUS electrodes only)

The first experiment involved only the TRUS electrodes and simulated imaging of a metal inclusion that was positioned at varied distances and angles from the probe face (figure 3(A)). These simulations revealed that the maximum accurate distance that a single metal inclusion could be recovered, defined as a mean position error of less than 2 mm, is 12–13 mm away from the probe face (figure 3(B)) with no added noise. Given that the rectal wall is approximately 5 mm thick and that a prostate may be 50 mm in maximum dimension, this experiment implies that TREIT only data may be insufficient to image the whole prostate.

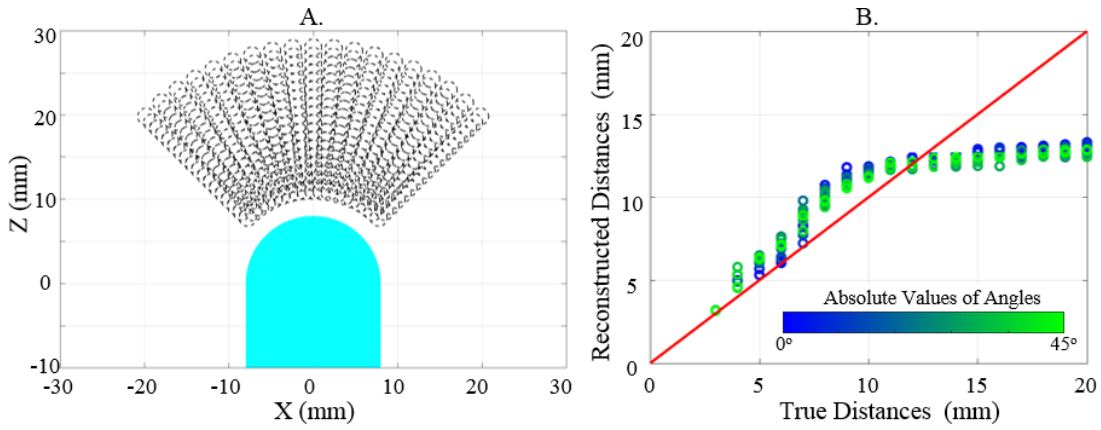

Figure 3. (A) Location of the true simulated inclusions, and (B) a plot comparing the reconstructed and true inclusion distances. This simulated experiment revealed a 12–13 mm maximum depth sensitivity without noise.

3.2. Sensitivity and measurement analysis

3.2.1. Region of sensitivity

Ideally, TREIT will have sufficient sensitivity within all regions encompassing the prostate, which we model as a 50 cm^3 sphere for this analysis. The larger side-fired TREIT probe has significantly more sensitivity than the end-fired geometry (12.6% versus 0.6%, respectively; compare figures 4(A) and (C)). Incorporating BP patterns significantly increases the volume of sensitivity; the side-fired probe increases to 94.6% (compared to 12.6%) and the end-fired probe increases to 7.2% and 1.8% (compared to 0.6%) assuming either two TRUS and two BP electrode patterns or BP-only patterns, respectively. This analysis reveals how much more challenging the EIT problem is for the end-fired geometry as compared to the side-fired probe and that the two TRUS and two BP patterns provide significantly more sensitivity than the TRUS-only or BP-only patterns of the end-fired geometry. Overall, this suggests that data fusion using impedances recorded from multiple BP locations is needed to have sufficient sensitivity throughout the entire prostate. Although the three tank experiments were not explicitly designed to reconstruct over an entire prostate, these experiments provide examples for visualizing the effective region of sensitivity available through fusion of all measurements into a single Jacobian (figures 4(F)–(H)). The overall percent coverage of a nominal 50 cm^3 prostate from these three experiments (table 3) is 33.2%, 55.4%, and 91.4% for the rotation, one Z-plane, and four Z-plane experiments, respectively. Thus we see that with multiple (x, y, z)-translations of the BP one can nearly cover the entire prostate, achieving a similar coverage to the side-fired TRUS probe with BP electrodes at a single position (91.4% compared to 94.6%).

3.2.2. Imaging the entire prostate using 12-core biopsy data

A 3.6 cm^3 spherical region of sensitivity exists about each measurement site (e.g. figure 4(D)). Fusion of EIT measurements from standard 12-core BP sites resulted in 45.0% coverage of the prostate. Two optimal depths assuming standard trajectories from a 12-core biopsy resulted in 76.1% coverage of the prostate. Two optimal depths and optimal trajectories that were within 5 and 10 degrees from a standard 12-core biopsy resulted in 88.0% and 94.1% coverage of the prostate, respectively.

3.2.3. Number of independent measurements

Based on Picard's condition (figure 5(A)) and the four z-plane experimental data, the average number of effective singular values over the 60 data frames was roughly seven and four for all two TRUS & two BP patterns (3672) and for only those patterns actually used (19), respectively (figure 5(B)); this finding was similar for all reconstruction ROIs and pixel sizes considered. The primary reason there are so few independent measurements per data frame is that the ROI is centered on the average inclusion position, which is outside the region of sensitivity near to the face of the end-fired TRUS probe. This analysis illustrates another way in which the small size of the end-fired TRUS probe and its corresponding small region of sensitivity contribute to the challenging nature of the problem. Furthermore, despite using only 19 measurements at each probed location for reconstruction, this analysis shows that this represents a reduction of only three effective independent measurements per data frame as compared to the maximum possible when using all two TRUS and two BP patterns. This suggests that even though the number of patterns remaining after noise filtering is small for the three experiments (64, 107, and 19; table 2, column 2), these patterns are likely sufficient for estimating the conductivity in the ROIs.

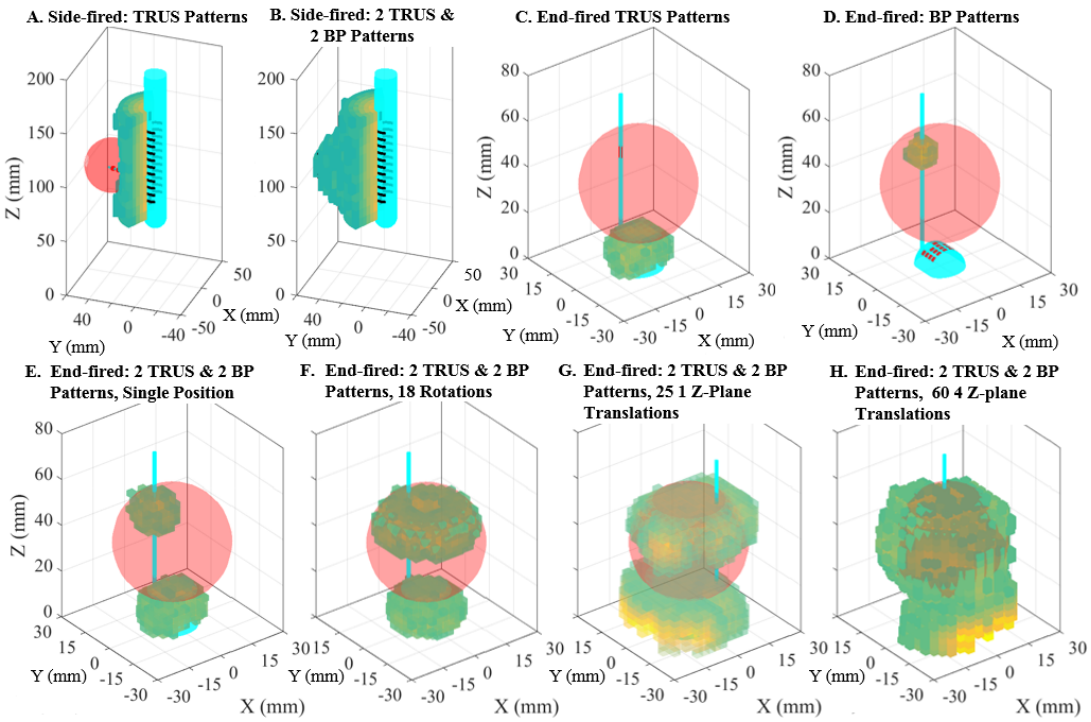

Figure 4. Illustration of the regions of sensitivity for the previously studied side-fired TRUS probe assuming (A) TRUS-only patterns and (B) two TRUS and two BP patterns, and the end-fired probe assuming (C) TRUS patterns only, (D) BP patterns only, (E) patterns with two TRUS and two BP patterns, and overall sensitivity from fusing two TRUS and two BP patterns corresponding to the (F) rotation, (G) one *Z*-plane, and (H) four *Z*-plane experiments.

Table 3. Volume of sensitivity regions and percent volume assuming a 50 cm^3 prostate.

Probe	Measurements	Volume near TRUS (cm^3)	Volume near BP (cm^3)	Total volume (cm^3)	Total percent volume (%)
Side-fired	TRUS patterns	6.3	NA	6.3	12.6
Side-fired	2 TRUS/2 BP	47.3	NA	47.3	94.6
End-fired	TRUS patterns	0.3	0.0	0.3	0.6
End-fired	BP patterns	0.0	0.9	0.9	1.8
End-fired	2 TRUS/2 BP	0.6	3.0	3.6	7.2
End-fired	1 TRUS/3 BP	0.0	1.5	1.5	3.0
End-fired	3 TRUS/1 BP	0.4	0.0	0.4	0.8
End-fired	2 TRUS/2 BP fused: rotation exp.	0.7	15.9	16.6	33.2
End-fired	2 TRUS/2 BP fused: 1 *Z*-plane exp.	3.0	24.7	27.7	55.4
End-fired	2 TRUS/2 BP fused: 4 *Z*-plane exp.	NA	45.7	45.7	91.4

3.3. Saline tank experiments

The average position error for the rotations in a single *z*-plane with 2 metal inclusions (figure 6), *x*/*y*-translations in a single *z*-plane with 2 metal inclusions (figure 7(A)), and *x*/*y*-translations in four *z*-planes with 2 metal and 1 plastic inclusions (figure 7(B)) are shown as a function of the ROI radius for the four resolutions considered. The best reconstructions in terms of average position error are listed in table 4 and shown in figure 9 in three views for each of the three experiments. Figure 9 also shows the positions of the BP electrode measurements (black dots), reconstructed conductors (yellow blocks) and insulators (blue blocks), true conductors (red spheres) and insulators (pink spheres), and ROIs (green cylinders).

For the rotation experiment, the two inclusions can only be resolved when the reconstruction ROI radius ranges from 5.2 to 6.4 mm. For larger ROI radii, the two inclusions merge into a single, centrally located elevated region of conductivity. Based on the sensitivity study in section 3.2, this could be due to the small sensitivity in the center of the ROI (i.e. the central portion of the annular sensitivity volume of figure 4(F)).

In addition to reconstructing images with impedance data collected from all BP locations in the translation experiments, we also (figures 9(B) and (C)) reconstructed images using subsets of data recorded when the BP was positioned within a limited radius; this enabled us to evaluate how the position of the BP influences the accuracy of the reconstructed inclusions (multiple curves in figures 7(A) and (B)). Figure 8 illustrates the number of BP

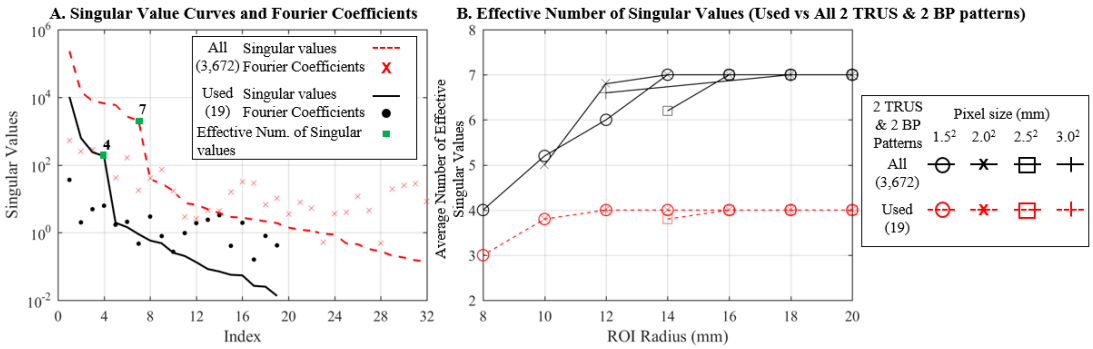

Figure 5. (A) Two examples of using Picard's condition to determine the number of effective singular values (i.e. there are four and seven singular values above the noise level of the Fourier coefficients), and (B) the average number of effective singular values for the used and all two TRUS and two BP patterns across all the pixel sizes and ROIs considered. (A) Only shows the first 32 singular values of the 3672 singular values assuming all two TRUS & two BP patterns, because all pertinent information for Picard's condition analysis is contained in this zoomed-in window.

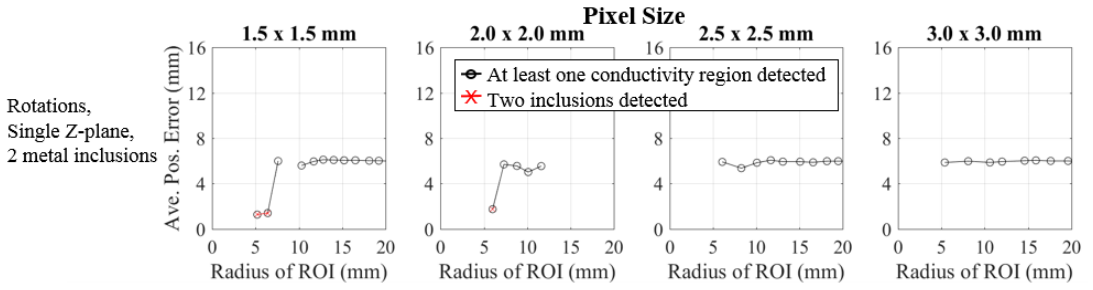

Figure 6. Average position error for the measured rotation experiment with two metal inclusions. The four plots show results for coarse voxels with size 1.5 × 1.5 mm to 3.0 × 3.0 mm in 0.5 mm steps.

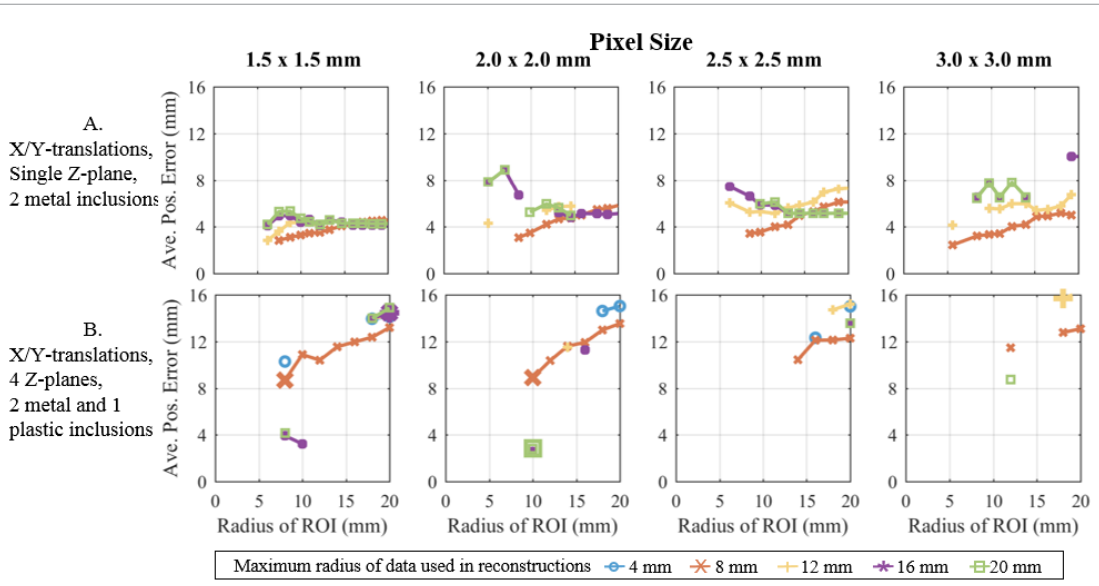

Figure 7. Average position error for the saline tank experiments assuming (A). 1 *z*-plane, *x*/*y*-translations with two planar, metal inclusions, and (B) four *z*-plane, *x*/*y*-translations with two metal and one plastic inclusions. The columns show results for coarse voxels with size 1.5 × 1.5 mm to 3.0 × 3.0 mm in 0.5 mm steps. Each curve corresponds to reconstructions that used EIT data in which BPs (*x*/*y*) radial position was less than a specified maximum tolerance (defined in legend). Results are only shown in (A) if two conductors were detected, and in (B) if at least one insulator and one conductor were detected. Further, in (B) markers are enlarged if the correct number of targets were found (two conductors and one insulator).

probe locations that are within selected maximum radii. The single *z*-plane *x*/*y*-translation experiment showed the best robustness to varying ROI radii and voxel size; all parameter settings yielded similar average position errors. However, similar to the rotation experiments, the position errors were slightly better both qualitatively and quantitatively when the ROI extended just beyond the inclusions.

Table 4. Best quantitative results.

Experiment	Voxel size (mm)	Max. radius of data	ROI radius (mm)	Ave. pos. error (mm)
Rotations	1.5 × 1.5	11 mm (fixed)	5.2	1.27
1 *Z*-plane, *x*/*y*-translations	3.0 × 3.0	8 mm	5.6	2.49
4 *Z*-planes, *x*/*y*-translations	2.0 × 2.0	16 mm	10	2.56

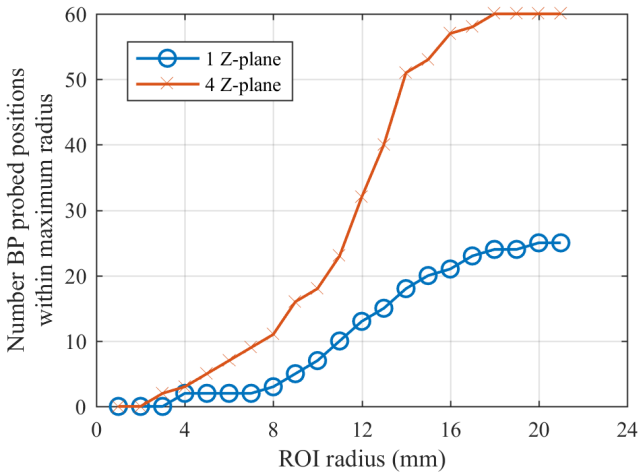

Figure 8. Number of data points within the ROI of each given radius. These curves illustrate how many frames of data were used in figures 7(A) and (B).

The four *z*-plane, *x*/*y*-translation experiment was similar to the rotation experiment in that there was a small ROI radius range (8–10 mm) that resulted in small average position errors. The metal inclusions were positioned at 7.3 and 6.6 mm and the plastic inclusion at 9.6 mm from the center of the imaging domain. In all three experiments it appears that an ROI radius extending to just beyond the inclusions produces the best results.

4. Discussion

Fusing data recorded from TRUS- and BP-based electrodes positioned at multiple sites within a domain (i.e. fd-TREIT + BP) provides enhanced EIT sensitivity as compared to TRUS-based imaging alone and aligns with the routine clinical scenario of sampling multiple cores during end-fired TRUS-guided prostate biopsy procedures. Sensitivity analysis revealed that 76.1% or 94.1% of a nominal 50 cm^3 prostate could be covered with fd-TREIT + BP using data recorded during a routine or custom 12-core biopsy, respectively. Given that the typical human prostate ranges from 15 to 30 cm^3 (Walsh 2007), this fused-data EIT approach has the potential to image nearly the full prostatic volume even in cases in which the prostate is larger in size (e.g. >50 cm^3) due to benign prostatic hyperplasia or adenocarcinoma (Uzzo *et al* 1995). Two significant steps that are being pursued in current research are (1) how to design the approach to be more robust to parameter selection (i.e. ROI and voxel size), and (2) how to image the entire prostate or an ROI within the prostate (e.g. through the use of a BP with additional electrodes along its length). We note that during the TRUS-guided biopsy procedure images such as figures 4(F) and (G) could be constructed in real time to help guide probing locations and ensure full- or nearly full coverage of the prostate.

A significant limitation of this approach is that the accuracy of the reconstruction is largely dependent on the ROI over which electrical properties are estimated. The results presented here suggest that the reconstruction ROI should encompass a volume that extends to just beyond the inclusions; however, the inclusion, or tumor, location will not typically be known in the clinical setting. One approach to improve the current method is to employ a sensitivity-based coarse mesh similar to those developed in a 2D closed domain EIT scenario (Saulnier *et al* 2001) and in open-domain applications (Loke 2013, Murphy *et al* 2016). In some clinical cases (e.g. MR-TRUS fusion), the tumor location may be known *a priori* (Siddiqui *et al* 2015); in these situations, the TREIT ROI could be specified based on the tumor locations identified in MR images registered to the ultrasound image space. Additionally, incorporating the prostate boundary and/or tumor locations/boundary using hard prior (Syed *et al* 2012) or soft-prior (Murphy *et al* 2017c) techniques may further improve the robustness of the method.

A second limitation of the study was that the number of BP locations sampled was larger than typically collected during a 12-core biopsy, i.e. 18, 25, and 60 for rotation, one *z*-plane, and four *z*-plane, respectively. While the 60 measurements far exceed the standard 12-core limit, if multiple samples are recorded as the biopsy needle

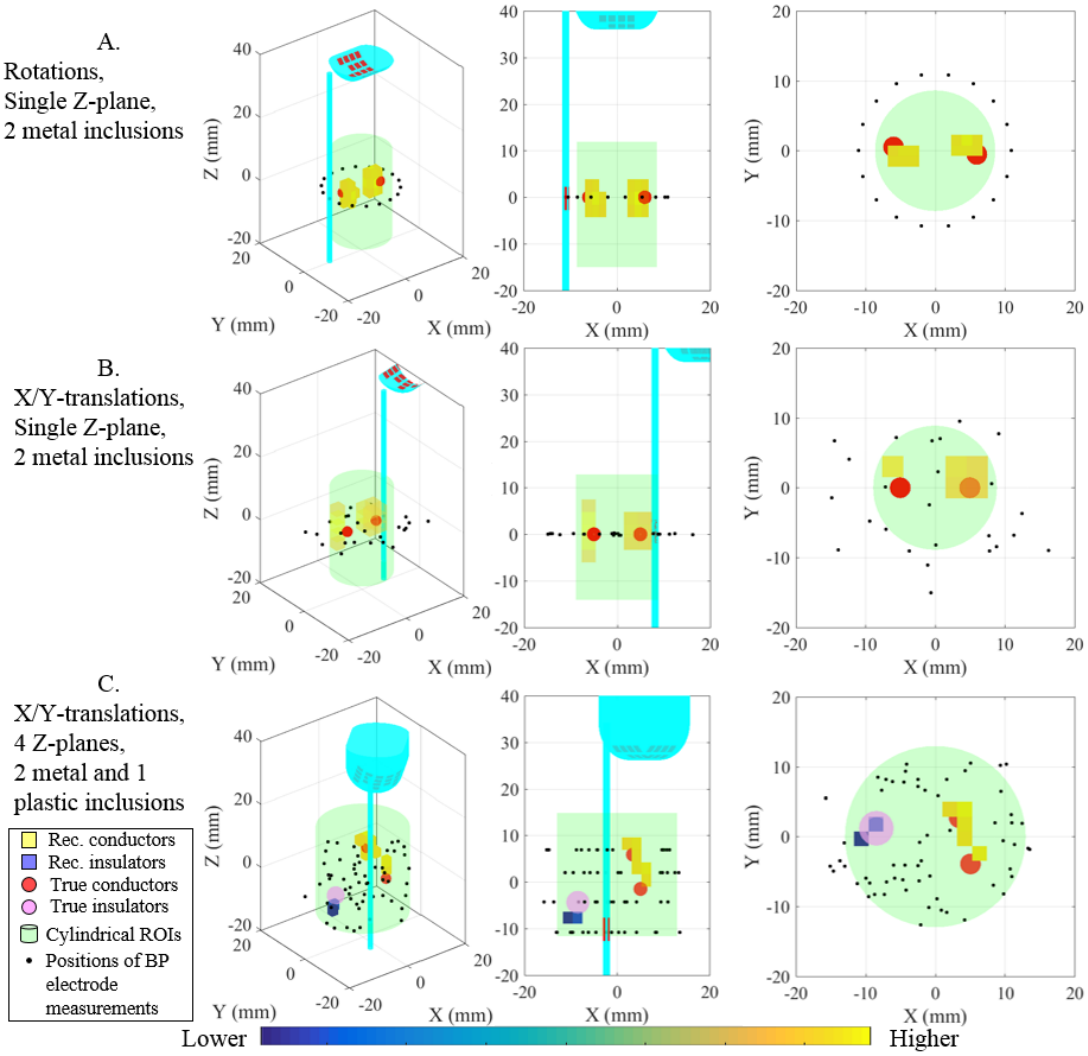

Figure 9. Three views of reconstructions that yielded minimum average position errors in the three saline tank experiments: (A) rotations in a single *z*-plane with two metal inclusions, (B) *x*/*y*-translations in a single *z*-plane with two planar, metal inclusions, and (C) *x*/*y*-translations in four *z*-planes with two metal and one plastic inclusions.

is advanced, or if additional electrodes are embedded along the shaft of the biopsy needle, multiple *z*-plane data can be recorded from a single biopsy location. For example, if four *z*-planes are sampled as the biopsy needle is inserted, only 15 cores would need to be extracted to sample at 60 total locations. We are currently exploring the potential of recording at multiple depths during a single core extraction and of embedding additional electrodes along the length of the biopsy needle.

We have demonstrated that we can accurately track our imaging system, record impedances from multiple locations, and fuse all data together to reconstruct a single estimate of the 3D conductivity distribution within a ROI. All experiments were conducted in a homogenous saline bath with high-contrast inclusions. A logical next step would be to image gelatin phantoms and *ex vivo* prostates in order to explore the efficacy of this technology in a more clinically relevant scenario.

5. Conclusions

Simulations and sensitivity studies reveal that (1) TREIT measurements recorded from an end-fired probe are not sufficiently sensitive to image the whole prostate and that (2) the combination of TREIT + BP measurements recorded from multiple location can essentially cover an entire nominal 50 cm^3 prostate. Three measured tank experiments of the fd-TREIT + BP approach successfully and accurately recovered the positions of two to three metal or plastic inclusions. The measured tank experiments represent important steps in the development of an EIT reconstruction algorithm that can combine impedance data recorded from multiple locations and from multiple probes. Importantly, the current method has the potential to image a majority of a prostate (76.1%) during a routine TRUS-guided 12-core biopsy procedure. Ongoing prostate phantom work is aiming to further refine the approach for an *ex vivo* imaging study.

Acknowledgments

This work was supported in part by the Department of Defense Congressionally Directed Medical Research Program under Grant W81XWH-15-1-0102.

ORCID iDs

Ethan K Murphy https://orcid.org/0000-0002-4635-3384

References

Baumann M, Mozer P, Daanen V and Troccaz J 2012 Prostate biopsy tracking with deformation estimation *Med. Image Anal.* **16** 562–76

Borsic A, Halter R, Wan Y, Hartov A and Paulsen K D 2010 Electrical impedance tomography reconstruction for three-dimensional imaging of the prostate *Physiol. Meas.* **31** S1–16

Ching C B, Moussa A S, Li J, Lane B R, Zippe C and Jones J S 2009 Does transrectal ultrasound probe configuration really matter? end fire versus side fire probe prostate cancer detection rates *J. Urol.* **181** 2077–83

Everitt A, Manwaring P and Halter R J 2018 A real-time 4-bit imaging electrical impedance sensing biopsy needle for prostate cancer detection *Proc. SPIE* **10578** 1–10

Geselowitz D B 1971 An application of electrocardiographic lead theory to impedance plethysmography *IEEE Trans. Biomed. Eng.* **18** 38–41

Geuzaine C and Remacle J F 2009 Gmsh: a 3D finite element mesh generator with built-in pre- and post-processing facilities *Int. J. Numer. Methods Eng.* **79** 1309–31

Halter R J, Hartov A, Heaney J A, Paulsen K D and Schned A R 2007 Electrical impedance spectroscopy of the human prostate *IEEE Trans. Biomed. Eng.* **54** 1321–7

Hansen P C 1998 *Rank-Deficient and Discrete Ill-Posed Problems* (Philadelphia, PA: Society for Industrial and Applied Mathematics) (http://epubs.siam.org/doi/book/10.1137/1.9780898719697).

Harnden P, Naylor B, Shelley M D, Clements H, Coles B and Mason M D 2008 The clinical management of patients with a small volume of prostatic cancer on biopsy: What are the risks of progression? a systematic review and meta-analysis *Cancer* **112** 971–81

Harvey C J, Pilcher J, Richenberg J, Patel U and Frauscher F 2012 Applications of transrectal ultrasound in prostate cancer *Br. J. Radiol.* **85** S3–17

Khan S, Manwaring P, Borsic A and Halter R 2015 FPGA-based voltage and current dual drive system for high frame rate electrical impedance tomography *IEEE Trans. Med. Imaging* **34** 888–901

Lee B R, Roberts W W, Smith D G, Ko H W, Epstein J I, Lecksell K and Partin A W 1999 Bioimpedance: Novel use of a minimally invasive technique for cancer localization in the intact prostate *Prostate* **39** 213–8

Loke M H 2013 Tutorial: 2D and 3D electrical imaging surveys *Geotomo Software Malaysia Technical Report* 127 (http://seisweb.oma.be/bibadmin/uploads/pdf/COURSENOTES.pdf)

Murphy E K, Mahara A and Halter R J 2017a Absolute reconstructions using rotational electrical impedance tomography for breast cancer imaging *IEEE Trans. Med. Imaging* **36** 892–903

Murphy E K, Mahara A, Khan S, Hyams E S, Schned A R, Pettus J and Halter R J 2017b Comparative study of separation between *ex vivo* prostatic malignant and benign tissue using electrical impedance spectroscopy and electrical impedance tomography *Physiol. Meas.* **38** 1242–61

Murphy E, Mahara A and Halter R 2016 A novel regularization technique for microendoscopic electrical impedance tomography *IEEE Trans. Med. Imaging* **35** 1593–603

Murphy E K, Mahara A, Wu X and Halter R J 2017c Phantom experiments using soft-prior regularization EIT for breast cancer imaging *Physiol. Meas.* **38** 1262–77

Numao N, Kawakami S, Yonese J, Koga F, Saito K, Fujii Y, Ishikawa Y, Fukui I and Kihara K 2008 Three-dimensional 26-core biopsy-based patient selection criteria for nerve-sparing radical prostatectomy *Int. J. Urol.* **15** 1061–6

Salomon G *et al* 2009 The feasibility of prostate cancer detection by triple spectroscopy *Eur. Urol.* **55** 376–84

Saulnier G J, Blue R S, Newell J C, Isaacson D and Edic P M 2001 Electrical impedance tomography *IEEE Signal Process. Mag.* **18** 31–43

Shariat S F and Roehrborn C G 2008 Using biopsy to detect prostate cancer *Rev. Urol.* **10** 262–80 (PMID:19145270)

Siddiqui M M *et al* 2015 Comparison of MR/ultrasound fusion-guided biopsy with ultrasound-guided biopsy for the diagnosis of prostate cancer *JAMA* **313** 390–7

Siegel R L, Miller K D and Jemal A 2016 Cancer statistics *CA Cancer J. Clin.* **66** 7–30

Somersalo E, Cheney M and Isaacson D 1992 Existence and uniqueness for electrode models for electric current computed tomography *SIAM J. Appl. Math.* **52** 1023–40

Soni N K, Dehghani H, Hartov A and Paulsen K D 2003 A novel data calibration scheme for electrical impedance tomography *Physiol. Meas.* **24** 421–35

Syed H, Borsic A, Hartov A and Halter R J 2012 Anatomically accurate hard priors for transrectal electrical impedance tomography (TREIT) of the prostate *Physiol. Meas.* **33** 719–38

Uzzo R G, Wei J T, Waldbaum R S, Perlmutter A P, Byrne J C and Vaughan D 1995 The influence of prostate size on cancer detection *Urology* **46** 831–6

Walsh P 2007 *Campbell's Urology* (Philadelphia, PA: Saunders)

Wan Y, Borsic A, Hartov A and Halter R 2012 Incorporating a biopsy needle as an electrode in transrectal electrical impedance imaging *Proc. Annual Int. Conf. IEEE Engineering in Medicine and Biology Society EMBS* pp 6220–3

Wan Y, Halter R, Borsic A, Manwaring P, Hartov A and Paulsen K 2010 Sensitivity study of an ultrasound coupled transrectal electrical impedance tomography system for prostate imaging *Physiol. Meas.* **31** S17–29

An Analog Front End ASIC for Cardiac Electrical Impedance Tomography

Arun Rao, *Member, IEEE*, Yueh-Ching Teng, *Student Member, IEEE*, Chris Schaef, *Member, IEEE*, Ethan K. Murphy, Saaid Arshad, Ryan J. Halter, *Member, IEEE*, and Kofi Odame, *Senior Member, IEEE*

***Abstract*—In this paper, an end-to-end CMOS application specific integrated circuit (ASIC) for readout channel in a cardiac electrical impedance tomography system is presented. The ASIC consists of an integrated current driver for current injection, an instrumentation amplifier, variable gain amplifier at the analog front end for voltage readout from electrodes, and an on-chip 10-bit successive approximation register analog to digital converter with serial peripheral interface. The ASIC is fabricated in the CMOS 0.18 μm process with a supply voltage of 3.3 V. Amplitude and phase extraction of the voltages is performed in the digital domain with a matched filter. A fully integrated solution for use in multiple electrode system is demonstrated. The readout chain in the ASIC achieves a minimum signal-to-noise ratio of 71 dB over the frequency range of 500 Hz–700 kHz, while maintaining an average accuracy of 99.7%. Frame rates of 21 frames per second for a 32 electrode system is feasible, and the ASIC has an overall power consumption of 11.8 mW.**

***Index Terms*—ASIC, cardiac monitoring, current driver, electrical impedance tomography, instrumentation amplifier, matched filter, variable gain amplifier.**

I. Introduction

SELF-MANAGEMENT of chronic heart disease is hindered by three critical barriers: (i) the symptoms that patients monitor today are insensitive, non-specific and late indicators of heart failure [1]; (ii) this lack of predictive strength forces management of the condition to be reactive rather than proactive [2], [3]; (iii) single, once-a-day measurements cannot capture the patient's hemodynamic response to the stresses of daily life activities [4], [5], or the diurnal variation in sympathetic activation [6], [7], thus hindering a full understanding of the patient's condition [8], [9].

One possible solution is to use an implanted device for on-demand telemonitoring of pulmonary artery pressure [10]. Unfortunately, this approach is invasive, expensive, and risks infection, bleeding, arterial embolism, prolonged hospitalization, thrombus and cardiogenic shock, among others [11].

Manuscript received December 16, 2017; revised February 19, 2018 and April 5, 2018; accepted April 23, 2018. Date of publication June 12, 2018; date of current version August 15, 2018. This work was supported in part by the U.S. National Science Foundation under Grant 1418497, and in part by the U.S. Department of Defense CDMRP Grants W81XWH-15-1-0572 and W81XWH-15-1-0571. This work was recommended by Associate Editor A. Humeau-Heurtier. *(Corresponding author: Arun Rao.)*

The authors are with the Thayer School of Engineering, Dartmouth College, Hanover, NH 03755 USA (e-mail: arun.rao.th@dartmouth.edu; Yueh-Ching.Teng.TH@dartmouth.edu; christopher.schaef@intel.com; Ethan.K.Murphy@dartmouth.edu; Saaid.H.Arshad.TH@dartmouth.edu; ryan.j.halter@dartmouth.edu; kofi.m.odame@dartmouth.edu).

Color versions of one or more of the figures in this paper are available online at http://ieeexplore.ieee.org.

Digital Object Identifier 10.1109/TBCAS.2018.2834412

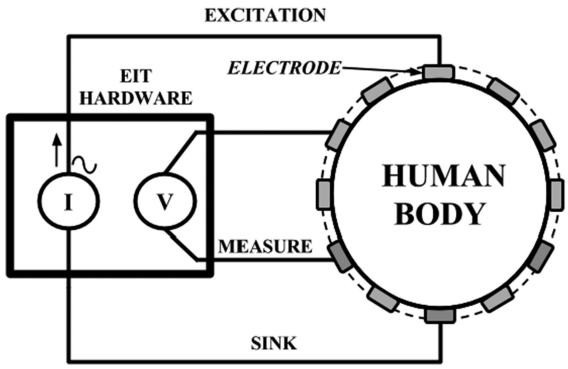

Fig. 1. Block diagram of a typical EIT system. AC current excitation is performed using a pair of electrodes and the voltages induced on the remaining electrodes are measured.

A promising, non-invasive alternative is dynamic electrical impedance tomography (EIT) of the thorax, from which left ventricular volume changes and cardiac output can be extracted. In an EIT system the tissue excitation is performed by injecting alternating current through a pair of electrodes and measuring the boundary voltages induced at the remaining electrodes as shown in Fig. 1. The excitation frequencies can be swept over a pre-determined range depending on the tissue being probed. This idea has been demonstrated previously, including in our own recent work [12] using the EIT Pioneer Set (Swisstom AG, Landquart, Switzerland). The challenge with these systems is that they are large and bulky. They may be appropriate for hospital bedside use, but they are unsuitable for telemonitoring, where physical obtrusiveness and ease of use are critical to ensuring patient adherence [13], [14].

Application specific integrated circuits (ASICs), like the one depicted in Fig. 2, could dramatically miniaturize the cardiac EIT instrumentation system, making its use more feasible in a telemonitoring environment. Unfortunately, the state-of-the-art ASICs for EIT do not meet the performance requirements necessary for cardiac output monitoring. For example, the ASICs described in [15]–[17] do not provide adequate signal-to-noise ratio.

In this paper, we present a novel analog front end ASIC that provides the signal-to-noise ratio, interrogation frequency and power consumption performance needed for a cardiac output monitoring application. Section II presents the system level

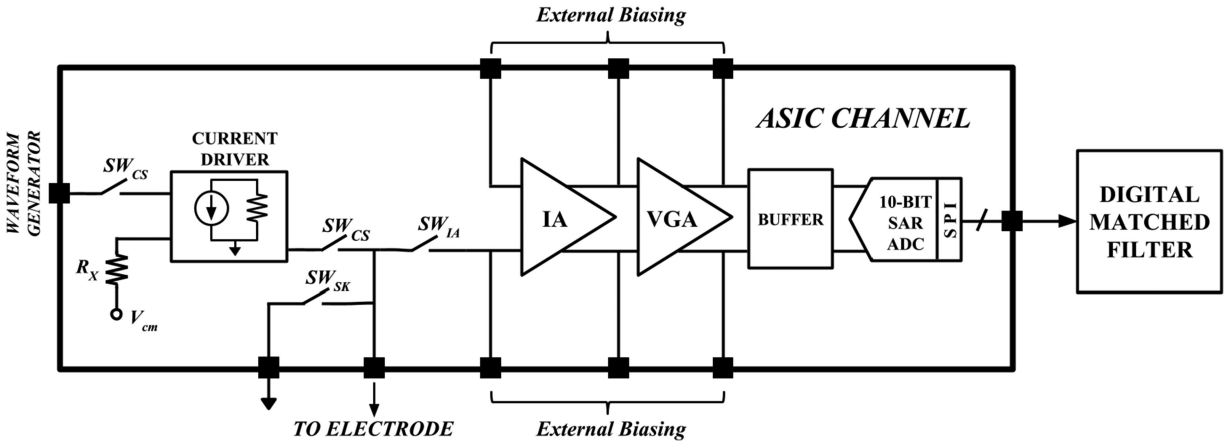

Fig. 2. Block diagram of the cardiac EIT ASIC. The on-chip switches are used to configure the channel in a current-source, current-sink or voltage-read mode. R_X is an on-chip resistor and V_{cm} is the common mode voltage of the current driver. The IA, VGA and the ADC form the voltage readout chain. The digital data from the ADC is sent off-chip using a SPI interface to a digital matched filter for amplitude extraction. Circuit blocks of the ASIC were measured individually with custom built PCBs.

specifications necessary for cardiac monitoring. Section III discusses ASIC building blocks in detail and provides a summary for measured performance. Section IV discusses the system design using the ASIC and provides measured results. Section V summarizes the performance achieved and provides concluding remarks.

II. EIT System Level Specifications

Image reconstruction in dynamic EIT aims to estimate the spatiotemporally-varying electrical properties (conductivity, σ and permittivity, ϵ) within the thorax, provided a set of boundary measurements. These measurements (small-amplitude, imperceptible AC currents that are injected into the thorax, and the resulting voltages that develop on the skin surface), carry information about the internal electrical properties. By solving the inverse problem, it is possible to reconstruct a tomography-like spatial distribution of σ and ϵ.

Over the frequency range 10 Hz to 1 MHz, the conductivity of the blood in the heart is about $\sigma_{\mathrm{h}} = 0.7$ S/m, while that of the background (heart muscle, lungs, fat, bone, etc.) is less than 0.4 S/m [18]. This contrast in electrical properties makes the blood-filled heart visible as a high conductivity region in an EIT image of the thorax. In practice, the frequency of interrogation for cardiac output measurement is at least 20 kHz, in order to avoid the high skin resistivity that would be encountered at lower frequencies [19]. Looking beyond cardiac output measurement, there are some other cardiac EIT applications that might require interrogation frequencies up to 1 MHz. These include bioimpedance spectroscopy for detecting cardiac ischemia [20], measuring fluid index ratio due to edema in congestive heart failure [21], and frequency differencing EIT for anatomic characterization, such as ventricular wall thickness [22]. Also, the entire process of making boundary measurements and constructing an EIT image (a "frame") must be performed at a rate of 14 frames per second (fps) or higher. This way, enough points are captured over the $\sim$1 s cardiac cycle such that heart volume change and cardiac output can be calculated.

To understand the remaining performance requirements of a cardiac EIT system, we made use of a highly detailed digital phantom of the human thorax. The phantom comprises the MRI and CT-based 4D XCAT model [23], mesh generation using distmesh [24] and gmsh [25], a perfusion model [26], ex-vivo tissue values of conductivity and permittivity from multiple frequencies [18], and a 3D finite element (FEM) implementation of the complete electrode [27]. We analyzed the digital phantom assuming a 32 electrode EIT system. As shown in Fig. 3, the phantom produces an image that is qualitatively similar to one constructured from measurements of a human volunteer.

Figure 4(a) shows the boundary voltage amplitudes that were generated by the digital phantom for a typical electrode position, with measurements taken at end diastole and also at end systole. Depending on the anatomy of the subject, the boundary voltages can range in amplitude from tens of millivolts to several hundred millivolts. Interestingly, the voltage measured at end diastole (when the heart is full of blood) is different from that at end systole (just after ejection of blood) by less than 1%. This small change is due to the large amounts of insulating air that are inhaled into the lungs, which confound the relatively smaller signals of blood flow in and out of the heart and cardiac muscle motion.

Since the EIT system must detect the 1% change in voltage amplitude across the systolic cycle in order to extract cardiac output, this would suggest a minimum required signal-to-noise ratio (SNR) of 40 dB. In fact, the EIT image reconstruction problem is poorly conditioned and ill-posed, and demands SNR $>$70 dB for this application. Fig. 4(c) illustrates how the EIT-derived cardiac output would deviate from ground truth if the SNR fell too low.

In summary, an EIT system for cardiac output monitoring must cover a dynamic range from 20 $\mathrm{mV_{pp}}$ to 1 $\mathrm{V_{pp}}$, operate at a frame rate of 14 fps, and maintain an SNR of $>$70 dB. In addition, it must support an interrogation frequency of a few tens of kHz, although frequencies up to 1 MHz would be useful for more generalized cardiac EIT applications. Accuracy and linearity requirements are less stringently defined, especially

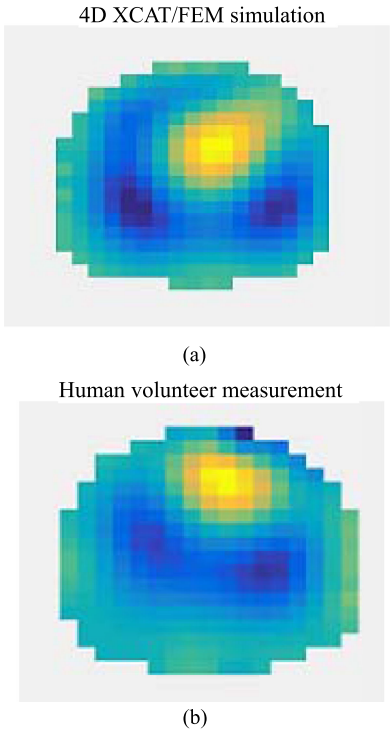

Fig. 3. Cross-sectional conductivity profile of the thorax produced from (a) Digital phantom model; and (b) Bioimpedance boundary voltage measurements of a healthy human subject. The digital phantom model and the in vivo measurements result in qualitatively very similar images, where the heart and lung (from perfusion) are very clearly seen when dynamic EIT imaging is used between end-diastole and end-systole.

with the use of the calibration techniques that we introduced in [28]. Still, it is typical to design for $\geq$99% accuracy and ≤ -40 dB total harmonic distortion [28]–[30].

III. ASIC Design and Description

In this section, we describe the different components that comprise the EIT cardiac output analog front end shown in Fig. 2.

A. Current Driver

System level specifications derived earlier indicate that cardiac monitoring requires an accuracy $\geq$99% and ≤ -40 dB total harmonic distortion. The current driver in the ASIC is capable of generating 1 mA_{pp} sinusoidal current while maintaining total harmonic distortion of $<$1% for frequencies up to 1 MHz. The accuracy of current delivered over this frequency range is $>$99.6%. Accuracy is achieved by designing the current driver with high output impedance, whereas linearity is obtained by using a resistor for voltage to current conversion. The details of the implementation are below.

The current driver for this design is based on the CCII current conveyor [32] shown in Fig. 5. To obtain high linearity, the voltage to current conversion is performed using a 2-stage op-amp in unity gain configuration with a resistor at the terminal X generating current, $I_X = \frac{V_X}{R_X}$ [33]. A class AB buffer at the output of the 2-stage op-amp creates a low impedance node, and

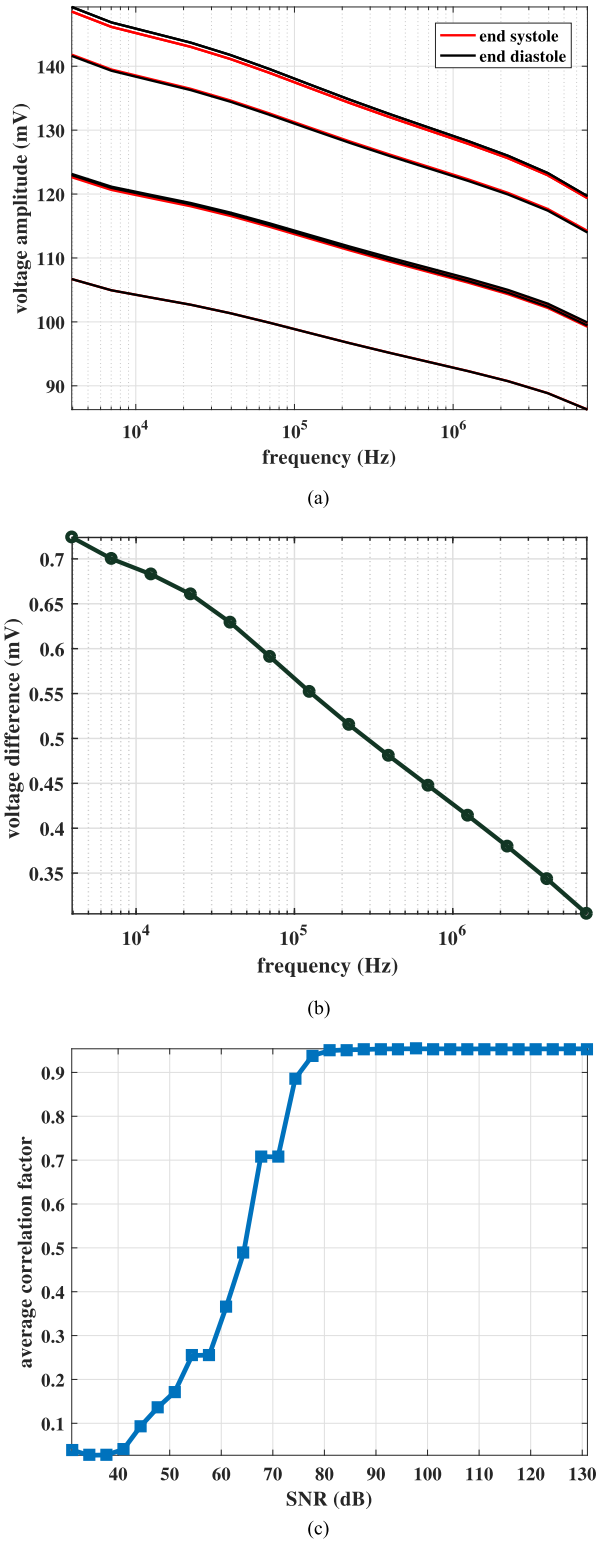

Fig. 4. (a) Boundary voltage amplitude versus frequency plot for some selected electrodes and current source-sink patterns. (b) The voltage difference between end systole and end diastole measured at the same electrode for a representative source-sink pattern from Fig. 4(a). The difference in voltage at these two time points is less than 1 mV, and decreases with frequency. (c) Effect of measurement SNR on accuracy of the extracted heart area [31]. The y-axis is the correlation factor between actual versus EIT-extracted heart area, averaged across the cardiac cycle. For accurate calculation of cardiac output, the correlation factor should ideally be 1. The plot shows that a measurement SNR of at least 75 dB is necessary for sufficiently-high correlation.

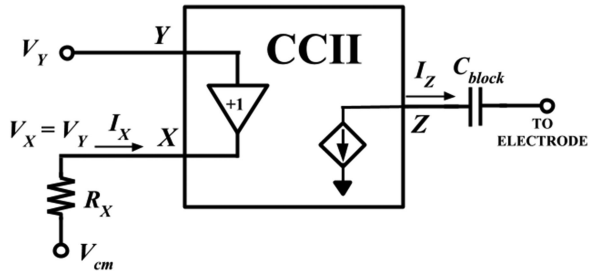

Fig. 5. Block diagram of the current conveyor architecture [32]. Current is generated at terminal X using an on-chip resistor such that $I_X = \frac{V_X}{R_X}$, where $R_X = 500\,\Omega$ and V_X follows the voltage at terminal Y. Current I_X is delivered to terminal Z with a current gain of unity.

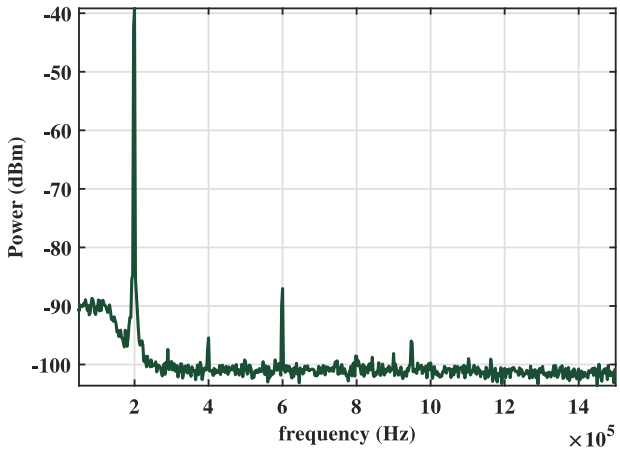

Fig. 6. FFT plot of the current driver delivering 500 μA_{pp} current to a fixed load of 500 Ω. The total harmonic distortion measured is ∼0.5% at an input frequency of 200 kHz.

TABLE I
MEASURED PERFORMANCE OF CURRENT DRIVER

Parameter	Value
Area	0.26 mm^2
Bandwidth	100 Hz - 10 MHz
Output Impedance	101 kΩ @ 1MHz
Max. Output Current	1 mA_{pp}
THD	< 0.1 % @ 50 kHz
Accuracy	99.6 % up to 1 MHz
Power	1.65 mW

the use of indirect compensation technique [34] helps achieve wide-band operation up to 10 MHz. The generated current is mirrored to the output terminal Z through a gain enhanced cascode current structure to provide high output impedance [35]–[37].

Figure 6 shows an example of the current driver's measurement results. When injecting a 200 kHz, 500 μA_{pp} current onto a 500 Ω load, the measured total harmonic distortion is 0.5%. Table I summarizes the other key performance metrics of the current driver.

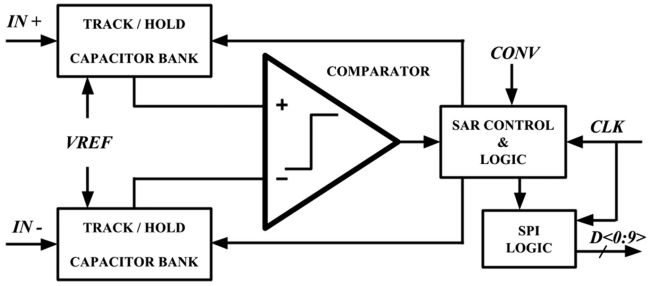

Fig. 7. Block diagram of the differential 10-bit SAR ADC. The maximum sampling rate of the ADC is 250 ksps. Serial data output is achieved by incorporating a SPI interface.

B. 10-b SAR ADC

The ADC samples the voltage readout chain and provides the digital data to an off-chip matched filter to extract the amplitude and phase. A signal-to-noise ratio of 80 dB is desirable to meet the system SNR specifications. Assuming an output-referred noise of IA, VGA chain of 1 mV_{rms} [38], 80 dB SNR can be achieved with a 10 bit ADC and 100 tap matched filter [39].

Next we discuss the sampling rate of the ADC based on the the desired frame rate of 14 fps. The frame rate is calculated by the following formula,

$$\mathrm{FR} = \frac{1}{\mathrm{P_N} \cdot \left(\frac{\mathrm{N_{tap}}}{f_s} + t_s\right)}\ (\mathrm{fps}) \tag{1}$$

where, FR represents the frame rate in frames per second, N_{tap} is the number of taps in the matched filter for amplitude extraction, P_N is the number of current source-sink patterns in a multi-electrode system, f_s is the sampling rate of the ADC and t_s is the settling time after each pattern is switched. With $N_{tap} = 100$, $P_N = 30$ for a 32 electrode system, and ideal settling time of zero, the minimum required sampling speed of the ADC is 42 ksps. In reality, the sampling rate should be higher to account for the settling time during pattern switching to obtain desired precision (see detailed discussion on frame rate in Section IV). The ADC is designed with a maximum sampling rate of 250 ksps.

An SAR ADC architecture was chosen as it exhibits lower power consumption in comparison to other ADC architectures [40]. The block diagram of the ADC designed is shown in Fig. 7. The track and hold comprises of a capacitor bank and CMOS switches controlled by the SAR logic block. An SPI interface was designed to achieve serial data output which simplifies system level design in terms of input/output infrastructure necessary when the ASIC is incorporated in a multiple electrode EIT system. The 10-bit data is available at the SPI interface after 14 clock cycles when the $CONV$ signal is asserted high. The ADC consumes an average current of 77.23 μA with a sampling rate of 250 ksps and input clock frequency of 3.5 MHz. The dynamic characteristics and measured performance parameters of the 10-bit ADC are shown in Table II.

The figure of merit for the ADC is given by (2) [41].

$$\mathrm{FOM_{ADC}} = \frac{\mathrm{P_{avg}}}{f_s \cdot 2^{\mathrm{ENOB}}}\ (\mathrm{J/conv\text{-}step}) \tag{2}$$

TABLE II
MEASURED PERFORMANCE OF 10-BIT SAR ADC

Symbol	Parameter	Value
V_{DD}	Process 0.18 μm	1.8 V
V_{IN}	Differential Input Voltage	0 - 1.2 V
F_s(max)	Sampling Rate	250 ksps
SINAD	Signal to Noise and Distortion	54.98 dB (1 kHz)
ENOB	Effective number of bits	8.84
P_{avg}	Average Power	139 μW
FOM_{ADC}	Figure of Merit	1.25 pJ/conv-step

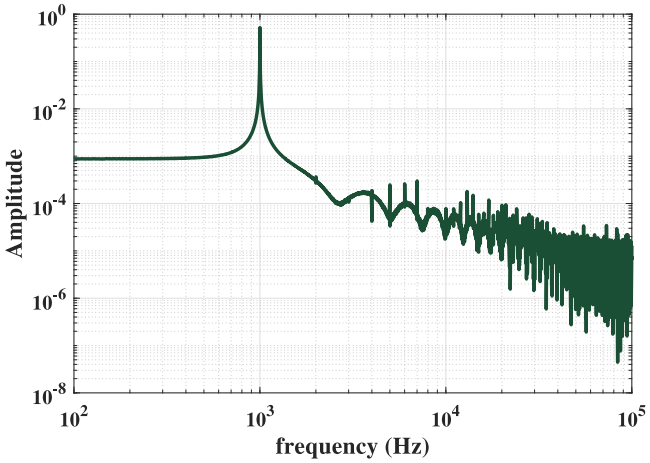

Fig. 8. FFT plot of the ADC for a 1 kHz input signal and sampling rate of 250 ksps.

where, P_{avg} is the average power, f_s is the sampling rate and ENOB represents the effective number of bits for the 10-bit SAR ADC. The ADC achieves an FOM_{ADC} of 1.25 pJ/conv-step.

The FFT plot for a 1 kHz input signal at 250 ksps sampling rate for the ADC is shown in Fig. 8.

C. Voltage Sensing Amplifiers (IA and VGA)

Boundary voltages on electrodes for a few selected current source-sink patterns are shown in Fig. 4(a). The readout chain should amplify these voltages without saturating the channel and provide high linearity (≤ -40 dB) for frequencies up to 1 MHz. The IA is designed with a fixed gain of 3 V/V, as we want to minimize noise, and prevent saturation of the readout chain. The VGA provides three additional gain settings of 1, 3 and 12 V/V. Thus, to amplify the smallest possible voltage (20 mV_{pp}), the readout chain can provide a gain of 36 V/V. The target output-referred noise specification of the IA and VGA chain is 1 mV_{rms}. With a 10-bit ADC and 100 taps in the matched filter, the circuit noise from the voltage sensing amplifiers will provide the required SNR of 80 dB (discussed in the ADC section).

The IA shown in Fig. 9 is a fully differential amplifier based on current conveyors [42]. It has a balanced structure, with high input impedance and linearity. The IA is designed for low noise operation and provides a fixed voltage gain determined by the ratio of two on-chip polysilicon resistors, R_2/R_1. The IA has a common mode rejection ratio (CMRR) over 86 dB, and a measured input-referred noise of 14 $nV_{rms}/\sqrt{Hz}$. The VGA is a fully differential amplifier which has a similar architecture and performance as the IA reported in [38]. Additionally, it has a reconfigurable gain of 0 dB, 9.5 dB and 21.5 dB to fully utilize the input dynamic range of the ADC.

For speed and power constraints, the amplifiers G in Fig. 9 only consists of a few transistors which provide proper level shifting incorporated, for the flipped source follower to increase its dynamic range. It also lowers the output impedance of the source follower, such that the transconductance stage can drive a low value gain resistor R_1 to reduce the overall amplifier noise. The V_{ref} bias voltages are set by on-chip current sources and the implementation of level-shifted source follower concept is similar to our design presented in [38], [43]. The common mode feedback (CMFB) circuit consists of a differential source follower and resistors [44] to control the gate voltage of transistors M_6 and $M_{6'}$.

The magnitude response of cascaded voltage sensing amplifiers which include IA and VGA is shown in Fig. 10. The digitally selectable gains of 9.3, 19 and 30 dB are set by the external control bits. Table III summarizes the measured performance of the IA and VGA. The measured voltage gains deviate less than ± 0.5 dB across the 3dB bandwidth. A total of 18 chips were used for this measurement. In addition the variation in gain across the frequencies of the readout chain can be calibrated out for each channel incorporated into the EIT system.

The ASIC is fabricated in the XFAB 0.18 μm CMOS process with a supply voltage of 3.3 V. The micro-photograph of the ASIC is shown in Fig. 11. The current driver, and the readout channel which contains the IA, VGA and the ADC are clearly indicated.

IV. SYSTEM DESIGN AND RESULTS

The system level block diagram of the ASIC channel is shown in Fig. 12. Necessary bias currents and reference voltages needed for the building blocks in the ASIC are provided by using current source IC's and voltage references. The input to the integrated current driver for voltage-to-current conversion is provided with a waveform generator IC, followed by an anti-aliasing filter with a cut-off frequency of 2 MHz. The output current is varied by changing the amplitude of the sinusoidal input voltage to the current driver. To sense the accurate current injected into the electrode, external sense resistors with switching mechanism is designed on the board. External ADC with anti-aliasing filter is also included as a backup. The output from the on-chip ADC and external ADC's is interfaced to a field programmable gate array (FPGA) using SPI communication protocol. The board is powered with linear dropout regulator (LDO) IC's which provide two voltage levels of 1.8 V and 3.3 V.

A. System Signal-to-Noise Ratio (SNR)

The SNR of the system indicates the noise in the readout signal chain of the EIT system. According to our analysis, the acceptable SNR for accurate cardiac output monitoring should

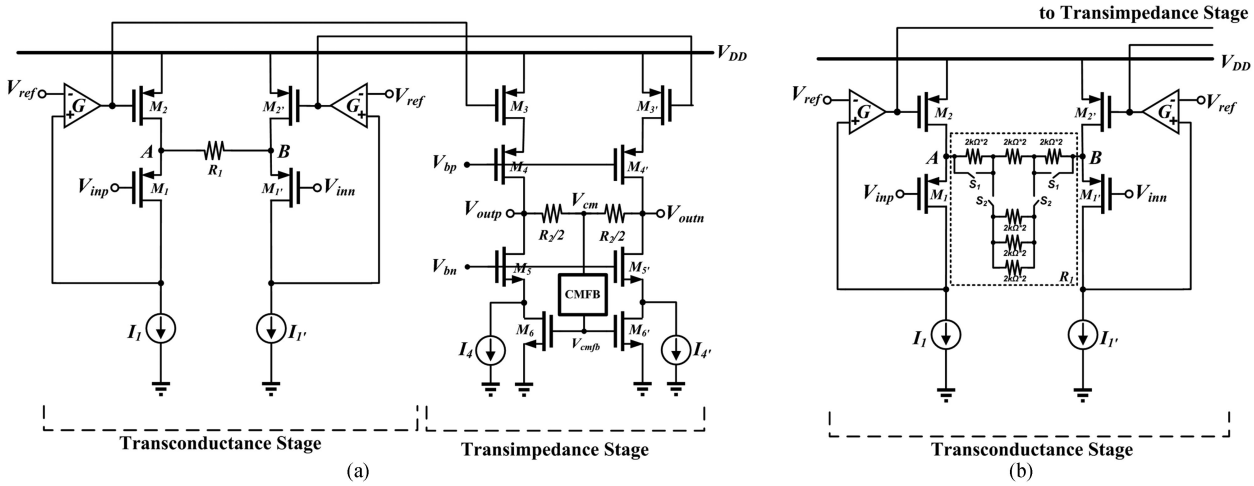

Fig. 9. (a). Simplified schematic of the current conveyor architecture used to implement the IA. The fixed gain is determined by the ratio of on-chip polysilicon resistors $R_1 = 10$ kΩ and $R_2 = 30$ kΩ. (b). The transconductance stage of the VGA is shown, while the transimpedance stage has a similar structure as the IA. Variable gains for the VGA is achieved by the on-chip resistor ladder shown in the figure. Resistor $R_2 = 15$ kΩ in the transimpedance stage is fixed while resistor R_1 in the transconductance stage is variable with values 15 kΩ, 5 kΩ and 2.5 kΩ. Digital control of variable gains is achieved using switches S_1 and S_2.

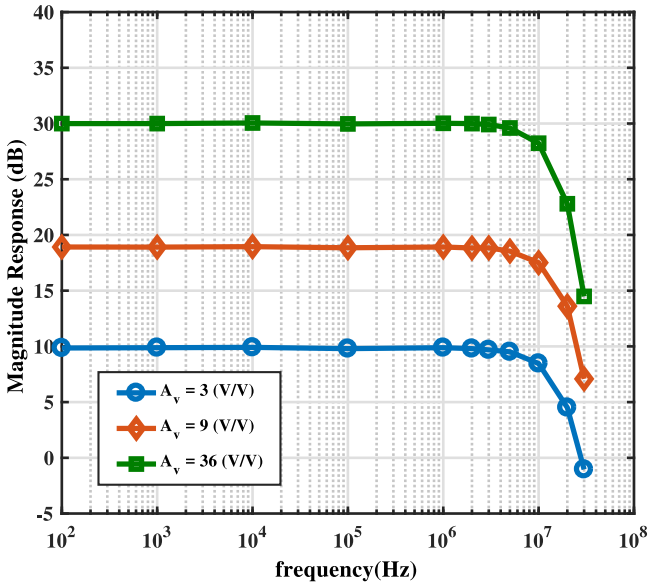

Fig. 10. Measured magnitude response of the readout channel (IA and VGA cascaded). The IA provides a fixed gain of 9.3 dB, whereas the VGA can be programmed to achieve a gain of 0, 9.3 and 21.5 dB with external control bits.

TABLE III
MEASURED IA AND VGA PERFORMANCE SUMMARY

	IA	VGA
V_{DD}	3.3 V	3.3 V
Power	2.07 mW	4.66 mW
Bandwidth	>10 MHz	>10 MHz
Input Impedance (DC)	>1 GΩ	>1 GΩ
Input Noise ($nV_{rms}/\sqrt{Hz}$)	14	80 / 27 / 6.7
Gain (dB)	9.3 (1 kHz)	0 / 9.3 / 21 (1 kHz)
THD (dB) ($V_{out,diff} = 2V$)	-63 (1 kHz)	-70 (1 kHz, A_v = 21 dB)

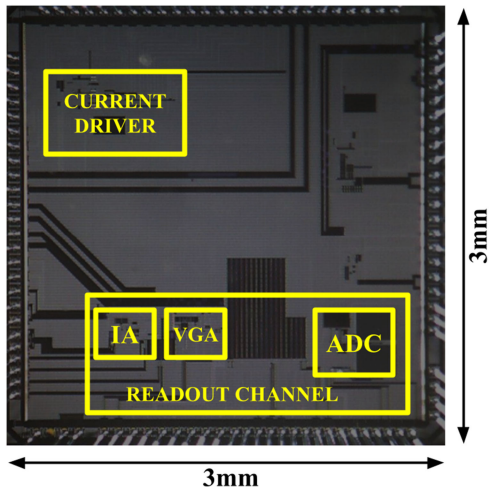

Fig. 11. Chip Micro-photograph. The current driver and the readout channel are shown.

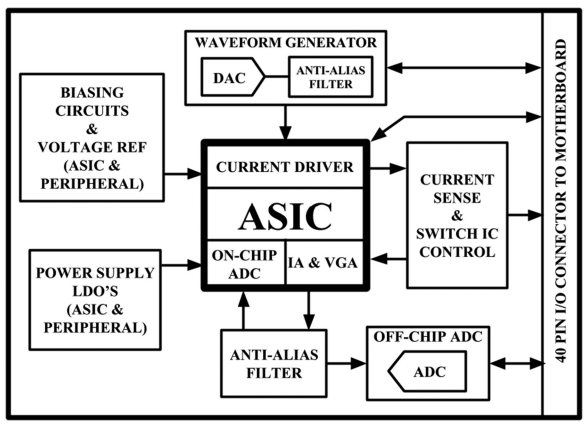

Fig. 12. Block Diagram of the PCB module. The core ASIC is shown with additional circuitry for power supply, biasing, waveform generation, current sensing, switch control, off-chip ADC, and anti-aliasing filters. The 40 pin I/O headers mounts onto a motherboard PCB and contain a large number of ground pins for signal integrity.

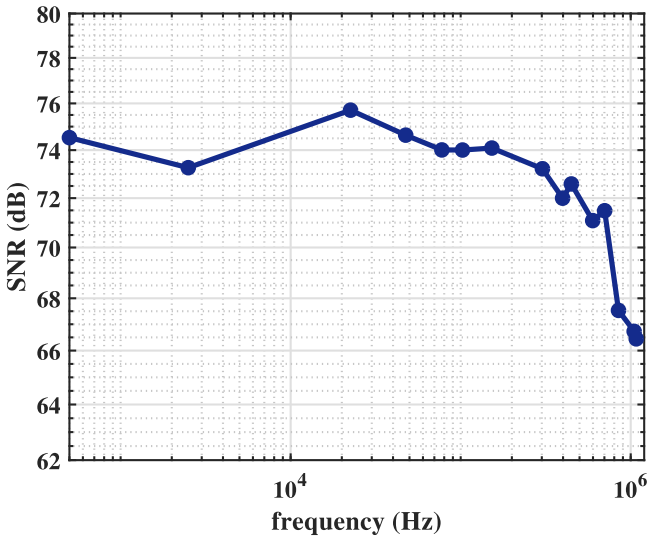

Fig. 13. Signal-to-noise ratio (SNR) at the output of the matched filter that follows the ASIC. SNR was measured using Eq. 3.

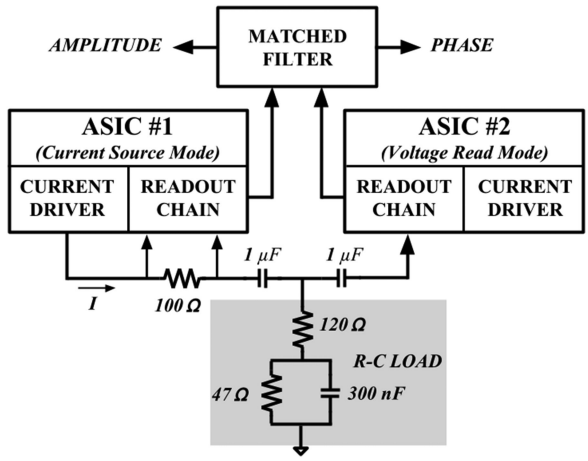

Fig. 14. Setup for obtaining Cole-Cole plot. Representative R-C load is selected via 4D XCAT simulations. Measurement is performed by two channels of the ASIC. Amplitude and phase extraction is performed in the digital domain with a matched filter. Calibration is incorporated to obtain accurate measurements.

be $\geq$70 dB. The SNR formula is given by [28].

$$\text{SNR} = 10 \cdot \log_{10} \cdot \left\{ \frac{\sum_{n=1}^{N} V_n^2}{\sum_{n=1}^{N} (V_n - \overline{V})^2} \right\} \tag{3}$$

where N is the repeated number of SNR measurements, V_n represents the measured SNR value of the signal chain, and $\overline{V}$ represents the mean of all measurements. The ASIC was configured in the voltage readout mode, and the readout channel gain settings chosen such that the ADC input dynamic range was utilized. The ADC sampling rate was set at 250 ksps and the input frequencies swept from 500 Hz to 1 MHz. The digital data from the ADC was sent off-chip and a matched filter used to extract the amplitude. To obtain the SNR of the readout signal chain, $N = 128$, repeated number of measurements were performed. The minimum SNR measured is 71 dB over a frequency range of 500 Hz–700 kHz. At frequencies >700 kHz the input amplitude had to be reduced to prevent distortion and accounts for the drop in SNR value. The measured SNR plot over frequencies of 500 Hz to 1 MHz is shown in Fig. 13.

B. Cole-Cole Plot

An R-C circuit combination is used to model the complex tissue impedance of the thorax. The representative load is chosen from simulations using the 4D XCAT model described earlier, where the voltages induced on the electrodes from select current injection patterns are analyzed across frequencies, (see Fig. 4(a)). The block diagram for the measurement of the representative complex impedance is shown in Fig. 14 which incorporates two ASIC channels. One channel is configured in the current source mode and the accurate current injected in to the R-C load is determined by measuring the voltage across the 100 Ω sense resistor. The second ASIC channel is configured in voltage read mode and measures the voltage induced on the R-C load circuit due to the injected current. In order to obtain high accuracy, a calibration method is adopted where a known value

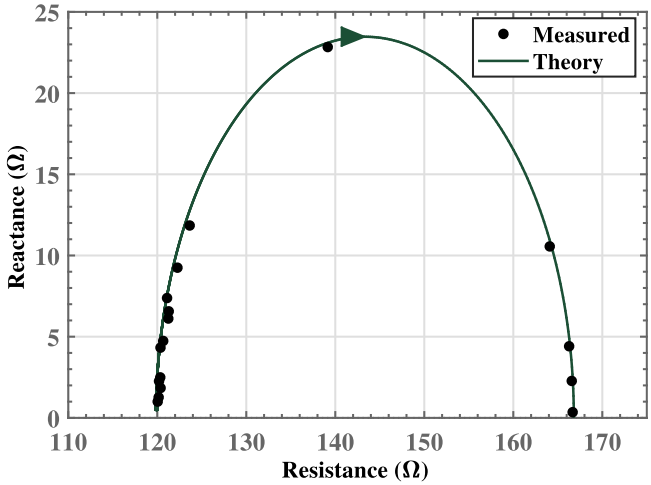

Fig. 15. Cole-Cole plot for a parallel RC load shown in Fig. 14. The measured results are compared with theory for frequencies from 250 Hz–1 MHz.

of current (500 μA) is injected into a fixed resistance (200 Ω). The R-C circuit components, sense resistor and associated parasitics are measured using a LCR meter. To ascertain the exact gain of the readout channel, gain values are incorporated from the measured results of the IA, VGA specifications over frequencies of interest. This data is saved as reference for actual measurement of load and used for calibration. The measured Cole-Cole plot for frequencies of 250 Hz–1 MHz is shown in Fig. 15. An average of 50 measurements are performed for each frequency point and the amplitude and phase are extracted using a matched filter.

Cardiac EIT systems typically have accuracies >99% as it is necessary to measure small impedance changes. The accuracy of the ASIC readout chain is calculated using Eq. 4.

$$\text{Accuracy } (\%) = \left(1 - \frac{\text{V}_{\text{meas}} - \text{V}_{\text{sim}}}{\text{V}_{\text{sim}}}\right) \cdot 100 \tag{4}$$

TABLE IV
PERFORMANCE COMPARISON OF ASIC'S FOR ELECTRICAL IMPEDANCE TOMOGRAPHY

Reference	[15]	[16]	[17]	This Work
Process	0.18 μm CMOS	0.18 μm CMOS	65 nm Mixed CMOS	0.18 μm CMOS
Frequency	up to 90 kHz	10 - 200 kHz	10 - 256 kHz	500 Hz - 700 kHz
Current Injection (peak-peak)	100 - 350 μA	0.1 - 1 mA	0.1 - 1 mA	up to 1 mA
Voltage Gain of Readout Chain (dB)	18 - 40	18 - 60 (6 dB step)	20 - 70 (6 dB step)	9.3, 19, 30
ADC (Sampling Rate)	10-bit (N/A)	10-bit (1 - 200 ksps)	10-bit (1 - 256 ksps)	10-bit (12.5 ksps - 250 ksps)
SNR (dB)	40	56.3[1]	N/A[2]	71[3]
Power (mW)	6.3	1.733	6.69	11.8[4]
FOM (pW/Hz)	700	13.27	N/A	4.75

[1] SNR averaged over measurement index [16].
[2] SNR was not reported. However, the analog matched filter approach used in [17] typically provides an SNR of less than 60 dB.
[3] The minimum achieved SNR is 71 dB over frequency range of 500 Hz - 700 kHz, whereas for the frequency range of 500 Hz - 1 MHz, the minimum achieved SNR is 66.7 dB.
[4] Breakdown of power is as follows. The current driver consumes 1.65 mW, IA and VGA consume 6.73 mW, and the ADC and its driver consume 3.44 mW.

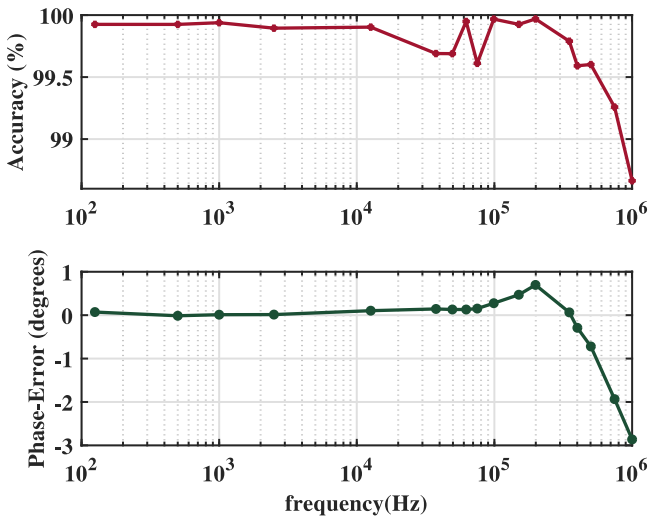

Fig. 16. Accuracy of measured amplitude and phase error over frequencies.

where V_{meas} is the measured voltage and V_{sim} is the voltage obtained from theory. The measured amplitude accuracy and phase error over frequencies is plotted in Fig. 16. An average accuracy of 99.7% is obtained for the measurement of complex impedance amplitude.

C. Frame Rate

To detect the change of heart volume and for accurate cardiac output monitoring the frame rate should exceed 14 fps as shown in our discussion earlier. The frame rate for the system is calculated by (1). It is typical in Swisstom systems and EIDORS modeling [45] to utilize skip patterns for single-ended voltage measurements. In a 32 electrode system using skip patterns, $P_N = 30$. The settling behavior after pattern switching can be studied with the help of the circuit used for measuring the complex impedance shown in Fig. 14. The RC time constant is determined by the DC blocking capacitor (1 μF) and the resistive load (167 Ω). To achieve a 10 bit resolution the voltage at the load requires 7 time constants [46] to settle. N_{tap} is set to 100 and the ADC is sampled at 250 ksps. Frame rates of $\sim$21 fps is feasible with the designed ASIC.

D. Comparison

Table IV summarizes the performance of this work with previously reported literature on EIT ASIC's. A figure of merit for the ASIC channel is defined by (5) [47],

$$\text{FOM} = \frac{\text{Power}}{\text{BW} \cdot 10^{\left(\frac{\text{SNR}}{20}\right)}} \ (\text{W/Hz}) \tag{5}$$

where, Power is the average power consumption per ASIC channel, BW is the bandwidth of the system, and SNR is the minimum signal to noise ratio in decibels over frequency range of 500 Hz–700 kHz. As seen in Table IV the ASIC used for cardiac output measurements in this work is more power efficient than other designs with the lowest FOM of 4.75 pW/Hz. This is achieved by designing an IA and a VGA with wider swing, lower noise and high linearity [38], [43].

V. CONCLUSION

The cardiac EIT system consists of several components such as the analog front-end for signal processing, the digital domain for single point impedance computation, FPGA block for control and communication strategies and reconstruction software to obtain the final image of the thorax. Some of the challenges associated are the signal processing on the ASIC up to 1 MHz, control strategies for electrode switching using FPGA, and robust board design for maintaining signal integrity. This paper measures the performance of the analog chain alone, without it being confounded by other components of the EIT system.

An ASIC with all analog front end components of a cardiac EIT system is fabricated in the CMOS 0.18 μm technology and individual blocks are characterized. The integrated current driver delivers currents up to 1 mA_{pp} while maintaining a THD of $<1\%$. The voltage sensing amplifiers provide gains of 9.3, 19 and 30 dB to process the dynamic range of voltages incident on the electrodes. The readout chain in the ASIC achieves a minimum SNR of 71 dB over frequency range of 500 Hz–700 kHz at the output of the matched filter. An average accuracy of 99.7% is measured by incorporating a representative R-C circuit and calibration scheme. Frame rates of 21 fps are feasible for a 32 electrode system for single ended measurements. The use of power efficient SAR ADC with serial interface for data acquisition enables the ASIC to be used in a multiple electrode EIT system for cardiac output monitoring. The ASIC achieves the desired SNR, frame rate and accuracy specifications with a power consumption of 11.8 mW.

REFERENCES

[1] S. R. Toukhsati, A. Driscoll, and D. L. Hare, "Patient self-management in chronic heart failure establishing concordance between guidelines and practice," *Cardiac Failure Rev.*, vol. 1, no. 2, pp. 128–131, 2015.

[2] A. Hasan and V. Paul, "Telemonitoring in chronic heart failure," *European Heart J.*, vol. 32, no. 12, pp. 1457–1464, Jun. 2011.

[3] P. B. Adamson *et al.*, "Ongoing right ventricular hemodynamics in heart failure: Clinical value of measurements derived from an implantable monitoring system," *J. Amer. College Cardiology*, vol. 41, no. 4, pp. 565–71, Feb. 2003.

[4] A. Sherwood, J. McFetridge, and J. S. Hutcheson, "Ambulatory impedance cardiography: A feasibility study," *J. Appl. Physiol. (Bethesda, Md. : 1985)*, vol. 85, no. 6, pp. 2365–2369, Dec. 1998.

[5] A. D. Goedhart, N. Kupper, G. Willemsen, D. I. Boomsma, and E. J. de Geus, "Temporal stability of ambulatory stroke volume and cardiac output measured by impedance cardiography," *Biol. Psychology*, vol. 72, no. 1, pp. 110–117, Apr. 2006.

[6] F. Lechin, B. van der Dijs, and A. E. Lechin, "Autonomic nervous system assessment throughout the wake-sleep cycle and stress," *Psychosomatic Med.*, vol. 66, no. 6, pp. 974–976, Nov. 2004.

[7] A. P. J. van Eekelen, J. H. Houtveen, and G. A. Kerkhof, "Circadian variation in base rate measures of cardiac autonomic activity," *Eur. J. Appl. Physiol.*, vol. 93, no. 1–2, pp. 39–46, Oct. 2004.

[8] M. Metra, "Use of cardiopulmonary exercise testing with hemodynamic monitoring in the prognostic assessment of ambulatory patients with chronic heart failure," *J. Amer. College Cardiology*, vol. 33, no. 4, pp. 943–50, Mar. 1999.

[9] G. Cybulski, *Ambulatory Impedance Cardiography : The Systems and Their Applications*. Berlin, Germany: Springer, 2010.

[10] J. T. Heywood *et al.*, "Impact of practice-based management of pulmonary artery pressures in 2000 patients implanted with the CardioMEMS sensor," *Circulation*, vol. 135, no. 16, pp. 1509–1517, Apr. 2017.

[11] W. T. Abraham *et al.*, "Wireless pulmonary artery haemodynamic monitoring in chronic heart failure: A randomised controlled trial," *Lancet*, vol. 377, no. 9766, pp. 658–666, Feb. 2011.

[12] E. K. Murphy, S. H. Arshad, and R. J. Halter, "Cardio-respiratory gated electrical impedance tomography for monitoring stroke-volume," in *Proc. 18th Int. Conf. Biomed. Appl. Electric. Impedance Tomography*, Jun. 2017, p. 22.

[13] B. K. Hensel, G. Demiris, and K. L. Courtney, "Defining obtrusiveness in home telehealth technologies: A conceptual framework," *J. Amer. Med. Informat. Assoc.*, vol. 13, no. 4, pp. 428–431, Jul. 2006.

[14] J. H. M. Bergmann and A. H. McGregor, "Body-worn sensor design: What do patients and clinicians want?" *Ann. Biomed. Eng.*, vol. 39, no. 9, pp. 2299–2312, Sep. 2011.

[15] L. Yan, J. Bae, S. Lee, T. Roh, K. Song, and H. J. Yoo, "A 3.9 mW 25-electrode reconfigured sensor for wearable cardiac monitoring system," *IEEE J. Solid-State Circuits*, vol. 46, no. 1, pp. 353–364, Jan. 2011.

[16] S. Hong, J. Lee, J. Bae, and H. J. Yoo, "A 10.4 mW electrical impedance tomography SoC for portable real-time lung ventilation monitoring system," *IEEE J. Solid-State Circuits*, vol. 50, no. 11, pp. 2501–2512, Nov. 2015.

[17] M. Kim *et al.*, "A 1.4-mΩ sensitivity 94-dB dynamic-range electrical impedance tomography SoC and 48-channel hub-SoC for 3-D lung ventilation monitoring system," *IEEE J. Solid-State Circuits*, vol. 52, no. 11, pp. 2829–2842, Nov. 2017.

[18] D. Andreuccetti, R. Fossi, and C. Petrucci, "An internet resource for the calculation of the dielectric properties of body tissues in the frequency range 10 Hz–100 GHz," 1997.

[19] E. T. McAdams, J. Jossinet, A. Lackermeier, and F. Risacher, "Factors affecting electrode-gel-skin interface impedance in electrical impedance tomography," *Med. Biol. Eng. Comput.*, vol. 34, no. 6, pp. 397–408, Nov. 1996.

[20] M. M. Gebhard, E. Gersing, C. J. Brockhoff, P. A. Schnabel, and H. J. Bretschneider, "Impedance spectroscopy: A method for surveillance of ischemia tolerance of the heart," *Thoracic Cardiovascular Surgeon*, vol. 35, no. 1, pp. 26–32, Feb. 1987.

[21] B. C.-H. Kwan *et al.*, "Bioimpedance spectroscopy for the detection of fluid overload in Chinese peritoneal dialysis patients," *J. Int. Soc. Peritoneal Dialysis*, vol. 34, no. 4, pp. 409–16, Jun. 2014.

[22] A. Adler and A. Boyle, "Electrical impedance tomography: Tissue properties to image measures," *IEEE Trans. Biomed. Eng.*, vol. 64, no. 11, pp. 2494–2504, Nov. 2017.

[23] W. P. Segars, G. Sturgeon, S. Mendonca, J. Grimes, and B. M. W. Tsui, "4D XCAT phantom for multimodality imaging research," *Med. Phys.*, vol. 37, no. 9, pp. 4902–4915, Aug. 2010.

[24] P.-O. Persson and G. Strang, "A simple mesh generator in MATLAB," *SIAM Rev.*, vol. 46, no. 2, pp. 329–345, Jan. 2004.

[25] C. Geuzaine and J.-F. Remacle, "Gmsh: A 3-D finite element mesh generator with built-in pre- and post-processing facilities," *Int. J. Numer. Methods Eng.*, vol. 79, no. 11, pp. 1309–1331, Sep. 2009.

[26] F. Braun *et al.*, "Aortic blood pressure measured via EIT: investigation of different measurement settings," *Physiological Meas.*, vol. 36, no. 6, pp. 1147–1159, Jun. 2015.

[27] A. Borsic, A. Hartov, K. D. Paulsen, and P. Manwaring, "3D electric impedance tomography reconstruction on multi-core computing platforms," in *Proc. IEEE 30th Annu. Int. Conf. Eng. Med. Biol. Soc.*, Aug. 2008, pp. 1175–1177.

[28] R. J. Halter, A. Hartov, and K. D. Paulsen, "A broadband high-frequency electrical impedance tomography system for breast imaging," *IEEE Trans. Biomed. Eng.*, vol. 55, no. 2, pp. 650–659, Feb. 2008.

[29] R. Cook, G. Saulnier, D. Gisser, J. Goble, J. Newell, and D. Isaacson, "ACT3: A high-speed, high-precision electrical impedance tomograph," *IEEE Trans. Biomed. Eng.*, vol. 41, no. 8, pp. 713–722, Aug. 1994.

[30] A. Hartov *et al.*, "A multichannel continuously selectable multifrequency electrical impedance spectroscopy measurement system," *IEEE Trans. Biomed. Eng.*, vol. 47, no. 1, pp. 49–58, Jan. 2000.

[31] E. K. Murphy, R. J. Halter, and K. Odame, "Simulation study for the design of an EIT system for cardiac output monitoring," in *Proc. 41st Annu. Northeast Biomed. Eng. Conf.*, Apr. 2015, pp. 1–2.

[32] A. Sedra and K. Smith, "A second-generation current conveyor and its applications," *IEEE Trans. Circuit Theory*, vol. CT-17, no. 1, pp. 132–134, Feb. 1970.

[33] I. Jivet and B. Dragoi, "On-electrode autonomous current generator for multi-frequency EIT," *Physiological Meas.*, vol. 29, no. 6, pp. S193–S201, Jun. 2008.

[34] V. Saxena and R. Baker, "Indirect feedback compensation of CMOS Op-Amps," in *Proc. IEEE Workshop Microelectron. Electron Devices*, 2006, pp. 3–4.

[35] A. Sedra, G. Roberts, and F. Gohh, "The current conveyor: History, progress and new results," *IEEE Proc. G Circuits, Devices Syst.*, vol. 137, no. 2, pp. 78–87, Apr. 1990.

[36] E. Sackinger and W. Guggenbuhl, "A high-swing, high-impedance MOS cascode circuit," *IEEE J. Solid-State Circuits*, vol. 25, no. 1, pp. 289–298, Feb. 1990.

[37] A. Zeki and H. Kuntman, "Accurate and high output impedance current mirror suitable for CMOS current output stages," *Electron. Lett.*, vol. 33, no. 12, pp. 1042–1043, Jun. 1997.

[38] Y.-C. Teng and K. M. Odame, "A 10 MHz 85 dB dynamic range instrumentation amplifier for electrical impedance tomography," *in Proc. IEEE Biomed. Circuits Syst. Conf.*, Oct. 2014, pp. 632–635.

[39] E. K. Murphy, M. Takhti, J. Skinner, R. J. Halter, and K. Odame, "Signal-to-noise ratio analysis of a phase-sensitive voltmeter for electrical impedance tomography," *IEEE Trans. Biomed. Circuits Syst.*, vol. 11, no. 2, pp. 360–369, Apr. 2017.

[40] N. Verma and a. P. Chandrakasan, "An ultra low power ADC for wireless micro-sensor applications," *Electr. Eng. Comput. Sci.*, vol. Master, pp. 143–147, 2005.

[41] R. H. Walden, "Analog-to-digital converter survey and analysis," *IEEE J. Sel. Areas Commun.*, vol. 17, no. 4, pp. 539–550, Apr. 1999.
[42] B. Wilson, "Universal conveyor instrumentation amplifier," *Electron. Lett.*, vol. 25, no. 7, pp. 470–471, 1989.
[43] Y.-C. Teng, M. Takhti, and K. M. Odame, "A power adaptive variable gain instrumentation amplifier for electrical impedance tomography," in *Proc. IEEE Biomed. Circuits Syst. Conf.*, Oct. 2015, pp. 1–4.
[44] B. Razavi, *Design of Analog CMOS Integrated Circuits*. New York, NY, USA: McGraw-Hill, 2003.
[45] "EIDORS : Electrical Impedance Tomography and Diffuse Optical Tomography Reconstruction Software," [Online]. Available: http://eidors3d.sourceforge.net/
[46] T. Corrigan, "AN-1024 APPLICATION NOTE : How to Calculate the Settling Time and Sampling Rate of a Multiplexer." [Online]. Available: http://www.analog.com/media/en/technical-documentation/application-notes/AN-1024.pdf
[47] S.-Y. Peng *et al.*, "A power-efficient reconfigurable OTA-C filter for low-frequency biomedical applications," *IEEE Trans. Circuits Syst. I, Reg. Papers*, vol. 65, no. 2, pp. 543–555, Feb. 2018.

Arun Rao (M'16) received the B.E degree from Bangalore University, Bengaluru, India, and the M.S. degree in electrical engineering from Utah State University, Logan, UT, USA. He is currently working toward the Ph.D with the Thayer School of Engineering, Dartmouth College, Hanover, NH, USA. He is interested in small form factor hardware system design and novel circuits for biomedical instrumentation and image sensors.

Yueh-Ching Teng (S'17) received M.Sc degree in electrical and computer engineering from Ohio State University, Columbus, OH, USA, in 2011. He is currently working toward the Ph.D. degree with Thayer School of Engineering, Dartmouth, Hanover, NH, USA. From 2011 to 2012, he was a Research Assistant Engineer with the ElectroScience Laboratory where he worked on analog/mixed-signal circuit designs for RFID applications. In 2017, he was an analog design intern at Texas Instruments, Manchester, USA. His current research interests are in the field of read-out amplifier design for biomedical applications, sensor interface, and power management circuits.

Christopher Schaef (M'16) received the B.S and M.S. degrees in industrial engineering from Helmut-Schmidt University, Hamburg, Germany, in 2010 and 2011, respectively and the Ph.D. degree from Dartmouth College, Hanover, NH, USA, 2016. He is currently a Power Delivery Researcher with the Circuits Research Laboratory, Intel Corporation, Santa Clara, CA, USA. His research interests are in integrated power management, energy harvesting, and hybrid dc-dc converters.

Ethan Murphy received the B.S and M.S degree from Worcester Polytechnic Institute, Worcester, MA, USA, in 2002 and Ph.D degree in all mathematics from Colorado State University, Fort Collins, CO, USA, in 2007. Prior coming to Dartmouth in 2014, he worked in industry and academic positions. He is currently a Research Scientist with the Thayer School of Engineering, Dartmouth College, Hanover, NH, USA. His interests are in inverse problems, specifically electrical impedance tomography, medical imaging, data fusion, and error analysis.

Saaid Arshad received the AB degree in engineering sciences from Dartmouth College, Hanover, NH, USA, in 2014. He is currently working toward the Ph. D. degree with the Thayer School of Engineering, Dartmouth College, Hanover, NH, USA, under Assistant Professor of Engineering Ryan J. Halter. He is interested in applications of electrical impedance tomography to cardiovascular physiology, image processing, and medical imaging.

Ryan J. Halter (M'05) is an Assistant Professor of Engineering with the Thayer School of Engineering, Dartmouth College, Hanover, NH, USA. His research interests are in biomedical instrumentation, medical imaging, electrical impedance tomography and spectroscopy, tissue bioimpedance, cancer detection technologies, traumatic brain injury, medical robotics, and image guidance.

Kofi Odame (S'06–M'08–SM'15) is an Associate Professor of electrical engineering with the Thayer School of Engineering Dartmouth College, Hanover, NH, USA. His primary interest is in analog integrated circuits for nonlinear signal processing. This work has applications in low-power electronics for implantable and wearable biomedical devices, as well as in autonomous sensor systems.

Noise-robust Bioimpedance Approach for Cardiac Output Measurement

Ethan K. Murphy[1], Justice Amoh[1], Saaid H. Arshad[1], Ryan J. Halter[1,2], and Kofi Odame[1]

E-mail: ethan.k.murphy@dartmouth.edu
November 2018
[1]Thayer School of Engineering, Dartmouth College, Hanover, NH 03755, USA
[2]Geisel School of Medicine, Dartmouth College, Hanover, NH 03755, USA

Abstract. *Objective.* Congestive heart failure is a problem effecting millions of Americans. A continuous, non-invasive, telemonitoring device that can accurately monitor cardiac metrics could greatly help this population, *reducing unnecessary hospitalizations and cost. Approach.* Deep neural networks (DNN) trained on electrical-impedance tomography (EIT) data are presented for portable cardiac monitoring. The approach was validated on a simulated thorax and a measured tank experiment. A highly detailed 4D chest model (finite element method mesh and conductivity profiles) was developed utilizing the 4D XCAT phantom to provide realistic data. The DNNs were trained using databases that assumed the presence of poorly contacting electrodes. The bad electrodes were either known or unknown, and the trained DNNs were compared to EIT evaluated with and without removing bad electrodes. *Main results.* The neural network approach was found to be robust to poorly contacting electrodes while not needing to know which electrodes were in poor contact. Overall, average errors for the DNN (without knowledge of bad electrodes) and EIT (that removed bad electrodes) were 1.8% and 4.8% (1 to 4 bad electrodes) in simulation and 4.0% and 3.7% (with 3 bad electrodes) in measurements, respectively. *Significance.* Although, the DNN is not always better than EIT (with bad electrodes removed), the comparable results without needing *a priori* knowledge of which electrodes are bad is seen as a very promising feature. An evaluation of computational costs showed that the DNN required about 20× less floating point operations and 12× less required memory storage, which could make the DNNs an attractive algorithm for a low-power, portable system. This work represents an important validation of the method using measured data, and model development, which is needed to apply this method on real clinical data. Additionally, the developed 4D simulated thorax model could be an important tool within the EIT community.

Keywords: Electrical impedance tomography, deep neural network, cardiac monitoring, cardiac output, noise modeling.

1. Introduction

Congestive heart failure (CHF) currently affects an estimated 5.8 million Americans, making it one of the most common reasons why those aged 65 and over are hospitalized [1]. Adverse cardiac events account for more than 1 million hospitalizations per year in the United States [2, 3]. With a growing proportion of the population living with some form of heart failure, the ability to pro-actively and accurately monitor cardiovascular health is crucial. Telemonitoring is becoming increasingly important to proactively address this growing need [3, 4, 5]. The primary metric of interest is cardiac output (CO) ([6, 7, 8]). CO is the product of heart-rate (HR) and stroke volume (SV), where stroke volume is the difference between the maximum and minimum left ventricular (LV) volume. A promising technology to non-invasively and continuously monitor CO is electrical impedance tomography (EIT). EIT uses multiple bioimpedance measurements recorded from electrodes placed around the chest, and, generally, uses physics-based approaches to recover the conductivity, which has been shown to correlate well with SV in several studies [9, 10, 11]. We have been developing a wearable EIT system for continuous monitoring of CO with low power constraints and potential smart-phone compatibility [12, 13].

Although EIT appears more promising than commercial electrical bioimpedance systems based on the sophisticated modeling of EIT, there remain significant concerns of error due to several sources: here we focus on one of the primary sources of errors in wearable systems, electrode contact issues, i.e. 'bad' electrodes. There have been a number of studies that have attempted to address this problem by 1) compensating for bad electrodes by simultaneously solving for both internal conductivity and the electrode contact impedances [14, 15, 16], 2) automatically detecting bad electrodes and simply removing them [17, 18], or 3) automatically detecting bad electrodes and adjusting their measurements in some way to mitigate their effect [19, 20, 21]. It was concluded in [14] that the simultaneous reconstruction of conductivity and contact impedance was not practical in situations without a homogeneous (or known) measured reference frame. In [19] bad electrodes are compensated by increasing the measurement variance of respective measurements, in [20] a similar approach was used but the data was also 'cleaned' with a projection technique, and in [21] a Grey model based on a time-series of data was used to estimate data from bad electrodes. Simply removing measurements corresponding to bad electrodes appears to be a very practical solution that results in good reconstructions. The main challenge is in reliably determining which electrodes are bad. This becomes increasingly challenging as more electrodes are bad, e.g. the work in [19] could only reliably detect up to 2 bad electrodes.

In this paper, we introduce a new bioimpedance-based method powered by deep neural networks (DNN) for measuring cardiac output (and left ventricular (LV) volume in general) that is robust to the presence of faulty electrodes. Our approach uses the same measurement data as EIT. However, instead of initially using the data to reconstruct an EIT image, from which LV volume is calculated, our novel method

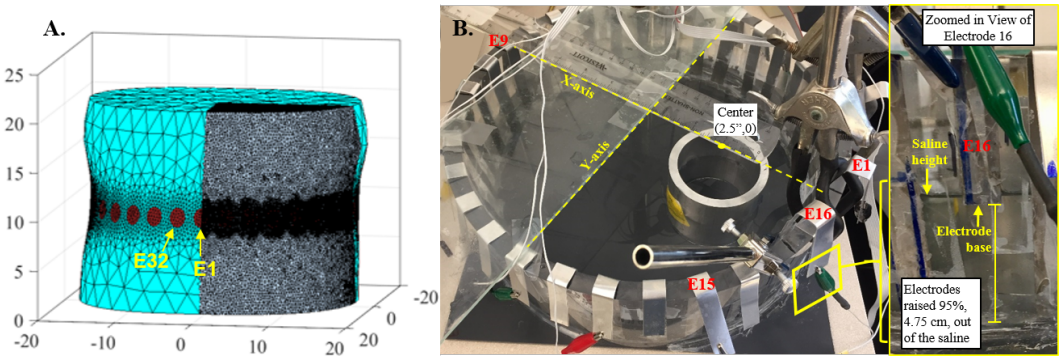

Figure 1. A. FEM mesh produced from 4D XCAT. The coarse mesh (cyan) is a surface mesh produced in distmesh with encoded electrodes, and the fine mesh (black) is the output 3D mesh from gmsh. B. The saline tank experiment with 16 electrodes connected to an EIT system (on a 32 electrode tank). Clamps were used to hold the electrodes partially out of the saline, simulating partially contacting electrodes.

inputs the data to a noise-robust deep neural network (DNN) regression model, which directly extracts LV volume information. The method is compared to EIT (with and without bad electrodes removed) on a simulated chest phantom (Fig 1A) and a measured saline tank experiment (Fig. 1B). The simulated thorax model built upon a sophisticated 4D thorax model ([24]) could be a useful tool within the EIT community. The DNN approach provides similar results to EIT (with bad electrodes removed) without requiring knowledge of which electrodes are bad for up to 4 electrodes and 3 electrodes in simulated and measured data, respectively.

This paper continues with the description of 1) traditional EIT, 2) parameter selection and the linear regression model for EIT, 3) the simulated thorax model, 4) the experiments, and 5) the DNN design and (testing and training) databases. Results of both experiments are then discussed along with a comparison on the number of floating point operations (FLOPS) and memory needed for the EIT and DNN approaches. Future development needed for this approach to work successfully on clinical data are discussed, and conclusions are summarized.

2. Methods

2.1. Traditional EIT

2.1.1. Forward problem The forward problem relies on solving the generalized Laplace equation,

$$\nabla \cdot \sigma \nabla u = 0, \tag{1}$$

over the entire domain, where σ is the conductivity and u is the electric potential. The complete electrode model (CEM) is used to realistically account for discrete electrodes [22]. The forward problem calculates the electric potential distribution throughout the domain and voltages on the electrodes assuming the conductivity and applied currents on the electrodes are known. The CEM boundary conditions additionally specify each

electrode's contact impedance and assume that current only flows in or out of the system through the electrodes. The solution to the forward problem is calculated in 3D using the finite element method (FEM) with linear basis elements [23].

2.1.2. Inverse Methods A standard Gauss-Newton algorithm is employed using Laplace-smoothing Tikhonov regularization. The aim is to minimize the following objective function

$$\arg\min_{\delta\sigma} \|\mathbf{J}\delta\sigma - (\mathbf{v}_{Test} - \mathbf{v}_{Ref})\|^2 + \alpha\|\mathbf{L}\delta\sigma\|^2, \tag{2}$$

where $\delta\sigma$ is a perturbation from some estimated or known conductivity, $\mathbf{J}$ is the Jacobian, α is the Tikhonov parameter, $\mathbf{L}$ is the regularization matrix, and $\mathbf{v}_{Test}$ and $\mathbf{v}_{Ref}$ are the test and reference voltages, respectively. Here only difference images are considered. This problem can be solved directly via the following formula

$$\delta\sigma = \left(\mathbf{J}^T\mathbf{J} + \alpha\mathbf{L}^T\mathbf{L}\right)^{-1}\mathbf{J}^T(\mathbf{\Delta v}), \tag{3}$$

where $\mathbf{v}_{Test} - \mathbf{v}_{Ref} = \mathbf{\Delta v}$.

2.2. Parameter Selection and Linear Regression for EIT

In the experiments, linear regression is applied to the reconstructed heart areas or inclusion diameters from thresholded EIT images and the true values. A two-step optimization strategy was performed to find the best Tikhonov and threshold values. Specifically, we searched over a set of possible Tikhonov parameters ranging from $1e-3$ to $1e4$, where for each value a 1-D minimization procedure was performed on the RMS error of the linear regression resulting from the threshold value. At each threshold the heart area was determined by calculating the area, A_{rec}, of all the voxels above the threshold. The reconstructed inclusion diameter (for the tank experiment) was defined as the diameter of the circle that yielded the reconstructed area, i.e. $d_{rec} = 2\sqrt{A_{rec}/\pi}$.

2.3. Simulated Thorax

The model for simulated thorax data is based on the 4D XCAT model, which is a highly detailed extended cardiac-torso model that is based on visible human anatomical data, 4D cardiac-gated multi-slice CT data, 3D MRI data, and 4D respiratory-gated multi-slice CT data [24]. Non-uniform rational basis splines are used to model individual anatomical tissues/organs that are 4D. Multiple parameters within the model can be adjusted. In this study, a single cardiac cycle of 11 frames is considered with a fixed chest size (that is, assuming a breath-hold). At any time frame, the XCAT model provides the FEM model with the exterior of the domain and interior labels so that accurate conductivity distributions can be produced. The exterior boundary of the domain is approximated using a combined Fourier series and radial-basis-functions (RBF), i.e. it

extends a common Fourier series for 2D-chest approximations ([25, 26]) into 3D. The boundary model is given by

$$r_S(\theta, z) = r_0 + \sum_{j=1}^{9} \left[exp\left(-\frac{(z - z_{c,j})^2}{\sigma_z^2} \right) \sum_{n=1}^{8} \left(a_{j,n} cos(n\theta) + b_{j,n} sin(n\theta) \right) \right], \quad (4)$$

where there are 9 linearly spaced RBF centers from the bottom to top of the chest. The weights $(a_{j,n}, b_{j,n})_{j,n=1}^{9,8}$ can be solved using a straight forward linear least squares implementation given a sufficient number of boundary points. Furthermore, the electrodes (assumed equally spaced) are encoded in the mesh via construction of an initial coarse 2D surface mesh using distmesh (see Fig 1A, [27]). The coarse 2D surface mesh is then input to Gmsh ([28]) to construct the full 3D mesh of approximately 360k nodes and 1.9M elements. A slightly less dense mesh is used for the Jacobian calculation for EIT reconstructions so that no inverse crime is committed [29].

The initial conductivity model is produced by relabeling the voxels of the 3D image of the XCAT model to the corresponding conductivity values based on literature ([30]) at 50 kHz of the heart tissue, blood, lung, bone, cartilage, air, tissue, skin, and background tissue, and then interpolating onto the nodes of the FEM mesh. The conductivity distribution is then improved by incorporating a blood perfusion model (based on [31]), where the lung conductivity is given by the following equation

$$\sigma_i(t) = \sigma_L \left[1 + \Delta\sigma_{LMAX} \cdot P_L \left(t - \frac{d_{PV_i}}{PWV} \right) \right] \quad (5)$$

and σ_L is the nominal lung conductivity, $\Delta\sigma_{LMAX}$ is a factor used to control the maximum increase in conductivity, P_L is the pulmonary arterial distension, d_{PV_i} is the distance from each point in a given lung to its pulmonary valve, and PWV is the pulse wave velocity of the blood through the lung. We choose a nominal conductivity of 0.09 S/m (σ_L), allow for a maximum conductivity increase of 10%, and take the pulse wave velocity to be 1.5 m/s based on [31]. The blood volume entering the pulmonary artery given by the XCAT model is used as a surrogate for P_L.

2.4. Description of Experiments

2.4.1. Simulated Thorax Experiment. The simulated experiment used the model described in Section 2.3 assuming 1) 32 electrodes equally spaced in a horizontal plane centered at the heart height and 2) 11 heart frames of data that cover a portion of the cardiac cycle where the LV volume ranged from 52 mL to 119 mL. The simulated experimental data (test data) included 660 frames where 1 to 6 electrodes were partially occluded (50% to 95% in 5% steps, i.e 10 possibilities) for each of the 11 heart frames. The partially contacting electrodes were $\{1\}$, $\{1, 2\}$, $\{1, 2, 32\}$, $\{1, 2, 31, 32\}$, $\{1, 2, 3, 31, 32\}$, and $\{1, 2, 3, 30, 31, 32\}$. These electrodes were chosen as they appeared most important for producing accurate heart reconstructions and are the closest electrodes to the true anatomical heart region. For each set of partially contacting

electrodes, all electrodes within the set were occluded by the same percent. Single-ended measurements were simulated assuming skip (injection) patterns of 1 through 7, which results in 224 injection patterns on the 32 electrodes. This matrix (32×224) of single-ended voltages (differenced by a reference set of single-ended voltages) was used as input to the DNN while a down-selection to only 4-skip voltage differences are used in the EIT reconstructions (928×1), see Table 1.

Table 1. Measurement Frame Description for 16-electrode Saline Tank and 32-electrode Simulated Thorax Experiments.

Method	Experiment	Skip Patterns	Voltage Type	Frame size
EIT	Simulated Thorax	4	Differential	928×1
EIT	Measured Tank	1-7	Differential	$1,456 \times 1$
DNN	Simulated Thorax	1-7	Single-ended	224×32
DNN	Measured Tank	Exhaustive	Single-ended	112×16

2.4.2. Saline Tank Phantom Experiment Impedance data was recorded from a cylindrical, saline-filled tank with 28 cm diameter, 5 cm depth, 16 electrodes each with widths of 1.2 cm and heights of 5 cm (Fig 1B). The background conductivity was 0.1 S/m, and there were 6 metal inclusions used (considered one at a time) with diameters ranging from 1.5" to 4" in 0.5" steps and centered at (2.5", 0). Impedance data was recorded using a custom designed EIT system [33] at 10 kHz. Measurements for partially contacting electrodes were achieved by lifting the electrodes 60%, 70%, 80%, 90%, and 95% out of the saline. For each percent occlusion considered, electrodes 1, 2, & 16 were all removed the same percent out of the tank. Single-ended measurements are recorded assuming exhaustive skip (injection) patterns, which resulted in 112 injection patterns on the 16 electrode tank. This matrix (16×112) of single-ended voltages (differenced by a reference set of single-ended voltages) was used as input to the DNN while a down-selection to only 1 through 7-skip voltage differences are used in the EIT reconstructions ($1,456 \times 1$), see Table 1.

2.5. Deep Neural Network

Deep neural networks (DNN) are highly expressive models that have proven effective for a variety of data analysis and pattern recognition tasks. Through a series of hierarchical non-linear transformations, neural networks are able to extract salient task-specific features from raw input data. Convolutional neural networks, in particular, are designed to capture spatially local and global patterns in multidimensional inputs, and are thus used in image and video processing tasks. In this work, we implement DNNs featuring convolutional layers to learn salient features from unprocessed impedance measurements which are suitable for predicting the expected cardiac output.

The input data to the DNNs are 2-D matrices of single-ended voltages (Fig. 2A), in the format: (number of electrodes) $\times$ (number of current injection patterns). Calculating correlations across rows (current patterns as variables) and across columns (electrodes as variables) revealed the (generally local) correlations present in the matrix form of the data (Figs 2B & 2C, respectively). Hence, a 2-D convolutional neural network is a practical choice for capturing the spatial interdependencies in the data.

A pre-processing step is required to accommodate the symmetric nature of the measurements. In the experimental setup, since electrodes are arranged in a circle, the first and last electrodes are adjacent to each other. However, those same electrodes are far apart in a simple 2-D input matrix representation. To address this, the first N_W rows of the input matrix are repeated at its end to provide the network with this wraparound information. This pre-processing step was observed to improve network performance.

The architecture of the neural network used was identified using a hyper-parameter optimization toolkit. Using a Tree of Parzen Estimators (TPE) [34], the optimization toolkit determined optimal number of layers as well as corresponding optimal number of hidden units. The hyper-parameter search process involved the training of over 50 different models to find the configuration. Unlike the network architecture, the optimal number of wraparound rows ($N_W = 4$) was identified in a heuristic manual search manner.

The resulting network architecture (Fig. 3) featured 5 layers in all. Layers 1-3 are convolutional layers of size 28, 16, 15, respectively. The 2-D convolutional kernel sizes were (3,5) for the first and (3,3) for the second and third. The corresponding kernel strides were (2,3) for the first 2 layers and (1,3) for the third layer. The output sizes of the convolutional layers are (18,75), (9,25) and (9,9), respectively. All convolutional layer activations were rectified linear units (ReLU), preceded by mini-batch normalization. An average pooling layer downsamples the output of layer 3 into a $4 \times 4 \times 15$ matrix. This is then flattened into a 240×1 vector, and fed to a 7-unit dense layer. The output layer is a single linear regressor node for predicting heart volume. In all, there are 8,600 parameters in the neural network.

The DNN was implemented in Python using the Tensorflow deep learning library, with the Keras wrapper. Training was performed with the Adam optimization algorithm for stochastic gradient descent, with a batch size of 32 for 80 epochs, completing in 10 minutes on a computer with an Nvidia GTX 1080 Ti GPU, a 3.8 GHz Core i5 CPU and 64 GB of RAM.

2.5.1. Simulated Thorax Databases The simulated thorax databases either assumed the bad electrodes were known or unknown. The databases include many samples of simulated non-idealities, where each sampled error is simulated over all 11 heart frames. The non-idealities include percentages of electrodes being occluded and a rotation of the electrode plane from horizontal (horizontal is assumed ideal). The percent occlusions varied from 50% to 95% in 5% steps, and the electrode plane was rotated through the heart center along the left-right axis by randomly selected angles from the set (+/-0.7,

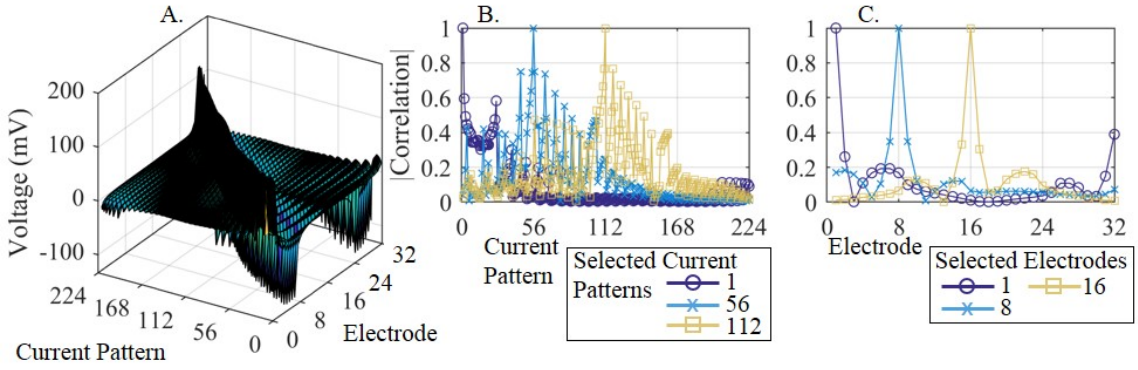

Figure 2. Example matrix of simulated single-ended voltages from the simulated thorax model (A) and corresponding absolute correlations of selected current patterns across electrodes (B) and selected electrodes across current patterns (C), which reveals the 'spatial' correlations in the singled-ended 'images'.

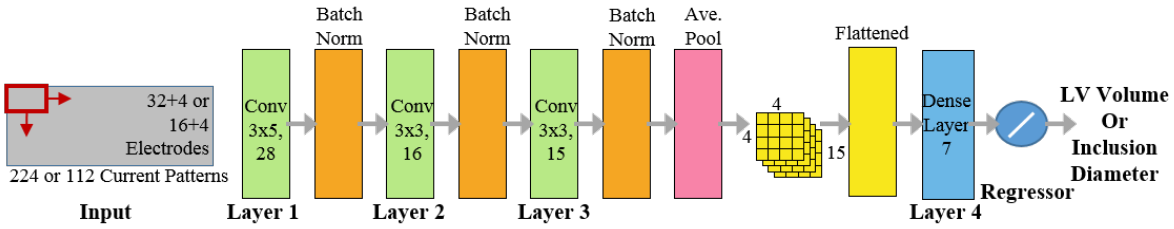

Figure 3. Architecture of the network: 5 layer DNN with 3 convolutional layers, a dense 4th layer, and a final regression layer that predicts the LV volume or inclusion diameter (depending on the experiment) from an input matrix of single-ended voltages (differenced by a reference frame).

+/-0.5, and +/-0.3 degrees). The training database assuming known bad electrodes, DB^{XCAT}_{known}, consisted of 22,011 samples, which had 11 samples with no error (i.e. 11 heart frames with no error) and 2,000 sets of 11 heart frames with randomly sampled non-idealities. Each set of 2,000 samples were constructed by selecting all possible combinations of percent occlusions of electrodes 1, 2, & 32 (1,000) where for each possibility 2 electrode plane rotations were randomly selected. The training database on unknown electrodes, $DB^{XCAT}_{unknown}$, consisted of 77,000 samples, which had 11 samples with no error (i.e. 11 heart frames with no error) and 7,000 sets of 11 heart frames with random sampled errors. For each random sample of errors, 5 electrodes were chosen where it was uniformly chosen between good contact and partial contact and a random electrode plane rotation was chosen. For partially contacting electrodes the percent occluded was randomly selected among the 50% to 95% options. A different mesh was used for each electrode plane rotation and the only training data that used the same mesh as in testing was from the 11 samples with no occluded electrodes, i.e. good data.

2.5.2. Saline Tank Phantom Databases The first database DB^{tank}_{known} assumed that it was known *a priori* which electrodes had some partial contact. For this database, frames of data corresponded to the exhaustive combinations of electrodes 1, 2, and 16 being partially occluded; specifically 17 possible values of occlusions ranging from 10% to 95% in 5% increments. The total size of the database was 40,831, where there are 5,832 frames for each inclusion (including the homogeneous case) and all good data (7 frames). The second database $DB^{tank}_{unknown}$ assumes no knowledge of which electrodes have partial contact. Thus random sets of electrodes (1-5 bad electrodes per sample) were picked to have partial contact of random amounts (5% to 95% in 5% steps). The total database consisted of 84,000 samples, in which there were 6 conductivity distributions and 4,000 random samples with 1 bad electrode, 3,000 random samples for 2 & 3 bad electrodes each, and 2,000 random samples for 4 & 5 bad electrodes each. The test set used to evaluate the DNN is the measured tank data, described in Section 2.4.2.

2.6. Additional Parameters

Optimal Tikhonov parameters were found to be 10 in the simulated thorax experiment and 1 and 10 for the tank experiment when using all electrodes and when electrodes 1, 2, and 16 were removed, respectively. The mesh used for simulations and the Jacobian calculation in the saline tank experiment was ∼30k nodes and ∼150k elements and was constructed using Netgen [32].

3. Results

3.1. 4D XCAT Simulated Thorax

The predicted LV volumes, assuming 70%, 80%, 90%, and 95% occlusions of electrodes 1, 2, and 32, are shown for all four methods (Fig. 4A-D), i.e. EIT without compensation, EIT with bad electrodes removed, the DNN trained on DB^{XCAT}_{known}, and the DNN trained on $DB^{XCAT}_{unknown}$. The EIT approach with no electrode compensation has the largest errors, and does not track well with the LV volume. The EIT with bad electrodes removed performs better, but not as accurately as the DNN's (Fig 4E). The DNN trained on unknown bad electrodes slightly outperformed that of the DNN trained on known bad electrodes (mean absolute error of 2.8% compared to 2.5%). Additionally, the two EIT approaches and DNN trained on the unknown bad electrode set were evaluated assuming all sets of bad electrodes (Fig. 5). The EIT approaches were also evaluated when there were no bad electrodes. One can observe that the approach of removing known bad electrodes using EIT results in consistent errors for up to 3 electrodes removed and slightly increases errors for 4-6 electrodes removed. The DNN once again outperformed the EIT approaches, but this time only when less than 5 electrodes were partially occluded. For partial occlusions of 5 or 6 electrodes (only up to 5 were trained on) the errors significantly degrade. Illustrations of the loss curves on the training and testing sets over 80 epochs reveal good convergence while indicating the network is not

overfitting the training database (Fig. 6A). Overall, the DNN results, which do not rely on knowledge of bad electrodes, appear very promising as similar performance is achieved using the EIT approach, which requires knowledge of bad electrodes.

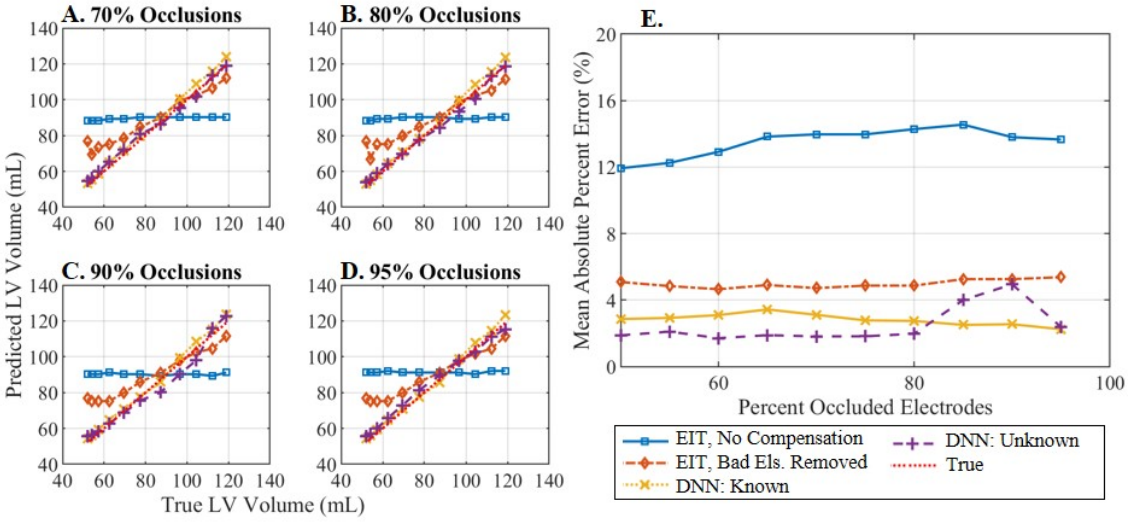

Figure 4. Predicted LV volume for each of the methods considered (EIT with no compensation (A), EIT with bad electrodes removed (B), and DNNs trained on DB^{XCAT}_{known} (C) and on $DB^{XCAT}_{unknown}$ (D)) on the simulated thorax example where electrodes 1, 2, & 32 were 70%, 80%, 90%, and 95% occluded. Mean errors of the predicted LV volume from each method assuming electrodes 1, 2, & 32 were partially occluded (E).

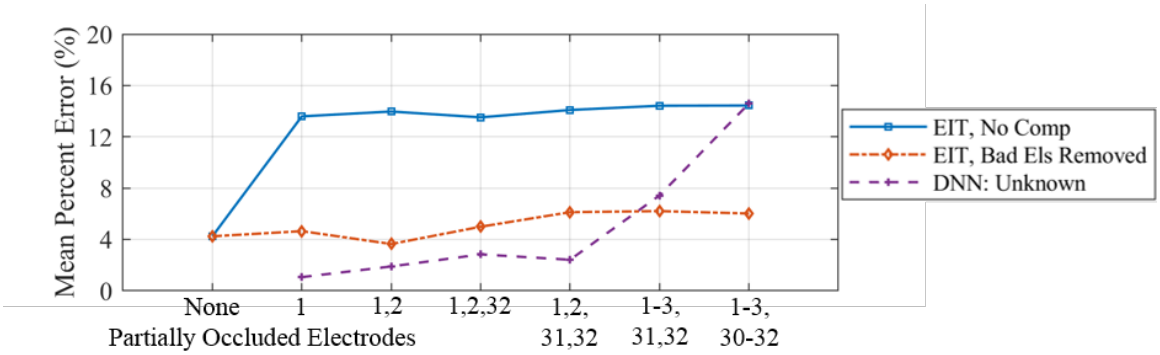

Figure 5. Overall mean percent errors across each set of partially occluded electrodes (0 to 6 bad electrodes) using EIT with no compensation, EIT with bad electrodes removed, and DNN trained assuming bad electrodes were not known for the simulated thorax example.

3.2. Saline Tank Phantom

EIT reconstructions for the no compensation approach (Fig 7) reveal that the reconstructions are qualitatively very sensitive to the partially contacting electrodes

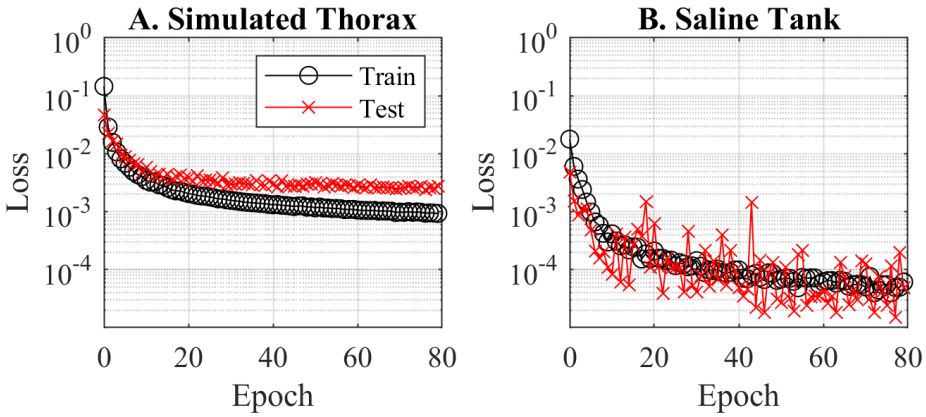

Figure 6. Logistic loss curves of the training and testing databases (assuming unknown bad electrodes) for A. the simulated thorax and B. saline tank.

with artifacts worsening with increasing percent occlusion. In contrast, when the bad electrodes are removed, the EIT reconstructions qualitatively appear quite robust to partially contacting electrodes (last row of Fig 7 which shows 95% occlusion). The DNN algorithms do not produce images, so there are no qualitative images to present.

The predicted inclusion diameters, assuming 70%, 80%, 90%, and 95% occlusions of electrodes 1, 2, & 16, are shown for all four methods (Fig. 8A-D). EIT with no compensation performs poorly, while the other approaches appear quite similar and are all close to the diagonal. To more clearly show the difference in accuracy, the mean absolute percent error across all experiments is displayed for each approach and percent occlusion (Fig. 8E). The three approaches (EIT bad electrodes removed, and DNN using either DB) have very similar accuracies. Averaging across all percent occlusions the errors are 24.3%, 3.7%, 7.0%, and 4.0% for the EIT with no compensation, EIT with bad electrodes removed, DNN using known and DNN using unknown bad electrodes, respectively. While EIT with bad electrodes removed is a commonly used approach, the similar accuracy to the DNN approach on measured data strongly validates the hypothesis that DNN algorithms can practically work on measured data when trained on simulated data. The DNN algorithms trained using $DB^{tank}_{unknown}$ outperformed the DB^{tank}_{known}-trained results, which is surprising because the DB^{tank}_{known} implicitly had more information. A similar check on the loss curves for this experiment shows good convergence while indicating the network is not overfitting the training database (Fig. 6B).

3.3. Computational Cost

We measured the computational cost in terms of memory storage required and the number of FLOPs, which we use as a surrogate measure for speed. The results are summarized in Table 2. The difference in the number of FLOPs between the EIT approaches is due to the reduced number of measurements associated with removal of

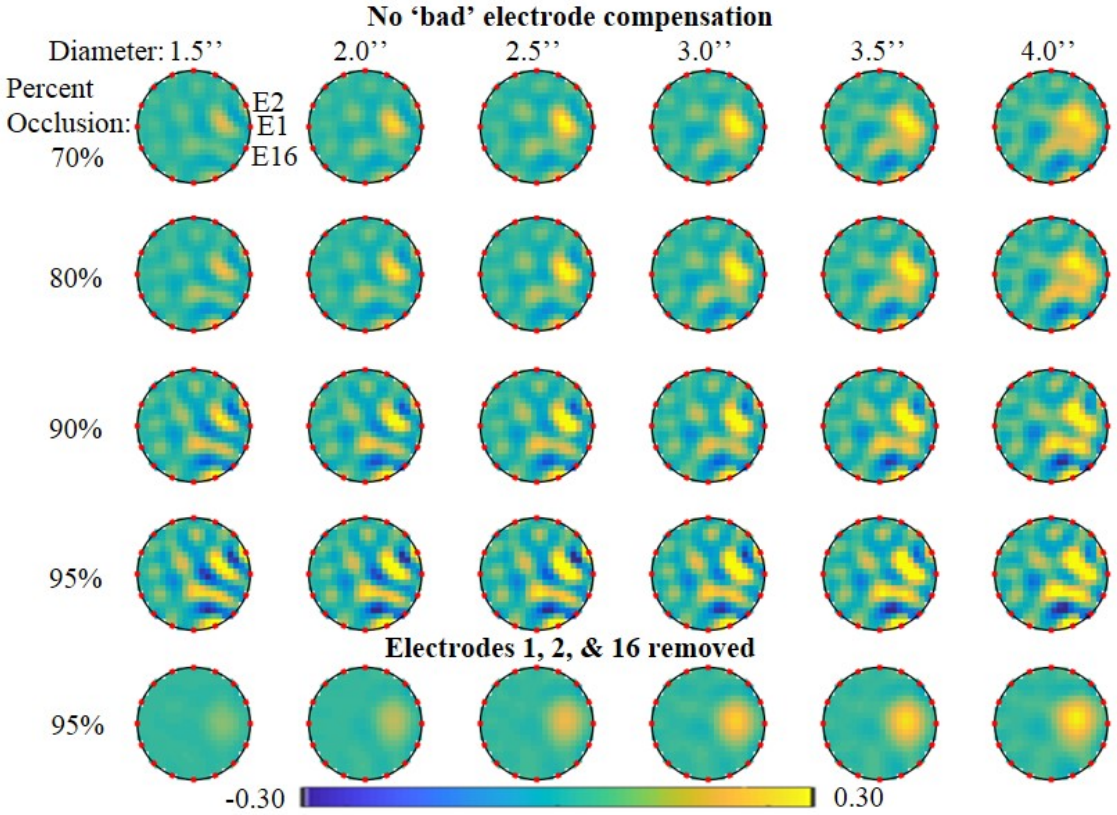

Figure 7. EIT reconstructions for measured difference data with electrodes 1, 2, & 16 occluded 70%, 80%, 90% and 95% in the first 4 rows assuming no bad electrode compensation. The final row depicts EIT reconstructions with 95% occlusions with bad electrodes removed. Qualitatively, 95% occlusions with bad electrodes removed look nearly the same reconstructions using all good data (not shown).

bad electrode data. The required memory is the same for the EIT approaches because both, in general, require storage of the complete Jacobian, which accounts for the vast majority of memory. In addition, we see that DNNs have significantly less FLOPs and memory required to evaluate the networks. Overall, on a current desktop computer these are all reasonable and fast calculations, but for the envisioned use of this technology in a portable, low-power system the lower computational requirements of the DNNs may make it a more attractive method.

Table 2. Computational cost of the different methods.

Method	FLOPs (×1000)	Memory Required (MB)
EIT No Comp	920	3.68
EIT Bad Els Removed	360	3.68
DNN (XCAT)	18	0.34
DNN (tank)	15	0.29

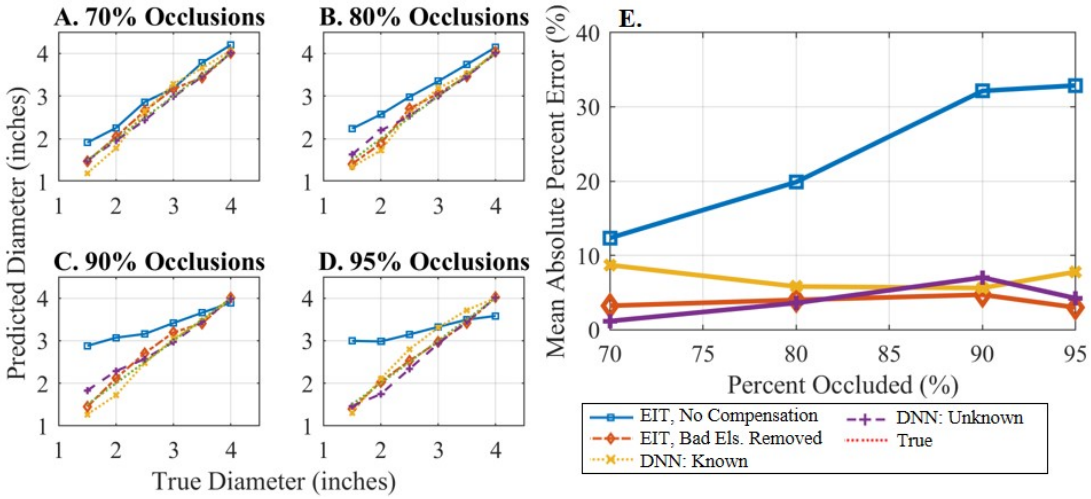

Figure 8. Reconstructed diameters from the tank experiment using A. EIT with no compensation, B. EIT with bad electrodes removed, and DNNs trained on C. DB^{tank}_{known} and D. $DB^{tank}_{unknown}$ with electrodes 1, 2, & 16 occluded 70%, 80%, 90%, or 95%. E. Mean absolute percent error of the four methods over the 6 metal inclusions with 3 repeated measurements per inclusion.

4. Discussion

This study highlights a proof-of-concept demonstration of how a DNN can be used to predict cardiac metrics through an imageless approach in a simulated thorax and a measured saline tank experiment, and provides details of a 4D thorax model that can be used to produce richly detailed simulations. This method is robust to up to four bad electrodes and should be of interest to others in the EIT community for related applications, as current EIT approaches can only handle up to two poorly contacting electrodes [19]. For instance, quantitative outcomes in lung-EIT applications could be considered. Although these results are promising, the thorax experiment is only simulated and does not necessary imply this exact approach will work as well with patient data.

Approaches that may be needed to expand this approach to patient data are 1) further development of the perfusion model of the thorax simulation, 2) incorporating patient-specific information into the training of the DNN databases, and 3) incorporating more information into the DNN for LV volume prediction. Patient-specific information could include height and weight (or chest dimensions) and could potentially include heart size and LV volume recorded during controlled data collection (where at-home LV prediction would be the purpose of the device). Additionally, as surface or near surface conductivities strongly effect the overall measurements, a small database of simulated voltages from a sampling of skin and subcutaneous fat thicknesses can be used to select the best skin and fat thicknesses for the given patient. Lastly in terms of expanding the information provided to the DNN, a promising approach could be to give the DNN not the difference between two frames of data but a time-window of impedance data (e.g.

30 seconds). The DNN can then automatically perform differencing of the data while being robust to bad electrodes - *thus reducing the restrictions on data filtering that is commonly needed in EIT applications.*

5. Conclusion

A new imageless electrical-impedance-tomography trained deep neural network algorithm is described for portable cardiac output monitoring. EIT and DNN approaches are evaluated on simulated and measured experiments. The DNN algorithms perform comparably with the standard EIT approach to handling bad electrodes (removing them), but with the very strong advantage (DNN) of not needing to know which electrodes are bad. This is a potential, significant advantage of the DNN algorithm. Analysis of the computational cost shows that the DNN may be more attractive as a method for the envisioned low-power, portable system because of its significantly reduced computational requirements. Overall, this work represents an important step in validation of the method using measured data, and model development, which is needed to apply this method to real clinical data.

Acknowledgment

This work was supported in part by the U.S. National Science Foundation, under Grant No. 1418497, the National Institutes of Health under Grant 5R01CA143020, and US DoD CDMRP Grant W81XWH-15-1-0571.

References

[1] M.J. Hal, S. Levant, and C.J. DeFrances, "Hospitalization for congestive heart failure: United States, 2000-2010". NCHS Data Brief 18 Online: http://www.ncbi.nlm.nih.gov/pubmed/23102190, 2012.

[2] J. Butler, D. Chirovsky, H. Phatak, A. McNeil, R. and Cody, "Renal function, health outcomes, and resource utilization in acute heart failure: A systematic review," Circ. Hear. Fail., vol. 3, 72645, 2010.

[3] R. Purcell, S. McInnes, and E.J. Halcomb, "Telemonitoring can assist in managing cardiovascular disease in primary care: a systematic review of systematic reviews," BMC Fam. Pract., vol. 15, 43, 2014.

[4] Hasan A and Paul V, "Telemonitoring in chronic heart failure," Eur. Heart J., vol. 32, pp. 145764, 2011.

[5] Chaudhry S, Mattera J, Curtis J, JA S and Herrin J, "Telemonitoring in patients with heart failure," N. Engl. J. Med., vol. 363, pp. 23019, 2010.

[6] J.A. Alhashemi, M. Cecconi, and C.K. Hofer, "Cardiac output monitoring: an integrative perspective," Crit. Care, vol 15, 214, 2011.

[7] J.M. Gillard, "Understanding cardiac biomarker," Emerg. Med., vol. 40, 124, 2008.

[8] P.E. Marik, "Noninvasive cardiac output monitors: A state-of the-art review," J. Cardiothorac. Vasc. Anesth., vol. 27, 12134, 2013. Online: http://dx.doi.org/10.1053/j.jvca.2012.03.022

[9] A. Fagerberg, O. Stenqvist, and A. Aneman, "Electrical impedance tomography applied to assess matching of pulmonary ventilation and perfusion in a porcine experimental model," Crit. Care, vol. 13, R34, 2009

[10] R. Pikkemaat, S. Lundin, O. Stenqvist, R.-D.Hilgers, and S. Leonhardt, "Recent advances in and limitations of cardiac output monitoring by means of electrical impedance tomography," Anesth. Analg., vol. 119, 76832014. Online: http://www.ncbi.nlm.nih.gov/pubmed/24810260

[11] A. Vonk-noordegraaf, J.T. Marcus, J.G.F. Bronzwaer, P.E. Postmus, T.J.C. Faes, and P. de Vries, "Determination of stroke volume by means of electrical impedance tomography Determination of stroke volume by means of electrical impedance tomography," Physiological measurement, vol. 21, 285-293, 2000.

[12] S.H. Arshad, Jordan S. Kunzika, Ethan K. Murphy, Kofi Odame, Ryan J. Halter, "Towards a Smart Phone-Based Cardiac Monitoring Device using Electrical Impedance Tomography," IEEE BioCAS conference proceedings, Oct. 22-24, 2015.

[13] M. Takhti, Y.C. Teng, K. Odame, "A high frequency read-out channel for bio-impedance measurement," Proc. IEEE International Symp. on Circuits and Systems, 1514-1517, July 2016.

[14] L.M. Heikkinen,T. Vilhunen, R.M. West, and M. Vauhkonen, "Simultaneous reconstruction of electrode contact impedances and internal electrical properties: II. Laboratory experiments," Measurement Science and Technology, vol. 13, no. 12, 1855-1861.

[15] G. Boverman, D. Isaacson, G.J. Saulnier, and J.C. Newell, "Methods for Compensating for Variable Electrode Contact in EIT," IEEE Trans on Biomed. Eng., vol. 56, no. 12, 2762-2772, 2009.

[16] E. Demidenko, A. Borsic, A. Hartov, Y. Wan, R. Halter, "Statistical estimation of EIT electrode contact impedance using magic Toeplitz matrix," IEEE transactions on bio-medical engineering, vol. 58, no. 8, 2194-2201, 2011.

[17] Y. Asfaw and A. Adle, "Automatic detection of detached and erroneous electrodes in electrical impedance tomography," Physiol. Meas., vol. 26, S175-S183, 2005.

[18] M.H. Jeon, A.K. Khambampati, B.S. Kim, S.I. Kang, and K.Y. Kim, "Image reconstruction in EIT with unreliable electrode data using random sample consensus method," Measurement Science and Technology, vol. 28, 2017.

[19] A.E. Hartinger, R. Guardo, A. Adler, and H. Gagnon, "Real-Time Management of Faulty Electrodes in Electrical Impedance Tomography," IEEE Trans on Biomed. Eng., vol. 56, no. 2, 369-377, 2009.

[20] Y. Mamatjan, P. Gaggero, B. Muller, B. Grychtol, and A. Adler, "Compensating Electrode Errors Due To Electrode Detachment in Electrical," Canadian Medical and Biological Engineering Society (CMBEC36), 2013.

[21] G. Zhang, M. Dai, L. Yang, W. Li, H. Li, C. Xu, X. Shi, X. Dong, and F. Fu, "Fast detection and data compensation for electrodes disconnection in long-term monitoring of dynamic brain electrical impedance tomography," BioMedical Engineering Online, vol. 16, no. 1, 1-23, 2017.

[22] E. Somersalo, M. Cheney, and D. Isaacson, "Existence and uniqueness for electrode models for electric current computed tomography," SIAM Journal on Applied Mathematics, vol. 52, no. 4, 1023–1040, 1992.

[23] A. Borsic, A. Hartov, K. D. Paulsen, and P. Manwaring, "3D electric impedance tomography reconstruction on multi-core computing platforms, in Proc. Annu. Int. Conf. IEEE Eng. Med. Biol. Soc., Dec. 2008, pp. 11751177.

[24] W. P. Segars, G. Sturgeon, S. Mendonca, J. Grimes, and B. M. W. Tsui, 4D XCAT phantom for multimodality imaging research, Med. Phys., vol. 37, no. 9, p. 4902, 2010.

[25] E. K. Murphy and J. L. Mueller, "Effect of domain shape modeling and measurement errors on the 2-D D-bar method for EIT," IEEE Trans. Med. Imaging, vol. 28, no. 10, pp. 15761584, 2009.

[26] A. Boyle, A. Adler, and W. Lionheart, "Shape deformation in two-dimensional electrical impedance tomography," IEEE Trans. Med. Imaging, vol. 31, no. 12, pp. 218593, 2012.

[27] P.-O. Persson and G. Strang, "A Simple Mesh Generator in MATLAB," SIAM Rev., vol. 46, no. 2, pp. 329345, 2004.

[28] C. Geuzaine and J.F. Remacle, "Gmsh: A 3-D finite element mesh generator with built-in pre- and post-processing facilities," Int. J. Numer. Methods Eng., vol. 79, no. 11, pp. 13091331, 2009.

[29] W.R.B. Lionheart, "EIT reconstruction algorithms: pitfalls, challenges and recent developments," Phys. Meas., vol. 25, no. 1, pp. 125-142, 2004.

[30] D. Andreuccetti, R. Fossi, and C. Petrucc, "Dielectric Properties of Body Tissues," Website: http://niremf.ifac.cnr.it/tissprop/htmlclie/htmlclie.php, accessed 20 November 2017.

[31] F. Braun, et al., "Aortic blood pressure measured via EIT: investigation of different measurement settings, Physiol. Meas., vol. 36, no. 6, pp. 114759, 2015.

[32] J. Schöberl, "NETGEN An advancing front 2D/3D-mesh generator based on abstract rules," Comput Visual Sci, vol. 1, 41-52, 1997.

[33] S. Kahn, P. Manwaring, A. Borsic, R.J. Hlater, "FPGA-based voltage and current dual drive system for high frame rate electrical impedance tomography," Medical Imaging, IEEE Trans., vol. 34, no. 4, pp. 888-901, 2015.

[34] Bergstra, J.S., Bardenet, R., Bengio, Y. and Kgl, B.. "Algorithms for hyper-parameter optimization." In Advances in neural information processing systems, pp. 2546-2554, 2011.

Current Conveyor Based Wide-band Current Driver for Electrical Impedance Tomography

A J Rao, E K Murphy, M Shahghasemi, and K M Odame

Thayer School of engineering, Dartmouth College, Hanover, NH, USA

E-mail: arun.j.rao.th@dartmouth.edu

Abstract. In this paper a wide-band integrated current driver for electrical impedance tomography (EIT) is presented. The application is primarily for prostate and breast cancer detection which require the tissue to be interrogated at frequencies up to 10 MHz while achieving low harmonic distortion and high accuracy. The current driver is based on current conveyor architecture and can deliver 1.2 mA of peak to peak ac current between frequencies of 100 Hz - 10 MHz. It is fabricated in CMOS 0.18-μm technology with a power supply of 3.3 V, and occupies a core area of 0.26 mm^2. The measured harmonic distortion for a peak current of 1.2 mA is $< 0.1\%$ for frequencies less than 100 kHz, and increases to 0.68% at 10 MHz. The measured output impedance of the current driver is 101 kΩ at 1 MHz and 19.5 kΩ at 10 MHz. The current driver maintains an accuracy $> 99\%$ with negligible phase error when delivering ac currents to an R-C load. The circuit is suitable for high frequency active electrode applications.

Keywords: bio-impedance, current conveyor, integrated current driver, electrical impedance tomography, wide-band, CMOS circuits

1. Introduction

Bio-impedance varies widely between cancerous and benign tissues and exhibits frequency dependent characteristics which have been used for differentiating various kinds of cancer (Saulnier et al., 2001). Electrical Impedance Tomography (EIT) is an imaging modality that incorporates the bio-impedances of various parts of the measured tissue to provide a spatial mapping of the organ being probed. By injecting a sinusoidal current into the tissue at the source electrode and measuring the voltages induced at the remaining electrodes, impedance of tissue is obtained, as shown in figure 1. One of the key advantages of an EIT system is its relatively smaller size and inexpensive cost compared to other imaging techniques such as Magnetic Resonance Imaging (MRI) or Computerized Tomography (CT). Importantly, EIT is also non-ionizing.

A major challenge of EIT is that it requires an accurate, high output impedance current driver to deliver a pure sinusoidal signal to the tissue being interrogated. The EIT current driver has traditionally been implemented as a Howland current source with discrete components (Tucker et al., 2013). This implementation unfortunately

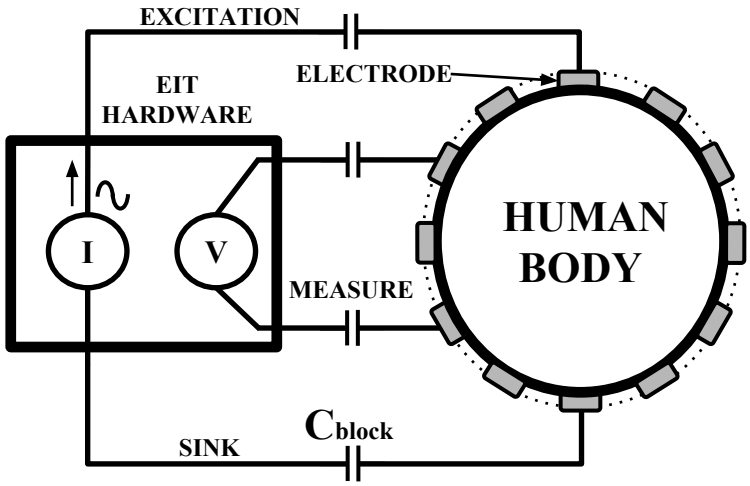

Figure 1. Block diagram of a typical EIT system. AC current excitation is performed using a pair of electrodes and the voltages induced on the remaining electrodes are measured.

introduces a significant amount of parasitic capacitance, which limits the bandwidth of the EIT system. To achieve higher frequencies of operation, the current driver must be implemented in an integrated circuit (IC), as part of an active electrode system, whereby the electronics are physically close to the electrodes and parasitic capacitance is minimized. Several promising IC current drivers have recently been proposed (Yan et al., 2011; Constantinou et al., 2014; Constantinou et al., 2015; Hong et al., 2015; Kim et al., 2017; Wu et al., 2018). Unfortunately, none of the solutions reported in the literature have measured operation beyond the 1 MHz range, where electrical impedance interrogation of intracellular physiology could provide increased contrast between benign and cancerous tissue (Jossinet, 1998; Halter et al., 2008). Also, none of the previous implementations are designed to drive a DC blocking capacitor, which is necessary for patient safety in EIT measurements (Lionheart et al., 2001; McEwan et al., 2007).

In this paper, a wide-band, current conveyor based, integrated CMOS current driver is introduced. Compensation for high speed operation at the transconductance stage is achieved using the indirect compensation technique (Saxena, 2007) which enables operation up to 10 MHz. Also, current-mode circuits (Wilson, 1990) at the output stage further aid in the wide-band operation of the designed current driver. Finally, a DC servo-loop circuit at the output branch maintains reliable operation of the current driver in the presence of a DC blocking capacitor at the current injection electrode.

2. Overview

Our proposed current driver for this design is based on the CCII current conveyor (Sedra and Smith, 1970) shown in figure 2. The input to the current driver is the voltage, V_Y. This is buffered to V_X, which generates a current $I_X = \frac{V_X}{R_X}$ through the load resistor

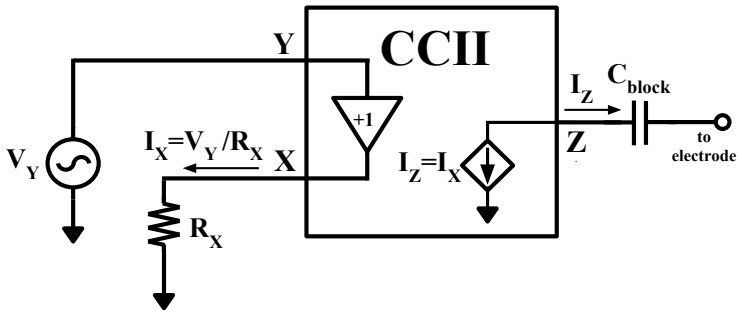

Figure 2. Block diagram of the current conveyor architecture (Sedra and Smith, 1970). Current is generated at terminal X using an on-chip resistor such that $I_X = \frac{V_X}{R_X}$, and V_X follows the voltage at terminal Y. Current I_X is delivered to terminal Z with a current gain of unity.

R_X. The current I_X is mirrored to the output of the current-controlled current source, and $I_Z = I_X$ flows through a DC-blocking capacitor, C_{block}, to an electrode and into the tissue. Our current driver architecture (figure 3) is based on the work presented in (Jivet and Dragoi, 2008). We modified the original architecture to make it suitable for high frequency EIT applications. In particular, we designed the 2-stage operational amplifier (op-amp) of figure 3 with indirect compensation around a class AB control circuit, to enable current interrogation frequencies up to 10 MHz. Also, we implemented a DC-biasing servo loop at the output of the current driver; this ensures proper operation of the current driver in the presence of a 1 μF DC-blocking capacitor that is necessary for patient safety.

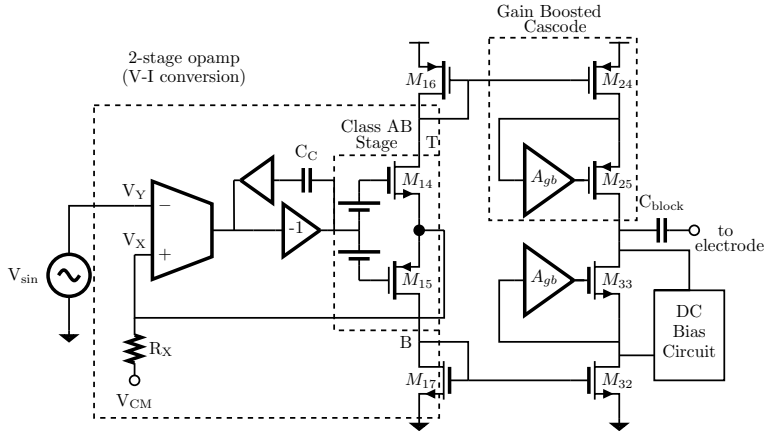

Figure 3. The architecture of the current driver. (a) The voltage to current conversion is performed using a 2-stage op-amp with indirect feedback compensation. (b) Class AB output stage at the output of the op-amp is necessary for generating the sinusoidal current at terminal X using a resistor R_X. (c) Current is mirrored to the high output impedance terminal Z with a gain enhanced current mirror forming the output stage.

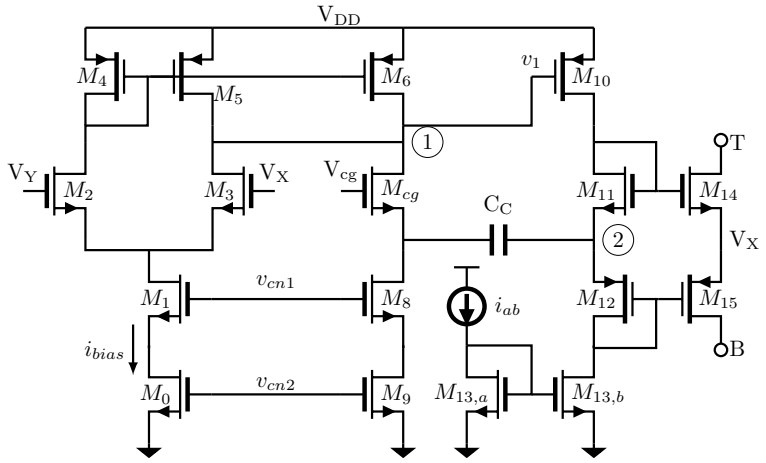

Figure 4. Two stage op-amp with indirect compensation followed by a class AB output stage. (a) The current from the output node 2 is indirectly fed to node 1 using the common gate transistor M_{cg}. This forms the indirect feedback compensation technique.(b) Transistors $M_{11}, M_{12}, M_{14}, M_{15}$ form the class AB output stage to source and sink currents into node X. Gate voltages, v_{cn1} and v_{cn2} are set by gate biasing circuits (not shown).

3. Circuit Design and Analysis

Details of the circuit implementation are presented in this section.

3.1. V-I conversion

Figure 4 shows the circuit diagram of the 2-stage op-amp with indirect compensation technique used for the voltage to current conversion in the current driver. A RHP pole zero appears in the transfer function of a conventional 2-stage op-amp compensated using a compensation capacitor C_c. This problem has been well-studied (Baker, 2010) and various compensation techniques exist to cancel the RHP zero or move it into the LHP to improve stability. However, the nulling resistor technique for compensation is process dependent and the use of a transistor in triode region of operation can cause issues with large signal behavior (Baker, 2010). Also, the value of compensation capacitor selected limits the speed of the circuit when high frequency of operation is desired.

In the indirect compensation technique, the compensation capacitor is not directly connected to the op-amp output. Instead, pole-splitting is achieved indirectly using a common gate transistor, M_{cg}, feeding the current from the output back to the first stage. Input transistors M_2, M_3, with current mirror loads M_4, M_5 and cascoded tail transistors M_0, M_1 form the input stage of the 2 stage op-amp. The gain of the input stage is given by $A_{v1} = g_{m2}(r_{o3}||r_{o5})$, where $g_{m2} = g_{m3} = G_{M1}$ are the transconductances of the input differential pair and r_{o3}, r_{o5} are the output impedances of transistors M_3, M_5 respectively. The branch comprising of transistors M_6, M_8, M_9, and M_{cg} form the indirect compensation branch in the circuit along with the compensation capacitor C_c. The gate of the common gate transistor M_{cg} is tied to the common mode voltage of the

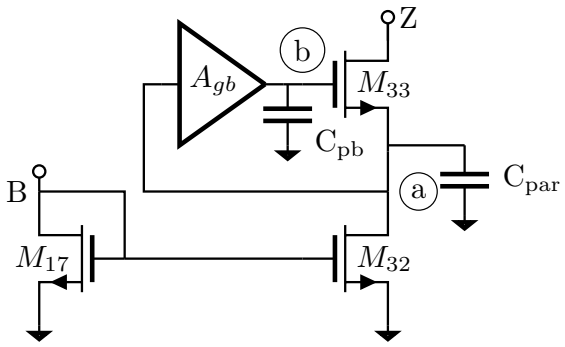

Figure 5. The gain boosted cascode structure with the amplifier A_{gb} providing an overall output impedance of $Ag_{m2}r_{o2}r_{o1}$ at node Z.

circuit. The currents in the input differential pair transistors and the indirect feedback branch are kept equal to achieve $G_{m1} = g_{m,cg}$. The output branch which provides the second stage gain is provided by transistors M_{10} and M_{13} which is the current source load. The gain is given by, $A_{v2} = g_{m10}(r_{o10}||r_{o13})$, where g_{m10} is the transconductance of transistor M_{10} and r_{o10}, r_{o13} are the output impedances of transistors M_{10}, M_{13} respectively. The bias voltages v_{cn1} and v_{cn2} are provided using a wide swing cascode current mirror (Carusone et al., 2012) (not shown). Class AB output buffer stage is formed by transistors M_{11}, M_{12}, M_{14}, and M_{15}. When voltage, v_1, at the gate of transistor M_{10} increases, M_{15} turns on and M_{14} turns off, as the gates of M_{11} and M_{12} move towards GND. Similarly, M_{14} sources all the current when v_1 decreases, which implies a class AB operation. The current source i_{ab} provides the necessary DC current bias for the class AB output branch.

Compared to conventional frequency compensation techniques, the indirect compensation technique uses smaller capacitors (Saxena, 2007). The reduced footprint allows multiple current drivers to be integrated onto a single chip; this avoids the parasitic capacitance that would be experienced by a single, multiplexed current source (Saulnier et al., 2001).

3.2. Gain Boosted Cascode Output Stage

The high output impedance necessary for the current driver is achieved by using the structure shown in figure 5. The gain boosting amplifier in figure 5 should have high unity gain frequency and exhibit single pole behavior to ensure stability. To achieve this we implement the amplifier as a common source amplifier with a current source load (transistors $M_{26} - M_{31}$ of figure 6). Gain boosting is similarly implemented for the PMOS half of the output branch, using transistors $M_{18} - M_{23}$.The low frequency small signal gain of the PMOS and NMOS gain boosting amplifiers is given by the following equations (Zeki and Kuntman, 1997) :

$$A_{gb,P} = g_{m21}(r_{o21}//r_{o23}) \tag{1}$$

$$A_{gb,N} = g_{m29}(r_{o29}//r_{o31}) \tag{2}$$

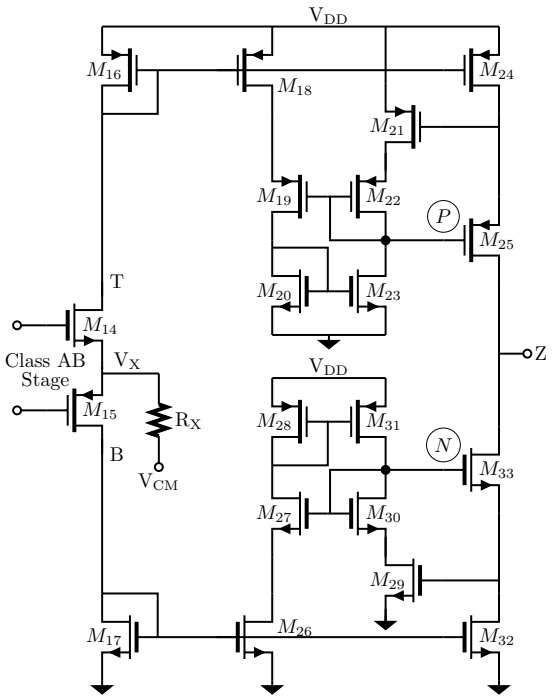

Figure 6. Mirroring of current generated at node X to output node Z using a gain boosted cascode structure. The auxiliary amplifiers for the gain boosted cascode structure have a single pole nature to enable high frequency operation.

where g_{m21}, g_{m29} are the transconductances of transistors M_{21}, M_{29} respectively and r_{o21}, r_{o23}, r_{o29}, r_{o31} are the output impedances of transistors M_{21}, M_{23}, M_{29}, M_{31} respectively. From equations 1, and 2, the overall output impedance at node Z is given as,

$$Z_{out} = (g_{m25}r_{o25}r_{o24}g_{m21}(r_{o21}//r_{o23}))\,//\,(g_{m33}r_{o33}r_{o32}g_{m29}(r_{o29}//r_{o31})) \quad (3)$$

3.3. Current driver output DC biasing

In EIT applications, a DC blocking capacitor at the output of the current driver ensures that no DC current flows into the human tissue (Lionheart et al., 2001). This results in an equivalent structure at the output stage of the current driver as shown in figure 7. Mismatch in the DC values of i_{pmos} and i_{nmos} will cause the output node Z to rail to either VDD or GND. To avoid this, and to maintain a suitable DC bias voltage at node Z, we use the servo-loop circuit shown in figure 8. Here the output branch of the current driver is shown where an operational transconductance amplifier (OTA) sets the output voltage to V_{CM}, which is typically at 1.65 V. The OTA is implemented as a current mirror OTA with input transistors sized to minimize the capacitive loading at node Z. The high output impedance of the OTA along with the capacitor C_{EXT}, external to the ASIC, forms a low pass circuit. In the designed circuit M_{FB} is 1/30 times the width

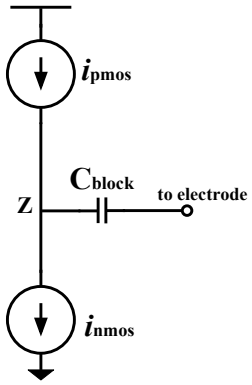

Figure 7. With a DC blocking capacitor C_{block}, the voltage at node Z can rail to either V_{DD} or GND and cause unreliable operation.

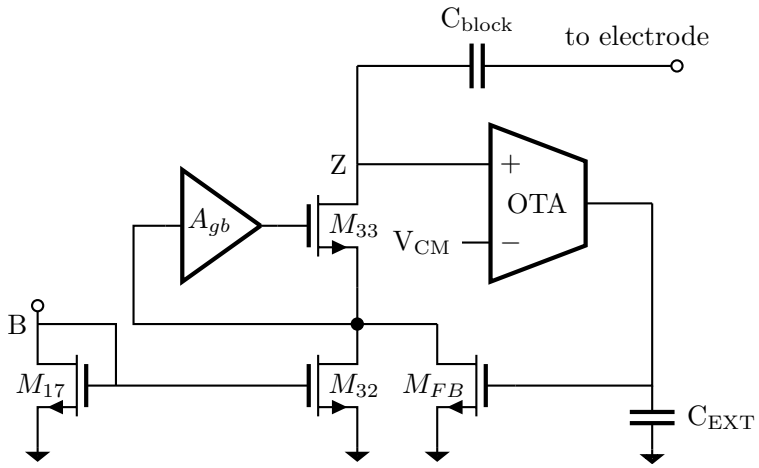

Figure 8. Structure designed to keep the current driver in the proper operating regime. The OTA at the output stage sets the output voltage to the common mode reference voltage V_{CM}, which ensures that all the transistors in the output branch of the current source structure are in saturation thus enabling reliable operation.

of transistor M_{32}, while the length remains the same. Its loading effect at the drain of transistor M_{32} is negligible. The designed servo-loop circuit sets the output branch at a reliable operating voltage such that the cascode transistors in the output branch have sufficient headroom for reliable operation.

4. Measured Results

The current driver was fabricated in XFAB 0.18-μm XH018 CMOS process with supply voltage of 3.3 V. Design, layout and simulation was performed using Virtuoso Cadence. The resistor R_X of figure 3 was implemented as a 500 Ω resistor, integrated on the ASIC. Two additional current driver test structures were also designed and included in the chip for complete measurement. The current driver core area with test structures is approximately 0.26 mm^2 as shown in figure 9.

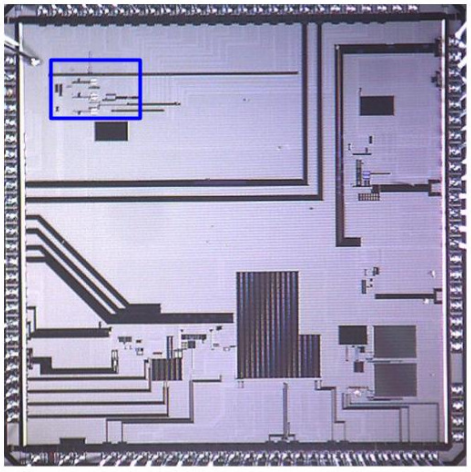

Figure 9. Chip micro photograph. The current driver with test structures are indicated by the blue rectangle.

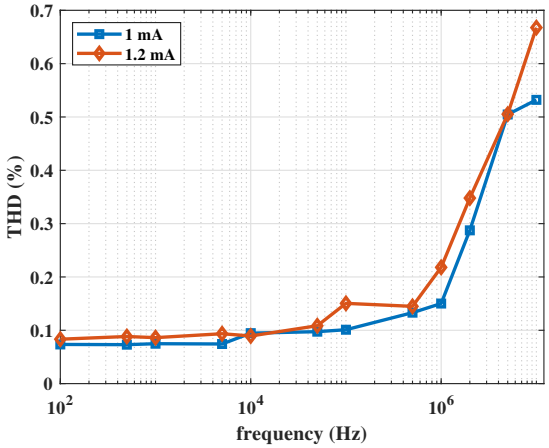

Figure 10. Measured THD vs frequency for current levels 1 mA and 1.2 mA. The worst harmonic distortion measured for the current driver is approximately 0.7%.

4.1. Harmonic Distortion

The input signals to the current driver was generated using a Kiethley Instruments 3300 waveform generator capable of generating sinusoidal signals greater than 10 MHz with negligible distortion contributing to the measurements. A 600 mV peak to peak voltage at the input terminal Y generates the maximum current of 1.2 mA at terminal Z. The output voltage at the load was monitored using a Rigol 1104-Z oscilloscope. Figure 10 shows the measured THD values against frequencies. Current values of 1 mA, and 1.2 mA are chosen to show the performance of the current driver with a 500 Ω load. The current driver achieves a THD of less than 0.7% harmonic distortion at 10 MHz while delivering a current of 1.2 mA to the load.

4.2. Noise

A Stanford Research Systems SRS 785 spectrum analyzer was used for noise measurements of the current driver. Due to limitations of the equipment, noise was measured up to 100 kHz. Figure 11 shows the comparison of measured noise with respect to Cadence simulations.The total integrated noise at the output was approximately 658 μV determined by simulation.

4.3. Output Impedance

The measurement of the output impedance of the current driver was performed as described in (Cook et al., 1994). The test configuration uses a Linear Technology LT1806 wide bandwidth precision op-amp as a negative feedback amplifier. To obtain accurate measurements, we used calibration and feedback resistors with tolerance of 0.1%. The associated parasitics of the board were measured using a Instek 821 precision LCR meter. The measured board parasitics, along with the output pad capacitance of the chip (terminal Z), were incorporated into the calculation of the output impedance. An average of 2500 points for a single frequency point measurement was used to obtain reliable measurement data. Figure 12 shows the output impedance vs frequency for the current driver. The output impedance is 101 kΩ at 1 MHz, and 19.5 kΩ at 10 MHz.

4.4. Cole-Cole Plots and Accuracy

The suitability of the designed current driver for complex impedance measurements up to 10 MHz was verified with the setup shown in figure 13. An R-C circuit combination was used to model the complex tissue impedance of the breast (Halter et al., 2008). A peak-to-peak input voltage of 500 mV was fed from the signal generator such that

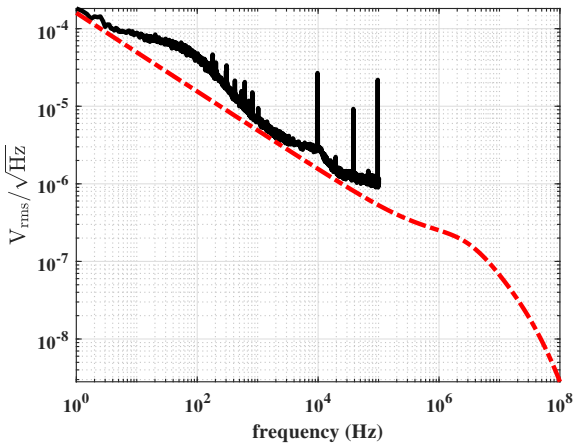

Figure 11. Plot showing the simulated (dashed curve) vs measured (solid curve) results of the noise at the output of the current driver. Higher frequency noise measurements could not be performed due to equipment limitations.

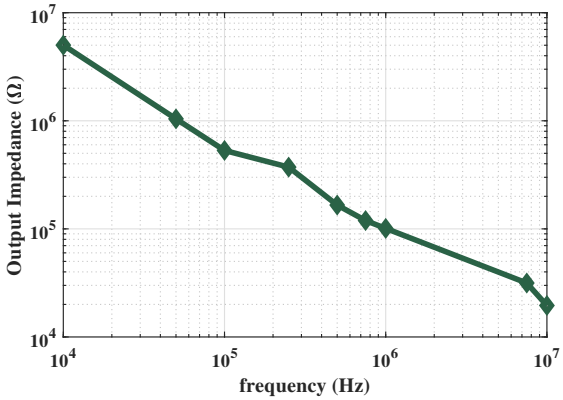

Figure 12. Output impedance vs frequency for the current driver. The measured output impedance is 101 kΩ at 1 MHz, and 19.5 kΩ at 10 MHz.

1 mA_{pp} of current was injected into the load. A 100 Ω sense resistor with 0.1% tolerance was included at the output to measure the accurate current from the current driver. The voltage across the sense resistor was captured by the data acquisition system. A digital matched filter in MATLAB was then used to extract the amplitude and phase of the complex load. The value of the passive components used in the setup was measured using an LCR meter and incorporated into the accuracy calculations. An average of 50 measurements was performed for each frequency point to obtain accurate results. The measured Cole-Cole plot for the complex impedance setup is shown in figure 14. The

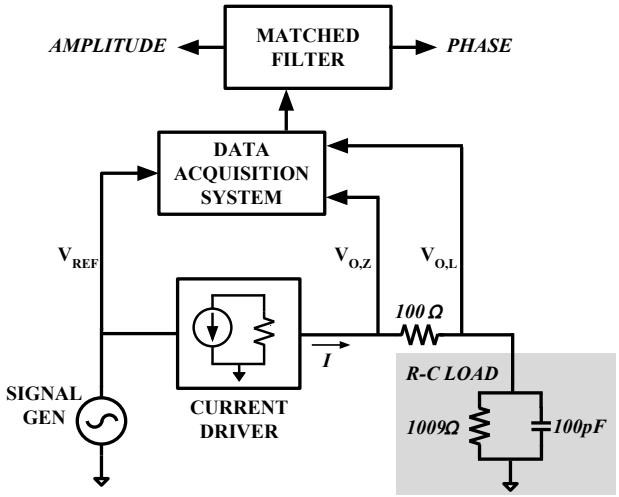

Figure 13. Setup for current driver testing. Input signal is fed by a signal generator and the Voltage across the sense resistor (is captured by the data acquisition system. Amplitude and phase extraction is performed in the digital domain with a matched filter.

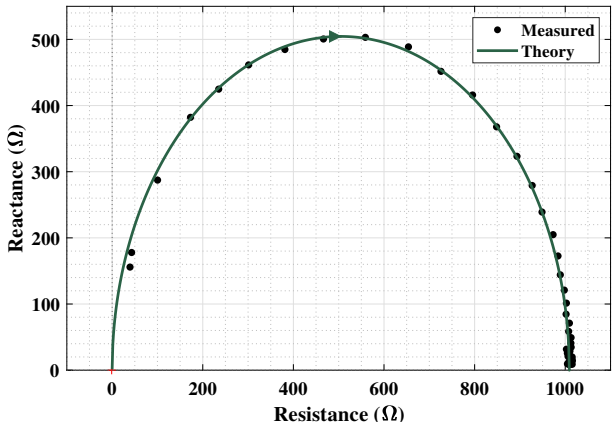

Figure 14. Cole-Cole plot for a parallel R-C load shown in figure 13 to model the complex tissue impedance.

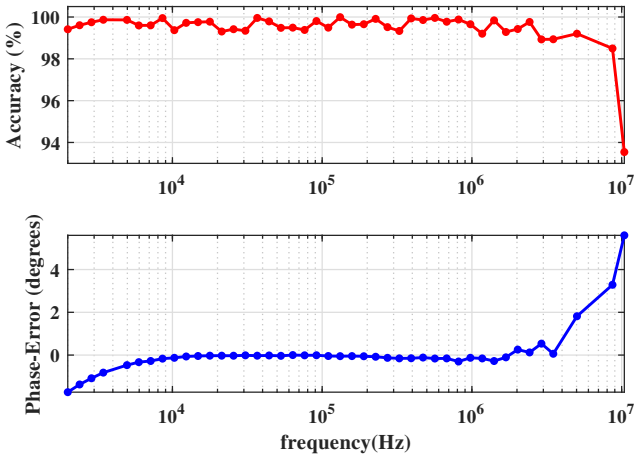

Figure 15. Accuracy of measured amplitude and phase error plot for the complex R-C load impedance.

accuracy of the measured amplitude is given as,

$$\text{Accuracy}(\%) = \left(1 - \frac{\text{V}_{\text{meas}} - \text{V}_{\text{theory}}}{\text{V}_{\text{theory}}}\right) \cdot 100$$

where V_{meas} is the measured voltage at the load and V_{theory} is the voltage obtained from theory. Calibration data is collected for the measurements to account for board parasitics. The measured amplitude accuracy and phase error over frequencies is plotted in figure 15. An accuracy of over 99.3% is maintained over most of the frequency range, dropping to 93.54% at 10 MHz. The phase error increases at frequencies greater than 4 MHz. This can be attributed primarily to board parasitics, ASIC packaging and test equipment limitations.

4.5. Saline Tank Measurements

To illustrate the functioning of the current driver in a full EIT system, saline tank experiments were performed to obtain impedance images. Sixteen copies of the current driver were integrated in a 16-electrode EIT system, which we used to measure and image a saline tank. An 8.5 cm diameter tank was filled with a saline solution of conductivity 1000 μS/cm which is in the range of value reported for different breast tissues (Jossinet and Schmitt, 1999). The tank was fitted with conductive polymer plugs in contact with alligator clip electrodes attached to the tank. The spacing between electrodes was 3.25 cm. An initial experiment consisted of filling the tank with saline to a height of 1.27 cm to form a baseline measurement. Subsequent experiments were performed with a brass rod of diameter 1.3 cm placed at the center of the saline tank and then close to electrode 1. The image obtained from the saline tank experiment using reconstruction algorithms (Murphy et al., 2017) is shown in figure 16.

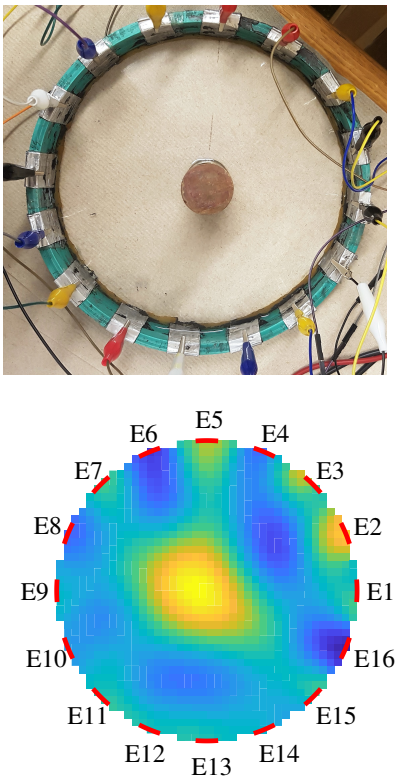

Figure 16. Saline tank setup and reconstructed image. (a) Brass rod of 1.3 cm diameter placed at the center of the saline tank with water depth of 1.27 cm and conductivity 1000 μS/cm. (b) Reconstructed image for the saline tank setup.

Table 1. Measured Performance and Comparison.

Parameter	(Yan et al., 2011)	(Constantinou et al., 2015)	(Hong et al., 2015)	(Kim et al., 2017)	(Wu et al., 2018)	This Work
Architecture	Differential Current Generator	Negative Feedback	Differential Current Generator	Differential Current Generator	Negative Feedback	Current Conveyor II
Bandwidth	90 kHz	$\leq$ 1 MHz	$\leq$ 200 kHz	256 kHz	500 kHz	**100 Hz - 10 MHz**
Output Impedance	$>$ 560 kΩ @ 90kHz	360 **k**Ω @1 MHz	–	–	**1.12 MΩ @ 500 kHz**	101 kΩ @ 1 MHz, 19.5 kΩ @ 10 MHz
Maximum Output Current (peak-peak)	350 μA	1 mA	1 mA	1 mA	**6 mA**	1.2 mA
THD (current) (frequency)	0.81 % (250 μA) (Unknown)	$<$ 0.1% (1 mA) (50 kHz)	$<$ 0.1% @ 0.1 mA (Unknown)	$<$ 0.47% (1 mA) (128 kHz)	$<$ 0.18% (6 mA) (500 kHz)	**$<$ 0.14% (1.2 mA) (500 kHz) $<$ 0.7% (1.2 mA) (10 MHz)**

5. Discussion

Since the number of pads available on the ASIC were limited, the output pad for current injection from the current driver at terminal Z could not be sufficiently isolated. This caused additional coupling capacitance with adjacent signals on chip, which would degrade high frequency output impedance of the current driver. The current driver achieves wide-band operation up to 10 MHz, necessary for EIT prostate and breast cancer detection. The THD values achieved are an improvement from previously reported integrated designs. The use of indirect feedback compensation enables wide-band operation with a small compensation capacitor. This is especially helpful when integrating multiple EIT channels on a single ASIC. On-chip bandgap references for biasing would improve the integration of the current driver in building multiple channel EIT systems. Additionally, a future iteration for the current driver would require careful placement of the output port, so that it is sufficiently isolated from adjacent nodes to reduce the parasitics. Table 1 shows a comparison with previously-reported current drivers.

6. Conclusion

A CMOS wide-band current driver based on current conveyor architecture is presented. High linearity is achieved by the use of a resistor for current generation in the V-I conversion phase, whereas high accuracy is obtained by the use of a gain boosted cascode structure for high output impedance. The design was fabricated in the 0.18-μm process and can deliver 1.2 mA of current up to frequencies of 10 MHz. The above performance is achieved while maintaining harmonic distortion of less than 1% essential for EIT imaging (Rao et al., 2018). A servo-loop circuit is designed for the output branch of the current driver to account for the DC blocking capacitor when injecting current into the human tissue. The current driver specifications have been measured using custom built PCBs and its performance characterized with a complex load impedance up to

10 MHz. A 16-electrode EIT system which incorporates the current driver was used to measure a saline tank setup and an image is obtained. The circuit is intended for use in active electrodes and EIT applications which require high frequency of operation to detect cancerous tissues.

Acknowledgments

This work was supported in part by the U.S. National Science Foundation, under Grant No. 1418497, U.S. Department of Defense CDMRP Grant Nos. W81XWH-15-1-0572 and W81XWH-15-1-0571.

References

Baker, R. J. (2010). *CMOS: Circuit Design, Layout, and Simulation, Third Edition*.

Carusone, T. C., Johns, D., Martin, K. W. K. W. and Johns, D. (2012). *Analog integrated circuit design*, John Wiley & Sons.

Constantinou, L., Bayford, R. and Demosthenous, A. (2015). A Wideband Low-Distortion CMOS Current Driver for Tissue Impedance Analysis, *IEEE Transactions on Circuits and Systems II: Express Briefs* **62**(2): 154–158.

Constantinou, L., Triantis, I. F., Bayford, R. and Demosthenous, A. (2014). High-Power CMOS Current Driver With Accurate Transconductance for Electrical Impedance Tomography, *IEEE Transactions on Biomedical Circuits and Systems* **8**(4): 575–583.

Cook, R., Saulnier, G., Gisser, D., Goble, J., Newell, J. and Isaacson, D. (1994). ACT3: a high-speed, high-precision electrical impedance tomograph, *IEEE Transactions on Biomedical Engineering* **41**(8): 713–722.

Halter, R. J., Hartov, A. and Paulsen, K. D. (2008). A broadband high-frequency electrical impedance tomography system for breast imaging, *Biomedical Engineering, IEEE Transactions on* **55**(2): 650–659.

Hong, S., Lee, J., Bae, J. and Yoo, H. J. (2015). A 10.4 mw electrical impedance tomography soc for portable real-time lung ventilation monitoring system, *IEEE Journal of Solid-State Circuits* **50**(11): 2501–2512.

Jivet, I. and Dragoi, B. (2008). On-electrode autonomous current generator for multi-frequency EIT, *Physiological Measurement* **29**(6): S193–S201.

Jossinet, J. (1998). The impedivity of freshly excised human breast tissue, *Physiological Measurement* **19**(1): 61–75.

Jossinet, J. and Schmitt, M. (1999). A review of parameters for the bioelectrical characterization of breast tissue, *Annals of the New York Academy of Sciences*, Vol. 873, pp. 30–41.

Kim, M., Jang, J., Kim, H., Lee, J., Lee, J., Lee, J., Lee, K.-R., Kim, K., Lee, Y., Lee, K. J. and Yoo, H.-J. (2017). A 1.4-mohm-Sensitivity 94-dB Dynamic-Range Electrical Impedance Tomography SoC and 48-Channel Hub-SoC for 3-D Lung Ventilation Monitoring System, *IEEE Journal of Solid-State Circuits* **52**(11): 2829–2842.

Lionheart, W. R. B., Kaipio, J. and McLeod, C. N. (2001). Generalized optimal current patterns and electrical safety in EIT, *Physiological Measurement*, Vol. 22, IOP Publishing, pp. 85–90.

McEwan, A., Cusick, G. and Holder, D. S. (2007). A review of errors in multi-frequency EIT instrumentation, *Physiological Measurement*, Vol. 28, IOP Publishing, pp. S197–S215.

Murphy, E. K., Mahara, A. and Halter, R. J. (2017). Absolute Reconstructions Using Rotational Electrical Impedance Tomography for Breast Cancer Imaging, *IEEE Transactions on Medical Imaging* **36**(4): 892–903.

Rao, A., Teng, Y.-C., Schaef, C., Murphy, E. K., Arshad, S., Halter, R. J. and Odame, K. (2018). An Analog Front End ASIC for Cardiac Electrical Impedance Tomography, *IEEE Transactions on Biomedical Circuits and Systems* **12**(4): 729–738.

Saulnier, G., Blue, R., Newell, J., Isaacson, D. and Edic, P. (2001). Electrical impedance tomography, *IEEE Signal Processing Magazine* **18**(6): 31–43.

Saxena, V. (2007). Indirect Feedback Compensation Technique for Multi-Stage Operational Amplifiers, *Boise State University Theses and Dissertations* .

Sedra, A. and Smith, K. (1970). A second-generation current conveyor and its applications, *IEEE Transactions on Circuit Theory* **17**(1): 132–134.

Tucker, A. S., Fox, R. M. and Sadleir, R. J. (2013). Biocompatible, High Precision, Wideband, Improved Howland Current Source With Lead-Lag Compensation, *IEEE Transactions on Biomedical Circuits and Systems* **7**(1): 63–70.

Wilson, B. (1990). Recent developments in current conveyors and current-mode circuits, *IEE Proceedings G Circuits, Devices and Systems* **137**(2): 63.

Wu, Y., Jiang, D., Bardill, A., de Gelidi, S., Bayford, R. and Demosthenous, A. (2018). A high frame rate wearable eit system using active electrode asics for lung respiration and heart rate monitoring, *IEEE Transactions on Circuits and Systems I: Regular Papers* **65**(11): 3810–3820.

Yan, L., Bae, J., Lee, S., Roh, T., Song, K. and Yoo, H.-J. (2011). A 3.9 mW 25-Electrode Reconfigured Sensor for Wearable Cardiac Monitoring System, *IEEE Journal of Solid-State Circuits* **46**(1): 353–364.

Zeki, A. and Kuntman, H. (1997). Accurate and high output impedance current mirror suitable for CMOS current output stages, *Electronics Letters* **33**(12): 1042.

Fused-data Transrectal Electrical Impedance Tomography for Prostate Cancer Imaging
EK Murphy, X Wu, RJH Halter

Introduction: Prostate cancer is a significant problem affecting 1 in 7 men. Unfortunately, the diagnostic gold-standard, 12-core transrectal ultrasound (TRUS)-guided biopsy, misses 10-30% of all cancers, and the addition of targeted magnetic resonance imaging (MRI)-guided biopsy increases detection of high-grade cancers but misses more low-grade cancers. A number of ex-vivo studies have shown that benign and cancerous prostate tissue exhibit significant differences in electrical properties. This has led to the investigation of Transrectal Electrical Impedance Tomography (TREIT), an electrical property imaging modality, to help improve US/MRI-guided biopsies. Presently, accurate EIT images of realistic gel-based prostate phantoms have been produced by fusing EIT data that could be collected during a TRUS-guided biopsy. The work presented here advances our prior efforts in fused data (fd)-TREIT; specifically, improvements include using 1) a realistic number of measurements that could be recovered during a standard 12-core TRUS-guided biopsy, 2) prostate phantoms with gelatine inclusions that can yield realistic cancer-to-benign contrasts, 3) electromagnetically (EM)-tracked TRUS and biopsy probes which makes fd-TREIT possible, and 4) incorporation of MRI images for improved prior information compared to TRUS images.

Materials and Methods: Gelatine phantoms were produced with gelatine inclusions containing graphite (US contrast) and copper sulphate (MRI-contrast). MRI images were used to segment the prostate and gelatine inclusion/s. EM-tracking using an NDI Aurora V2 system provided 6 degree-of-freedom states of the TRUS probe and biopsy needle for each EIT measurement. MRI data was registered to the EM-tracking data via target points on the rig holding the prostate (see Fig. 1A). For each experiment, 10 x/y-locations (needle insertion sites) were measured at 3 depths yielding a total of 30 locations. The fd-TREIT approach was based on a standard Gauss-Newton algorithm utilizing a soft-regularization technique via the segmented prostate boundary. The fusion process utilizes a single finite element method (FEM) mesh (776k nodes, 4.4M elements) that has the TRUS probe and biopsy needle encoded. The mesh was transformed for each state and related to a fixed coarse inverse mesh using the dual-mesh method. Absolute reconstructions were performed.

Results and Discussion: Reconstructions of a two-inclusion test (Fig. 1A) yields two thresholded high conductive regions (yellow) that are located mainly within the true inclusion regions (Figure 1B) with minimal artifacts (see cross-sectional image), but are significantly smaller than the true inclusions. Inclusions were produced with a 3-1 inclusion-to-background contrast. Average frequency-dependent conductivities from a single-inclusion reconstruction resemble the true inclusion conductivities (Fig. 1C). Black dots illustrate the location of the biopsy electrodes location for each measurement (Fig. 1B), which reveal the prostate was not uniformly sampled. Ongoing research includes 1) developing guidance, tracking software to improve the spatial sampling of the prostate (which should improve reconstructions), 2) investigating methods to decrease positioning and registration errors (e.g. modifications to the prostate rig), and 3) evaluating the procedure on more challenging phantoms (smaller inclusions and smaller contrasts).

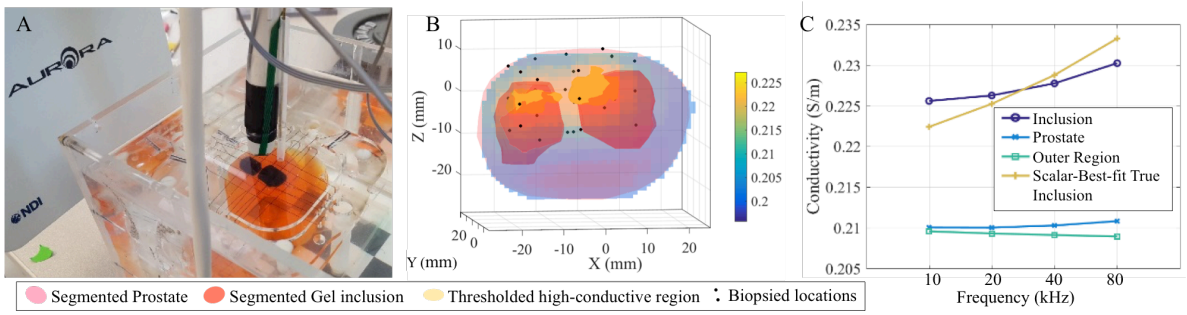

Figure 1. A. 2-inclusion test showing the TRUS probe, needle, EM-tracker prostate (orange) and inclusions (black), B. thresholded EIT reconstruction, and C. frequency-dependent reconstructions of a similar 1-inclusion phantom to A.

Conclusions: The fd-TREIT utilizing EM-tracked data and MRI segmented prostate boundaries was successful in producing reconstructions that resemble the true (frequency-dependent) conductivity distribution with minimal artifacts. This study represents significant steps towards bringing this technology towards pre-clinical evaluation.

Acknowledgements: This work was supported in part by the Department of Defense Congressionally Directed Medical Research Program under Grant W81XWH-15-1-0102.

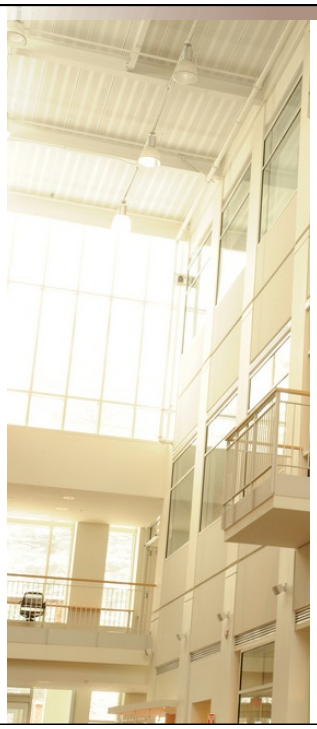

THAYER SCHOOL OF ENGINEERING AT DARTMOUTH

Fused-data Transrectal Electrical Impedance Tomography for Prostate Cancer Imaging

Ethan K Murphy[1], Xiaotian (Dennis) Wu[1], and Ryan J Halter[1,2]

[1]Thayer School of Engineering, Dartmouth College, Hanover, NH, USA, ethan.k.murphy@dartmouth.edu
[2]Geisel School of Medicine, Dartmouth College, Hanover, NH, USA, Ryan.J.Halter@dartmouth.edu

engineering.dartmouth.edu
18 October 2018

The Problem

THAYER SCHOOL OF ENGINEERING AT DARTMOUTH

- **Prostate cancer is a serious problem**
  - About 1 in 7 men will be diagnosed with the disease, and
  - It is the 2nd leading cause of cancer death in men[1]
- **The current gold-standard of diagnosis is transrectal ultrasound (TRUS)-guided needle biopsy[2]**
- **Unfortunately, this test has drawbacks including yielding many false negatives**
  - >30% false negatives for 12-core biopsies,[4]
  - A major reason for this is the cores only sampling a very small part of the prostate (< 1% of a standard 24 cm^3prostate)[5]
- **There is a need for improved minimally-invasive prostate cancer detection**

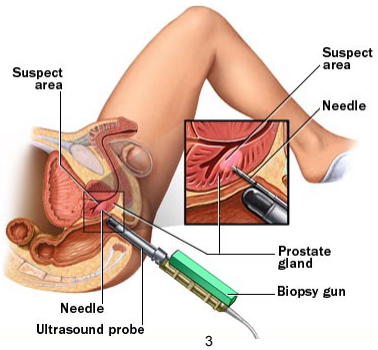

3

References
1. American Cancer Society. American Cancer Society Facts & Figures 2015.
2. Shariat, S. F., & Roehrborn, C. G. *Reviews in Urology*, *10*(4), 262–280, 2008.
3. Image: http://www.drtimnathan-urology.com.au/transrectal-ultrasound-Guided-biopsy-of-the-prostate
4. Serefoglu EC, et al., *Canadian Urological Association Journal*. 2013
5. Harnden, P., et al., Cancer, 112: 971–981, 2008.

2

Can Electrical Property Imaging Help?

THAYER SCHOOL OF ENGINEERING AT DARTMOUTH

- Ex-vivo studies have established that electrical impedance can discriminate between cancerous and benign prostate tissue
- The highest contrast have been found for multi-frequency (complex) conductivity parameters
- Electrical Imaging appears possible given the

Metric	AUC
Characteristic frequency, f_c	0.82
σ_{inf}	0.77

Picture from [A]

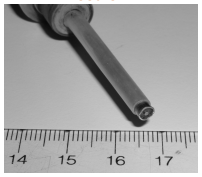

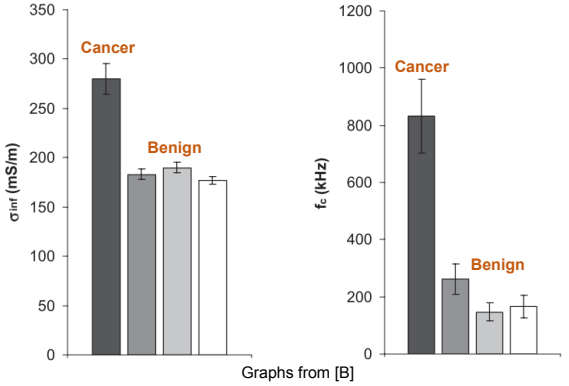

Graphs from [B]

Reference
A. Halter, R. J., Hartov, A., Heaney, J. a., Paulsen, K. D. & Schned, A. R. Electrical impedance spectroscopy of the human prostate. IEEE Trans. Biomed. Eng. 54, 1321–1327 (2007).
B. Halter, R. J., Schned, A., Heaney, J., Hartov, A. & Paulsen, K. D. Electrical Properties of Prostatic Tissues: II. Spectral Admittivity Properties. J. Urol. 182, 1608–1613 (2009).

Electrical Impedance Tomography: Overview

THAYER SCHOOL OF ENGINEERING AT DARTMOUTH

True (unknown) conductivity

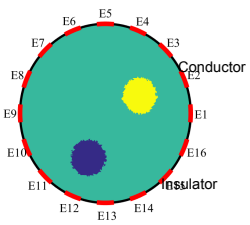

Measure on the Unknown Conductivity

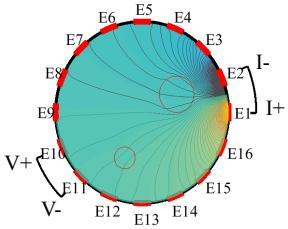

Difference using a measured (or simulated) homogeneous conductivity

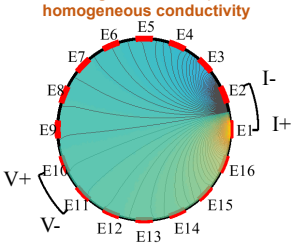

- EIT produces images of conductivity by measuring voltages on boundary electrodes from sets of current patterns
- The reconstruction is performed via the solving the following linearized model-fitting problem:

$$E(\boldsymbol{\delta\sigma}) = \|\boldsymbol{J\delta\sigma} - \boldsymbol{\Delta V}\|_2^2 + \lambda^2\|\boldsymbol{L\delta\sigma}\|_2^2$$

$$\delta\tilde{\sigma} = (\boldsymbol{J}^T\boldsymbol{J} + \lambda\boldsymbol{L}^T\boldsymbol{L})^{-1}\boldsymbol{J}^T(\boldsymbol{V}_{Meas} - \boldsymbol{V}_{Sim}(\tilde{\sigma}_0))$$

$\delta\tilde{\sigma}$: Conductivity perturbation from a known conductivity	$\boldsymbol{V}_{Meas}$: Measured voltages
$\boldsymbol{J}$: Jacobian	$\boldsymbol{V}_{Sim}(\tilde{\sigma}_0)$: Simulated voltages from a known conductivity
$\boldsymbol{L}$: Regularization matrix	

EIT Reconstruction

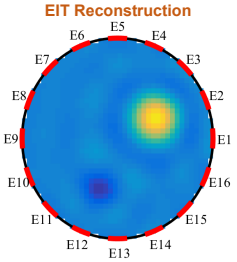

Approach: Add EIT to TRUS-guided biopsies

THAYER SCHOOL OF ENGINEERING AT DARTMOUTH

- Our approach is add electrodes onto equipment used in standard TRUS-guided biopsies to allow for Electrical Impedance Imaging
- We developed 1) A sono-lucent electrode array (20 electrodes) to be placed on the front of the TRUS probe and 2) Two rows of 4 electrodes that are wrapped around the biopsy needle
- Needle guides and biopsy gun mounts have also been developed
- The EIT problem then constructs images from combinations of electrodes in this open domain

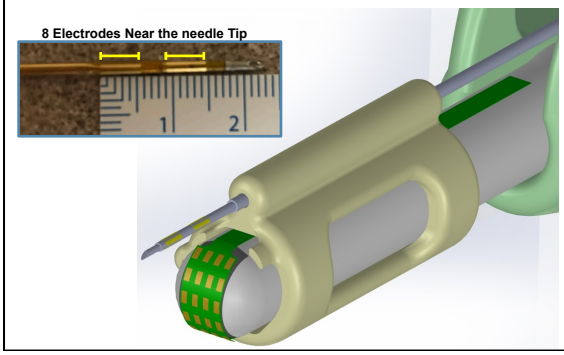

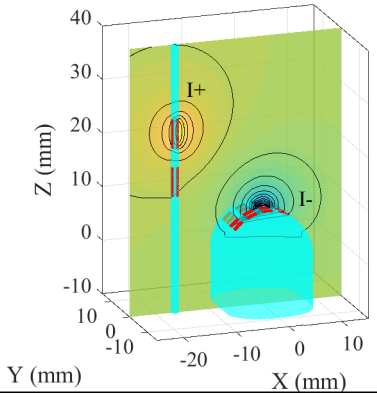

5

EIT Challenges & Solutions

THAYER SCHOOL OF ENGINEERING AT DARTMOUTH

- There are significant challenges to EIT in this application, primarily 1) a lack of sensitivity and 2) open domain (lack of full boundary data)

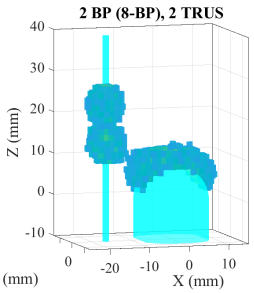

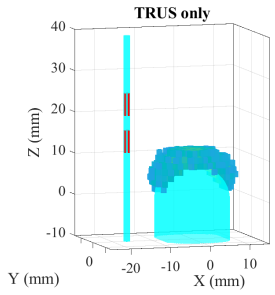

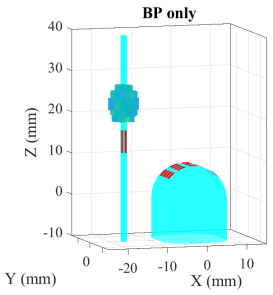

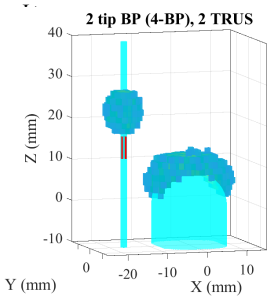

Fusing Data from Multiple Biopsy Sites

THAYER SCHOOL OF ENGINEERING AT DARTMOUTH

- There are significant challenges to EIT in this application, primarily 1) a lack of sensitivity and 2) open domain (lack of full boundary data)

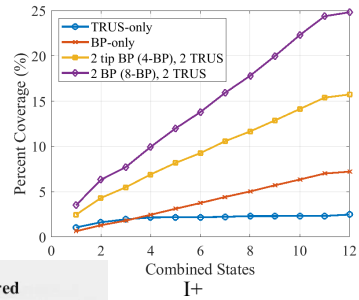

I+

I-

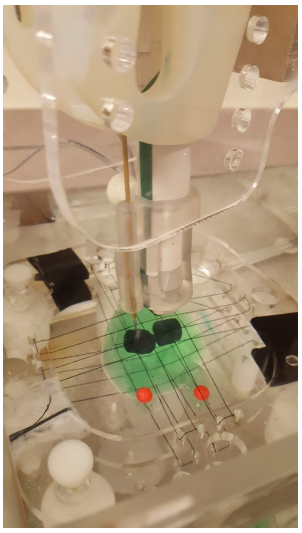

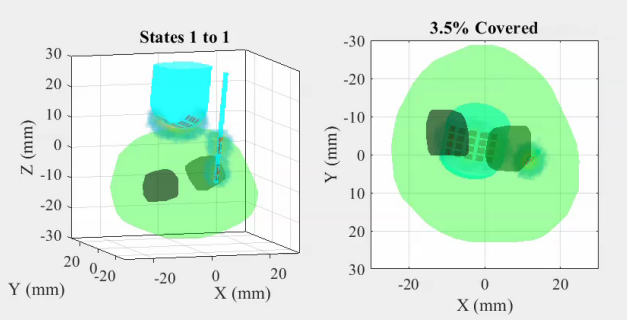

7

Methods: Jacobian via the Dual Mesh Method

THAYER SCHOOL OF ENGINEERING AT DARTMOUTH

- Choose a fixed coarse mesh (red blocks)
- For each we state transform the mesh and determine which FEM nodes are associated with each coarse voxel (cyan nodes in the blue block for each state)
- Transforming the fine Jacobian for each state to this coarse grid provides proper fusion of the data

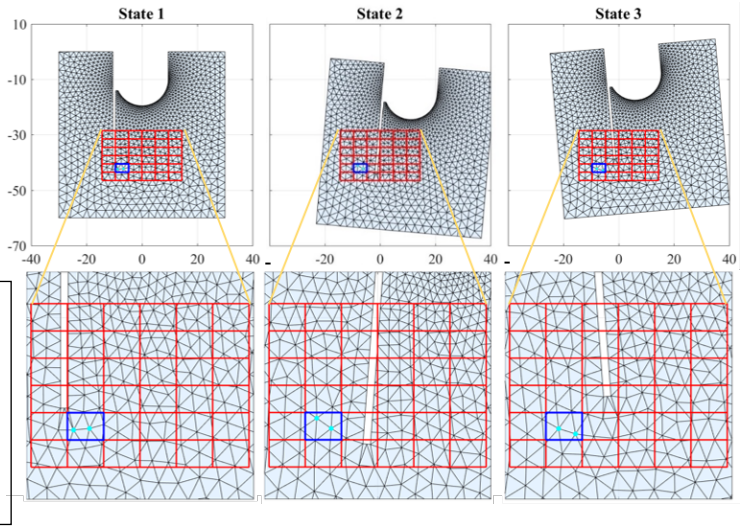

Data Fusion

Fusion is accomplished by concatenating the data, which allows for the simultaneous minimization across all states:

$$E(\boldsymbol{\delta\sigma}) = \frac{1}{N_S}\|\boldsymbol{J_{FD}\delta\sigma} - \boldsymbol{\Delta V_{FD}}\|_2^2 + \lambda^2\|\boldsymbol{L}(\boldsymbol{\sigma_0} + \boldsymbol{\delta\sigma} - \boldsymbol{\sigma_{REF}})\|_2^2$$

where the fused data Jacobian is given by

$$\boldsymbol{J_{FD}} = \left[\boldsymbol{J}^T(s_1) \quad \boldsymbol{J}^T(s_2) \quad \cdots \quad \boldsymbol{J}^T(s_{N_S})\right]^T$$

8

Methods: Data Segmentation & Registration

THAYER SCHOOL OF ENGINEERING AT DARTMOUTH

- Ultrasound images are collected during the data collection, by using the EM-tracking data and 2D contours of the (gel) prostate are combined to construct a 3D surface
- MR segmentation is also performed
- The MR data is registered with the EM-tracking data (and consequently EIT and US data) by aligning a set of points on the rig that holds the prostate.

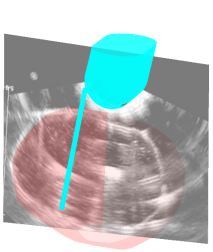

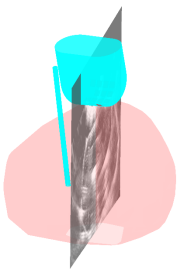

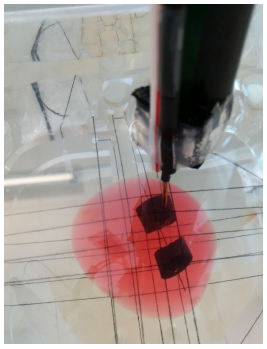

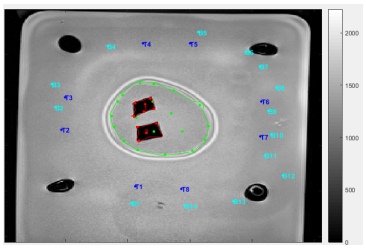

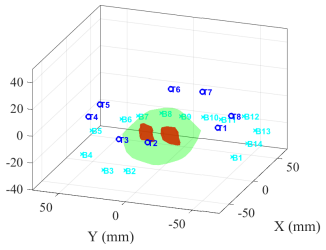

9

Experiment 4: Prostate 11

THAYER SCHOOL OF ENGINEERING AT DARTMOUTH

- Example of two graphite inclusions

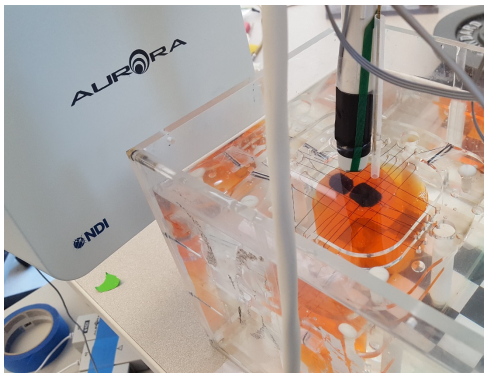

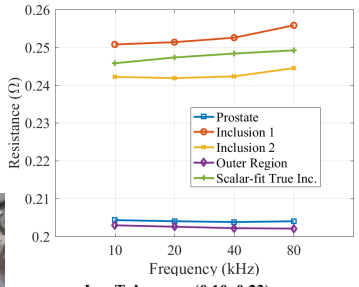

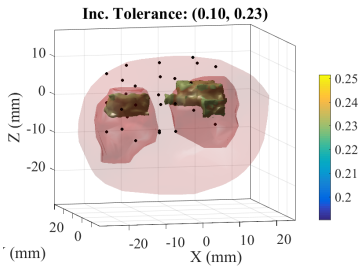

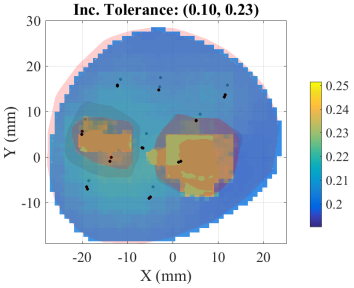

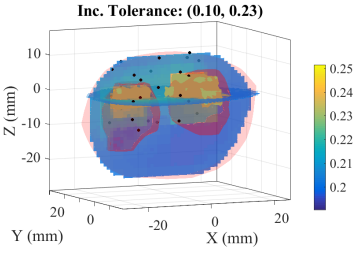

10

Experiment 4: Prostate 11

THAYER SCHOOL OF ENGINEERING AT DARTMOUTH

- Notes
- All measurements are within the prostate (gel) and at roughly the same height.
- 12 states were used.
- 3447 IIVV patterns were used

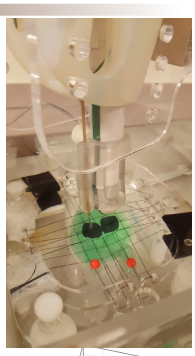

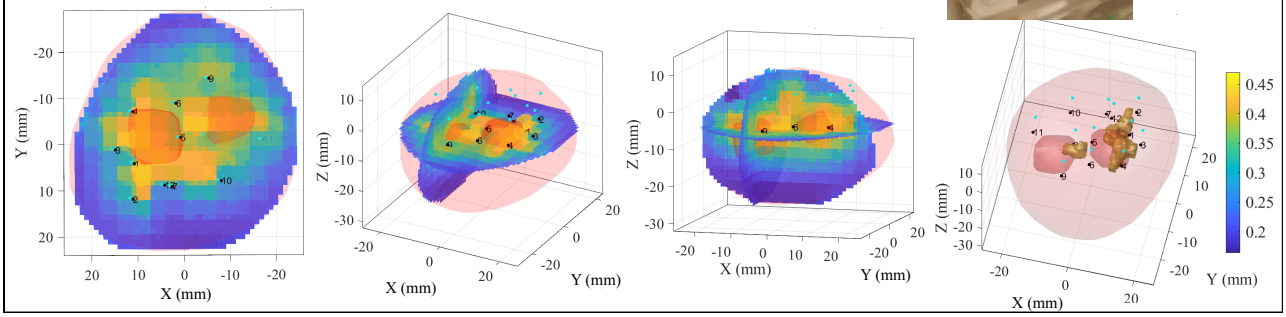

Conclusions and Next Steps

THAYER SCHOOL OF ENGINEERING AT DARTMOUTH

- **Conclusions**
  - Absolute reconstruction of prostate phantoms a success
  - There has been significant speed-up of the algorithm, but more is needed for (near) real-time reconstructions
- **Next Steps**
  - Improvement of needle housing to ensure repeatable needle trajectories
  - Ex-vivo prostate study!

12

Acknowledgements & Thanks

- Prof. Ryan Halter
- Dennis Wu
- Alicia Everett

Funding: This work was supported in part by the Department of Defense Congressionally Directed Medical Research Program under Grant W81XWH-15-1-0102

- Dartmouth's & Dartmouth Hitchcock Medical Center's resources
  - Thayer's computer servers
  - MRI in DHMC's Advanced Imaging Center

THANKS!

13

Absolute Phantom Reconstructions using Fused-Data EIT

Ethan K. Murphy[1], Xiaotian Wu[1], and Ryan J. Halter[1,2]

[1]Thayer School of Engineering, Dartmouth College, Hanover, NH, USA, ethan.k.murphy@dartmouth.edu
[2]Geisel School of Medicine, Dartmouth College, Hanover, NH, USA, Ryan.J.Halter@dartmouth.edu

Abstract: Absolute reconstructions from gelatine prostate phantoms using fused-data transrectal electrical impedance tomography (fd-TREIT) incorporating biopsy electrode measurements are produced. The successful reconstructions are important steps toward ex-vivo and in-vivo evaluation of the technology.

1 Introduction

Detecting prostate cancer non-invasively is clinically challenging. Low threshold PSA-based screening has a high sensitivity, but low specificity due to numerous benign conditions elevating PSA levels [1]. Men with elevated levels of PSA are typically subject to an image-guided biopsy protocol for more accurate diagnosis. Unfortunately, transrectal ultrasound (TRUS)-guided biopsies miss 10-30% of all cancers [1]. A number of ex-vivo studies have shown that electrical properties exhibit significant differences between benign and cancerous prostate [2]. We have previously developed an fd-TREIT system for prostate imaging that fuses tetra-polar impedance data recorded from 18 sonolucent electrodes adhered to a TRUS probe and 4 electrodes integrated on the tip of a biopsy needle. The work presented here advances our prior efforts in fd-TREIT [3]; specifically, improvements include using 1) a realistic number of measurements that could be recovered during a standard 12-core TRUS-guided biopsy, 2) prostate phantoms with metal, plastic, and gelatine inclusions, 3) electromagnetically (EM)-tracked TRUS and biopsy probes, and 4) a parallelized-software implementation providing 8x speed-up for absolute reconstructions.

2 Methods

Gelatine phantoms were produced with either 3 inclusions (2 metal and 1 plastic bead, Fig. 1B) or one large gelatine/graphite inclusion (Fig. 1A). TRUS images were used to segment the prostate and gelatine inclusion. EM-tracking using an NDI Aurora V2 system provided 6 degree-of-freedom states of the TRUS probe and biopsy needle for each EIT measurement and of the true bead locations. For each experiment, 10 x/y-locations (needle insertion sites) were measured at 3 depths yielding a total of 30 measurement locations.

The fd-EIT approach was based on a standard Gauss-Newton algorithm using a regularization scheme optimized for open domains [4]. The fusion process utilizes a single finite element method (FEM) mesh (776k nodes, 4.4M elements) that has the TRUS probe and biopsy needle encoded. The mesh was transformed for each state and related to a fixed coarse inverse mesh using the dual-mesh method. The measurements and Jacobians are concatenated so the problem can be solved as if it were a standard EIT problem. Absolute reconstructions required 90 (30x3) forward solves and 30 Jacobian calculations for each iteration. Three forward solves per state are due to the standard update and a parabolic linear search algorithm. Matlab's *parfor* with 16 workers solved the forward problems using Pardiso yielding a 8x speedup compared to serial runs while using up to ~150 GB of RAM. Each iteration took approximately 40 minutes, yielding total times of ~3.3 hours for 5 iterations.

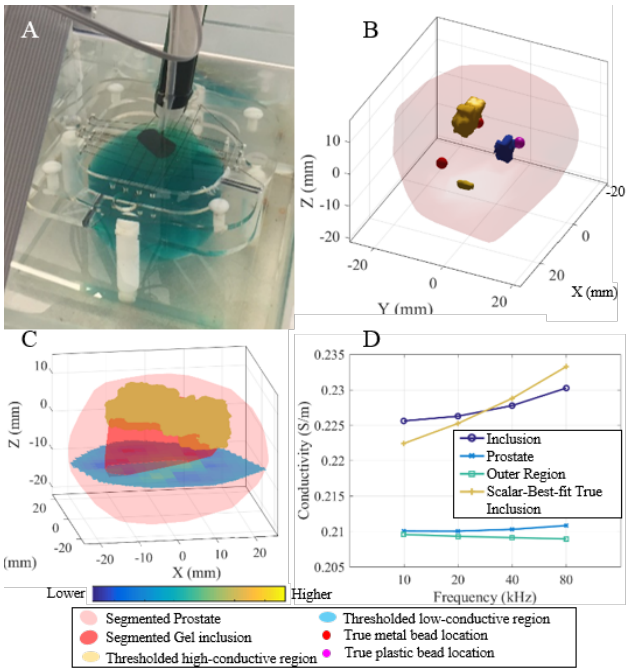

Figure 1: A. Setup for a prostate and gel inclusion experiment, B. absolute reconstructions of a 3 inclusion test, C. absolute reconstruction of the gel inclusion from A, and D. spectral results of the average of each region from C at 10, 20, 40, and 80 kHz.

The 3-inclusion experiment resulted in average position errors of 6.4 mm. The gel inclusion reconstruction resulted in 44% of the thresholded volume within the true inclusion volume and yielded frequency-dependent conductivities resembling the true inclusions.

3 Conclusions

This study represents significantly steps towards bringing this technology towards pre-clinical evaluation. Further study of EM data and TRUS images can likely improve the results and further speed-up can likely be accomplished.

4 Acknowledgements

This work was supported in part DoD CDMRP Grant W81XWH-15-1-0571.

References

[1] Campbell's Urology, 9th ed, P. Walsh. 2007, Saunders: Philadelphia
[2] R. J. Halter, et al., IEEE Trans. Bio. Eng., 54:,1321-1327, 2007.
[3] E.K. Murphy, et al., EIT Conf., Dartmouth, NH, USA, June 2017.
E.K. Murphy, et al., IEEE Trans Med. Imag., 35:1593-1603, 2017.

A Coupled US/EIT System for Assessing Muscle Health

Ethan K. Murphy[1], Joseph Skinner[1], Maria Martucci[2], Seward Rutkove[2] and Ryan Halter[1,3]

[1]Thayer School of Engineering, Dartmouth College, Hanover, NH, ethan.k.murphy@dartmouth.edu

[2]Beth Israel Deaconess Medical Center, Boston, MA, USA srutkove@bidmc.harvard.edu

[3] Geisel School of Medicine, Dartmouth College, Hanover, NH, USA

w

Abstract: Our initial patient study of a combined ultrasound (US) and Electrical Impedance Tomography (EIT) system on a small cohort of patients has shown significant differences between longitudinal and transverse muscle fibre conductivity reconstructions – *an important validation test* - and has shown a capability to distinguish healthy from diseased tissue.

1 Introduction

Electrical Impedance Myography (EIM) has shown significant promise as a diagnostic tool capable of distinguishing healthy from diseased muscle tissue in a number of neuromuscular diseases [1]. Electrical Impedance Tomography (EIT) has the potential to enhance EIM and improve the clinical value by providing reconstructions that spatially map the EIM signatures and specifically 1) properly account for variations in skin/subcutaneous fat layers across patients and 2) differentiate contributions from different muscles within the tissue volume interrogated. This study presents a coupled ultrasound (US) and EIT system used to record data from a small cohort of patients.

2 Methods

A combined US/EIT system (Fig. 1A-B) was used to record measurements on both legs from a small cohort of patients (4) who had a neuromuscular disorder affecting at least one side. Repeated, longitudinal and transverse data were acquired from a total of nine sites. Data corresponding to each measurement consisted of the US image and EIT voltages. Segmented tissues from the US images were used to construct Finite Element Method (FEM) meshes and the regularization matrix of the forward and inverse problems, respectively.

The inverse algorithm relied on a standard Gauss-Newton approach employing generalized Tikhonov regularization. The error function is given by

$$E(\boldsymbol{\delta\sigma}) = \|\mathbf{J}\boldsymbol{\delta\sigma} - \Delta\boldsymbol{v}\|_2^2 + \lambda\|\mathbf{L}(\boldsymbol{\sigma_0} + \boldsymbol{\delta\sigma} - \boldsymbol{\sigma}_{REF})\|_2^2 \quad (1)$$

where $\boldsymbol{\delta\sigma}$ is the conductivity update, $\mathbf{J}$ is the Jacobian, $\mathbf{L}$ is the regularization matrix, λ is the Tikhonov regularization factor, $\boldsymbol{\sigma}_{REF}$ is a reference conductivity, and $\Delta\boldsymbol{v}$ is the vector difference between measured, $\boldsymbol{v}_{Meas}$, and simulated voltages, $\boldsymbol{v}_{Sim}(\boldsymbol{\sigma}_0)$. Soft-regularization is implemented by assigning muscle, skin/subcutaneous fat, and US gel conductivity values (from literature) of $\boldsymbol{\sigma}_{REF}$ based on the location of each component. The $\mathbf{L}$-matrix was diagonal with entries equal to the sensitivity of each inverse voxel. Absolute reconstructions were performed using 5 iterations and Tikhonov parameter of 1e5 on frequencies of 10, 20, 40, and 80 kHz. The regularization approach is similar to that used in [2].

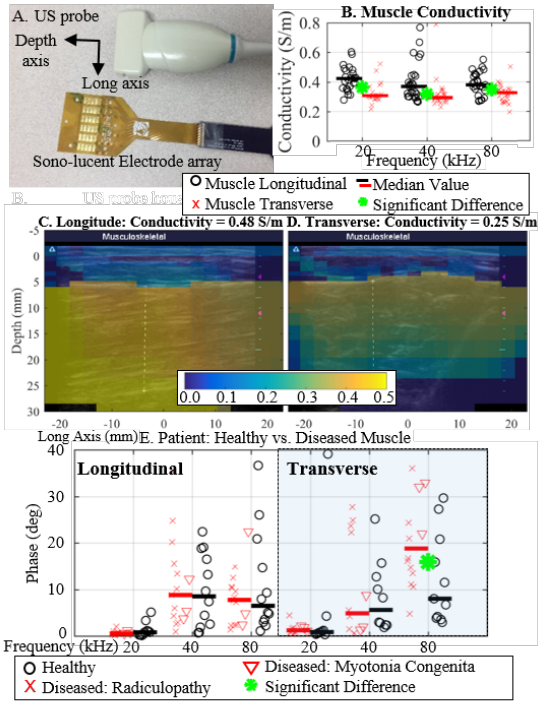

Figure 1: The combined system was composed of the A. the US probe and sono-lucent electrode array. B. Longitudinal reconstructions were found to be larger (with significance) than transverse (example C-D). E. The phase at 80 kHz showed an ability to distinguish healthy from diseased tissue.

Significant differences between longitudinal and transverse muscle reconstructs were found at frequencies of 20, 40, and 80 kHz (Fig. 1B). Example longitudinal and transverse EIT reconstructions from a single site overlaid on their respective US images (Fig. 1C-D) shows the expected result of a larger conductivity in the longitudinal direction. Significant differences between healthy and diseases tissue were observed at 80 kHz for permittivity and phase values of the transverse cases (Fig. 1E).

3 Conclusions

This is the first study of a combined US/EIT system showing an ability to obtain clinically relevant information on muscle condition. We hope to make minor modifications to the system and perform a larger clinical study.

4 Acknowledgements

This work was supported in part by the DoD CDMRP Grant W81XWH-15-1-0102.

References

[1] Rutkove, *Muscle and Nerve*, 40(6): 936–946, 2009

[2] Brooksby, *et al IEEE J Sel Top Quantum Electron,*9(2): 199-209, 2003

PROCEEDINGS OF SPIE

SPIEDigitalLibrary.org/conference-proceedings-of-spie

A real-time 4-bit imaging electrical impedance sensing biopsy needle for prostate cancer detection

Alicia C. Everitt, Preston K. Manwaring, Ryan J. Halter

Alicia C. Everitt, Preston K. Manwaring, Ryan J. Halter, "A real-time 4-bit imaging electrical impedance sensing biopsy needle for prostate cancer detection," Proc. SPIE 10578, Medical Imaging 2018: Biomedical Applications in Molecular, Structural, and Functional Imaging, 105781A (12 March 2018); doi: 10.1117/12.2293799

SPIE.

Event: SPIE Medical Imaging, 2018, Houston, Texas, United States

A real-time 4-bit imaging electrical impedance sensing biopsy needle for prostate cancer detection

Alicia C. Everitt*[a], Preston K. Manwaring[b], Ryan J. Halter[a]
[a]Dartmouth College, 14 Engineering Dr, Hanover, NH, USA 03755; [b]Rytek Medical Inc., 16 Cavendish Ct, Lebanon, NH USA 03766

ABSTRACT

Introduction: Prostate cancer is the second leading cause of cancer death in men. Biopsy serves as the primary tool for cancer diagnoses in these men. However, false-negative diagnosis following biopsy can be as high as 30% and even when detected via biopsy it can be difficult to accurately grade the cancer. Electrical properties of prostate cancer have been reported to be significantly different than benign prostate. We hypothesize that a custom tetrapolar-based electrical impedance sensing biopsy (EIS-Bx) needle will be able to detect electrical properties of surrounding tissue and provide a "4 bit" image for guidance to potential cancer locations. *Methods:* A custom EIS-Bx device was designed using four gold-plated electrode traces on a standard biopsy needle. A novel small form-factor impedance analyzer was designed to interface with the EIS-Bx needle. The EIS-Bx device was submerged in a saline bath while a high contrast inclusion was rotated in 90-degree increments around the needle. At each location, the impedance of 4 electrode configurations was recorded at 7 frequencies (ranging from 1kHz to 100kHz). The impedances of each quadrant were compared with the inclusion location to examine spatial differentiation. *Results:* Bipolar measurements clearly detected impedance changes correlated to inclusion presence across frequencies. These results validate the hypothesis of potential "4-bit" imaging for cancer detection and diagnostic guidance. *Conclusion:* Initial experiments successfully demonstrate spatial sensitivity to a moving inclusion using the EIS-Bx device. Future work will investigate the ability to differentiate cancer from benign tissue ex-vivo with quadrant specific resolution and to display this as a real-time map of prostate pathology.

Keywords: Electrical impedance, prostate cancer, bioimpedance, biopsy needle, EIS, real-time detection

1. INTRODUCTION

Prostate cancer is the second leading cause of cancer death in men, and one in seven men will be diagnosed with prostate cancer in their lifetime[1]. Diagnosis for prostate cancer historically has led to both over and under treatment—a fairly severe limitation as over diagnosis has significant morbidity implications and under diagnosis can be fatal. The primary tools for diagnosis of prostate cancer are digital rectal examination (DRE), prostate specific antigen (PSA) screening, and transrectal ultrasound (TRUS)-guided biopsies[2–4]. Treatment plans for prostate cancer range from watchful waiting to radical prostatectomy with radiation, indicating the importance and strong impact of an informed diagnosis. With 1 in 39 men dying *of* prostate cancer, and 2.1 million men dying *with* prostate cancer and not from it (CDC), there is an obvious need for powerful diagnostics—and thus the ability to discriminate between the treatment spectrum. However, significant limitations in current diagnostic approaches exist.

In 1986 prostate specific antigen (PSA) screening was introduced for the diagnosis of prostate cancer. From 1986 to 2005 there were an estimated 1.3 million additional men diagnosed with prostate cancer due to PSA, with debatably small to zero mortality benefit[5]. This resulted in the US Preventative Services Task Force (USPSTF) instructing against use of PSA for men 75+. In 2012 the USPSTF advised against the use of PSA for *all* average-risk men in an effort to rectify the severe over-diagnostic consequences from positive PSA screening[4,6,7]. However, some countries claim a significant correlation between PSA and prostate cancer detection[8], and many still use PSA in-spite of the recommendation against[9]. Digital rectal examinations are commonly used in tandem with PSA screening and rely on the presence of palpable tumors. While inexpensive and easy to perform, DREs are limited to detection of only large tumors (thus fairly advanced) and are heavily reliant on the experience of the physician[3]. To date the use of PSA in prostate cancer diagnosis is heavily debated, showing a critical need for additional diagnostic capabilities[3,4,9,10].

Currently, TRUS-guided biopsy is the gold-standard in diagnostics; however, this procedure samples <1% of a standard 25 cm^3 prostate during a 12-core biopsy procedure[11]. Limited tissue volume creates two significant clinical impacts: 1) the rate of false-negatives has been reported as high as 30%[12] and 2) it can be difficult to accurately grade cancer, yet the

Medical Imaging 2018: Biomedical Applications in Molecular, Structural, and Functional Imaging, edited by Barjor Gimi, Andrzej Krol, Proc. of SPIE Vol. 10578, 105781A · © 2018 SPIE
CCC code: 1605-7422/18/$18 · doi: 10.1117/12.2293799

adverse effects from surgery may not justify treatment. Therefore, there is widespread recognition of the need for additional imaging techniques. Magnetic resonance imaging (MRI) is one of the few alternatives used as it has the best soft tissue contrast; however, MRI has extensive capture requirements and very high cost[13,14]. Lastly, computed tomography (CT) has been explored, however, it is normally reserved for very severe cases[3]. It is evident that a device capable of detecting the presence of cancer in real-time to provide improved imaging to the clinician would be an invaluable contribution toward advancing prostate cancer diagnostics.

Bioimpedance (BI) measures the complex resistance of an organic material (e.g. tissue) to current flow, and is widely accepted as safe, low cost and easy to use[15,16]. Due to the vast differences in cellular architecture of benign and malignant tissue, bioimpedance has been shown to be sensitive to the presence of cancer in a variety of applications including tongue[17], breast[18], skin[19], and lung[20]. Specifically, electrical properties of prostate cancer have been reported to be significantly different than benign prostate[21,22]. *We hypothesize that a custom tetrapolar-based electrical impedance sensing biopsy (EIS-Bx) needle will be able to detect the electrical properties of surrounding tissue and provide a "4-bit" image for guidance to potential cancer locations.* Creating a device capable of providing even a coarse spatial map would improve diagnostic guidance, create a new parameter to reduce false-negatives, improve tumor grading, and overcome limitations of current biopsy protocols.

2. METHODS

2.1 Electrical impedance sensing biopsy needle

A custom electrical impedance sensing biopsy needle was designed to investigate the electrical properties of the surrounding prostate tissue during a standard biopsy procedure. Four gold-plated electrode traces were printed on a flexible polyimide circuit and overlaid onto a standard 18-gauge biopsy needle. Medical grade heat shrink was added over the traces to electrically insulate the shaft while leaving four 5 mm x 0.5 mm rectangular electrodes exposed at the needle tip (Figure 1). Additive manufacturing was used to create a custom housing of the circuit on the back end and enable electrical interface to a reusable firing device.

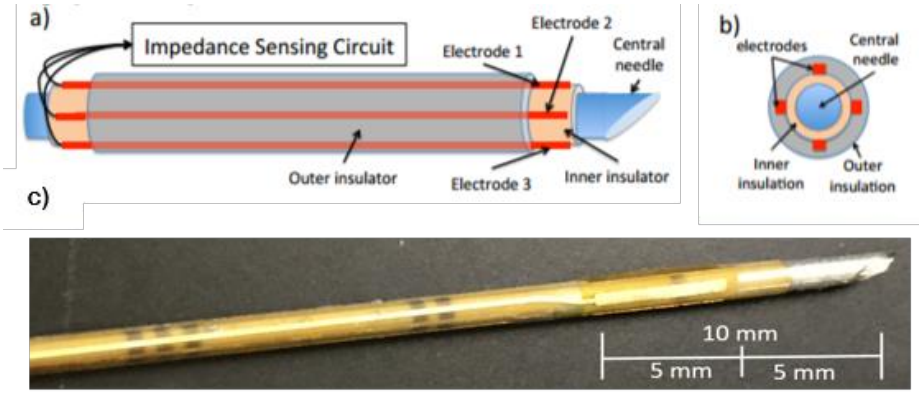

Figure 1 – (a) Diagram of our custom biopsy needle (b) cross-section view of tetrapolar enabled design and insulating layers (c) magnified image of the tip of the physical prototype EIS-Bx. The gold rectangle seen is one electrode

2.2 Small form-factor impedance analyzer

A custom printed circuit board (PCB) was designed to replace an HP4284A benchtop impedance analyzer system used in our previous bipolar needle design[23]. This custom PCB utilizes PSoC5 (CY8C5866, Cypress Semiconductor) and an analog front-end device (AFE4300, Texas Instrument) to record impedance measurements across all electrode configurations (Figure 2). Magnitude impedances are represented as $|Z| = \sqrt{R^2 + X^2}$ where R and X represent the real and imaginary components of the measurement, respectively.

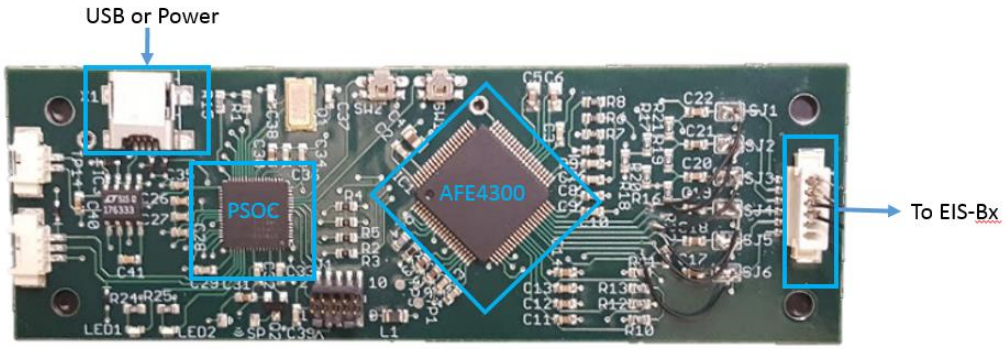

Figure 2 – Image of the custom PCB AFE board used for small form-factor impedance collection.

2.2.1 Benchtop validation

To validate the accuracy and stability of the custom small form-factor impedance analyzer it was characterized across diverse loading conditions, variable contact impedances and validated against the HP4284A benchtop system in saline solutions.

Magnitude impedance was collected at eight frequencies (1 kHz, 5 kHz, 10 kHz, 25 kHz, 64 kHz, 75 kHz, 100 kHz and 125 kHz) across four loads (100 Ω, 200 Ω, 750 Ω and 1000 Ω)—a range which includes values previously observed in prostate. Variable contact impedance, Rc in Figure 3, was simulated with resistance values ranging from 0 to 1 MΩ (0, 10, 50, 100, 500, 1k, 10k, 100k, and 1M Ω) and a load of 200 Ω—a value commonly seen in lab for prostate. The measured load was analyzed for accuracy at each Rc value.

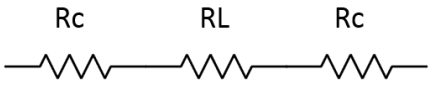

Figure 3 – Series circuit diagram where Rc presents contact resistors and RL load resistors.

Lastly, the EIS-Bx was connected to the benchtop HP4284A impedance analyzer and submerged in saline solutions of conductivities ranging from 0.01 to 1 S/m stepped in decades (once again a range which includes expected *in-vivo* loading conditions[23]) to determine the contact impedance of the device itself. This was then compared to the custom PCB AFE results for verification of performance in likely loading conditions.

2.3 Spatial differentiation experimentation

Electrical impedance was recorded at seven discrete frequencies (1 kHz, 5 kHz, 10 kHz, 25 kHz, 64 kHz, 75 kHz, and 100 kHz) for four electrode configurations. The four electrode configurations consisted of bipolar measurements where two electrodes both drive current (I+ and I-) and record the induced potential difference (V+ and V-). For bipolar measurements the electrodes were grouped into adjacent pairs then rotated around the needle, resulting in four configurations (Figure 4b).

To test the hypothesis of quadrant specific sensitivity, the EIS-Bx was connected to the custom PCB and wired to discrete components in each quadrant. Three RC resistors represented surrounding tissue and one RL resistor represented the heterogeneous inclusion. For a conductive inclusion RC = 400 Ω and RL = 200 Ω, for insulative RC = 100 Ω and RL = 200 Ω. Each quadrant was normalized over its largest value to account for variations in electrode patterns (e.g. distance between + and -). A binary color map was then created with maximum conductivity being denoted as 1 and remaining pixels set to 0 if insulative, or minimum conductivity set to 0 and remaining to 1 for conductive. Additionally, a non-binary color map with full normalized gradation was created to investigate other quadrant trends beyond simply detecting the inclusion in the correct quadrant.

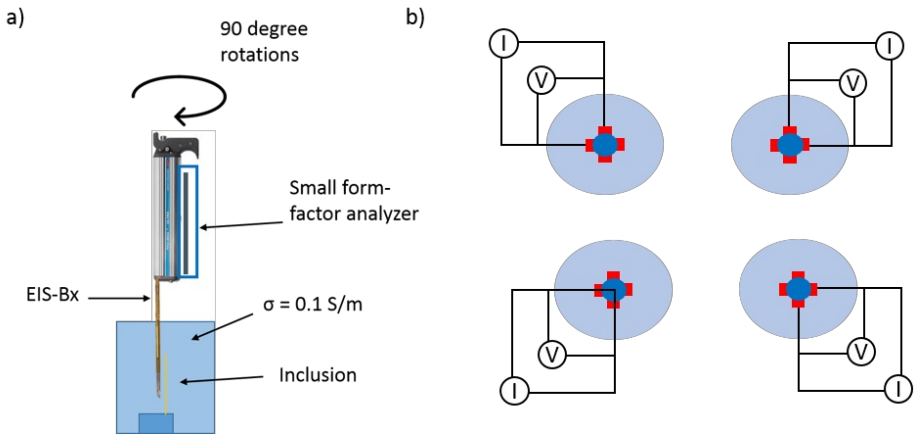

Figure 4 – (a) Experimental phantom setup with EIS-Bx (b) electrode patterns for bipolar measurements where each red square represents one electrode, "I" represents current and "V" the measured potential.

To validate quadrant specific sensitivity in a phantom the EIS-Bx was connected to the custom PCB and placed vertically with the electrodes submerged in a saline bath with conductivity similar to prostate tissue (0.11 S/m)[21]. An insulative inclusion of diameter 700 μm was placed parallel to the needle approximately 500 μm away from the electrodes. The inclusion was rotated in 90-degree increments around the stationary needle with the 4 configurations and 7 frequencies collected at each position (Figure 4a). The impedances of each quadrant were then compared with the location of the inclusion to evaluate potential spatial differentiation. Both binary maps and color maps were created using the same method discussed above for the discrete condition. The procedure was repeated using a conductive inclusion to verify ability to detect a range of conductivity anomalies.

3. RESULTS

Impedance data were successfully acquired from the custom PCB (Figure 2). All data were collected through the AFE with programmed automatic switching between each electrode configuration. Through variation of impedance values it was determined there is both a load dependency and frequency dependency within the measurements (Figure 5a). A look-up-table (LUT) was produced to enable calibrated load measurements using the small form-factor PCB. Additionally, when analyzing contact resistances (Rc in Figure 3), there was a clear cutoff at 500 Ω (Figure 5b). All Rc values lower than this were accurate and all data for Rc values higher unreliable—as is apparent by the steep drop off in the plot. The Rc cutoff was successfully validated by the EIS-Bx in saline solutions. The resistance vs resistivity curve was linear, showing predictable response of the EIS-Bx. The Rc value was calculated across the 20 saline solutions and found to be approximately 12 Ω at 50 kHz, well within the 500 Ω limit.

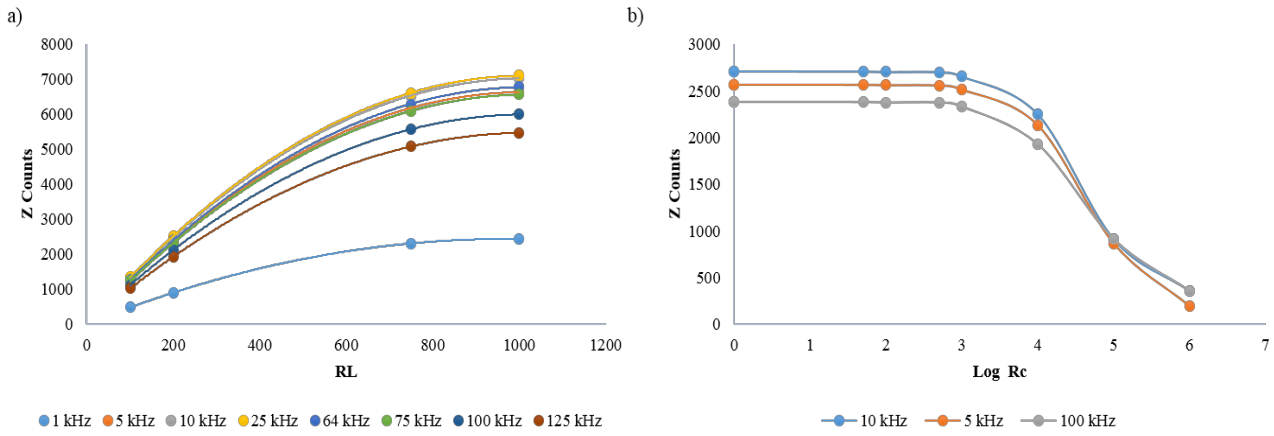

Figure 5 – (a) Impedance (Z) ADC counts vs known load resistance across frequencies (b) Impedance (Z) ADC counts vs varying contact resistances for a 200 Ohm load

For the discrete quadrant sensitivity tests, we would theoretically expect to see impedance increase in the quadrant where the insulative inclusion is present and decrease in the quadrant where the conductive inclusion is present. For a bipolar set of patterns, all measurements follow what would be expected with the highest impedance and lowest impedance present when the insulating or conductive inclusion was closest to those electrodes, respectively (Figures 6 and 7). Additionally, Figure 7 shows consistency across frequency. Color maps are seen to be almost identical to binary maps.

When moving to a more complex saline phantom, inclusion presence was correctly predicted across all quadrants and between conductivities (Figures 8 and 9). The expected trend from the discrete measurements was seen in the phantom with the insulative inclusion resulting in increased impedance and conductive inclusion in reduced impedance. New variability in color maps can be seen in the phantom experiments, which would be expected when compared to discrete components. Maps for both 25 kHz and 100 kHz show consistency across frequency.

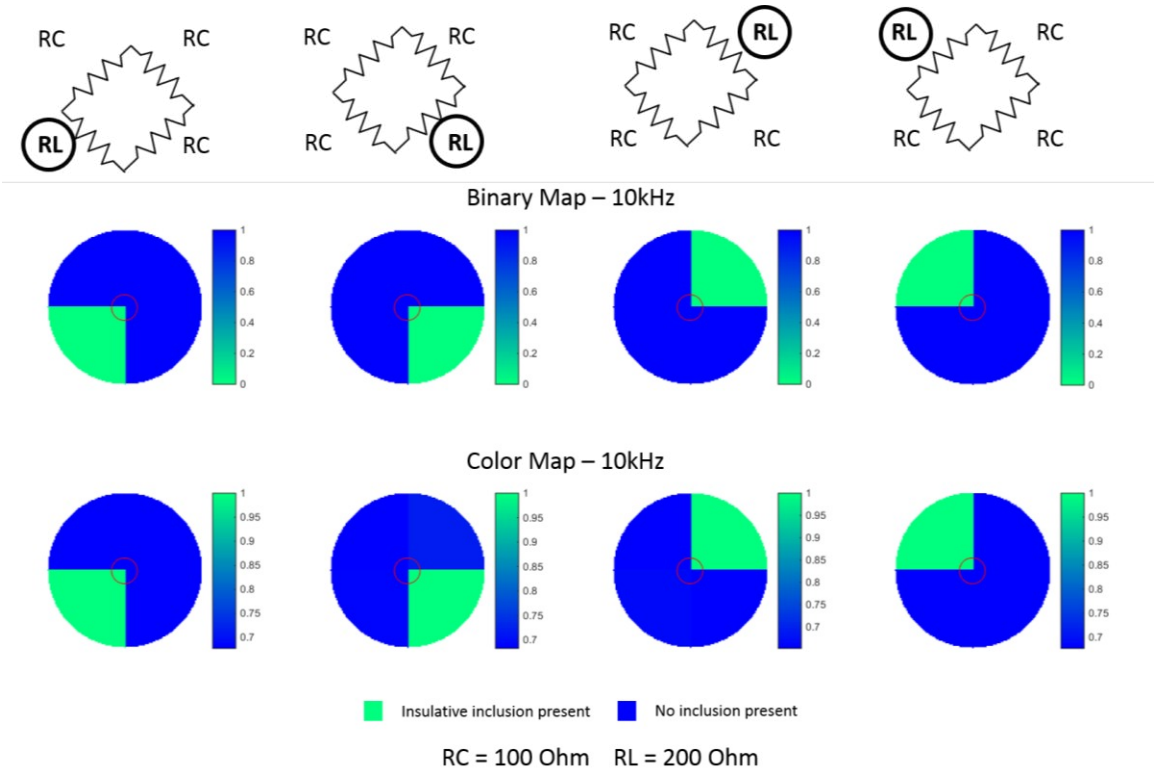

Figure 6 – Discrete insulative component successfully detected in both binary map (second row) and color map (third row) at 10 kHz.

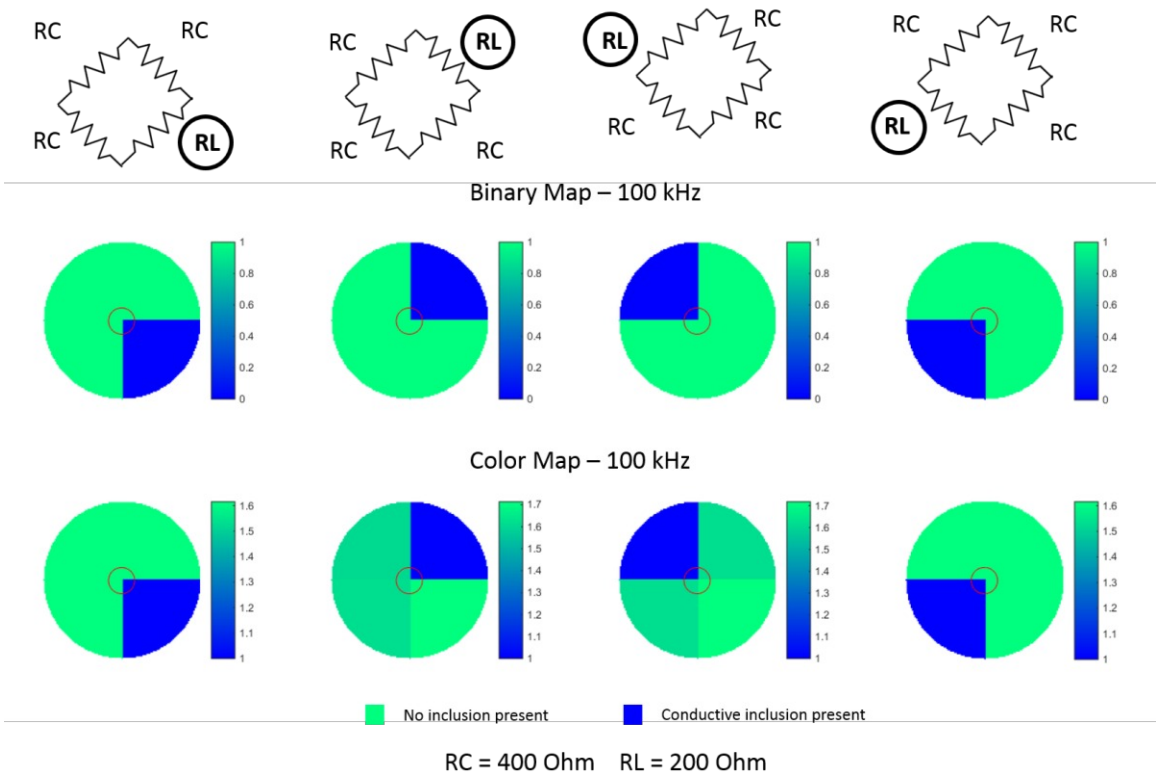

Figure 7 – Discrete conductive component successfully detected in both binary map (second row) and color map (third row) at 100 kHz.

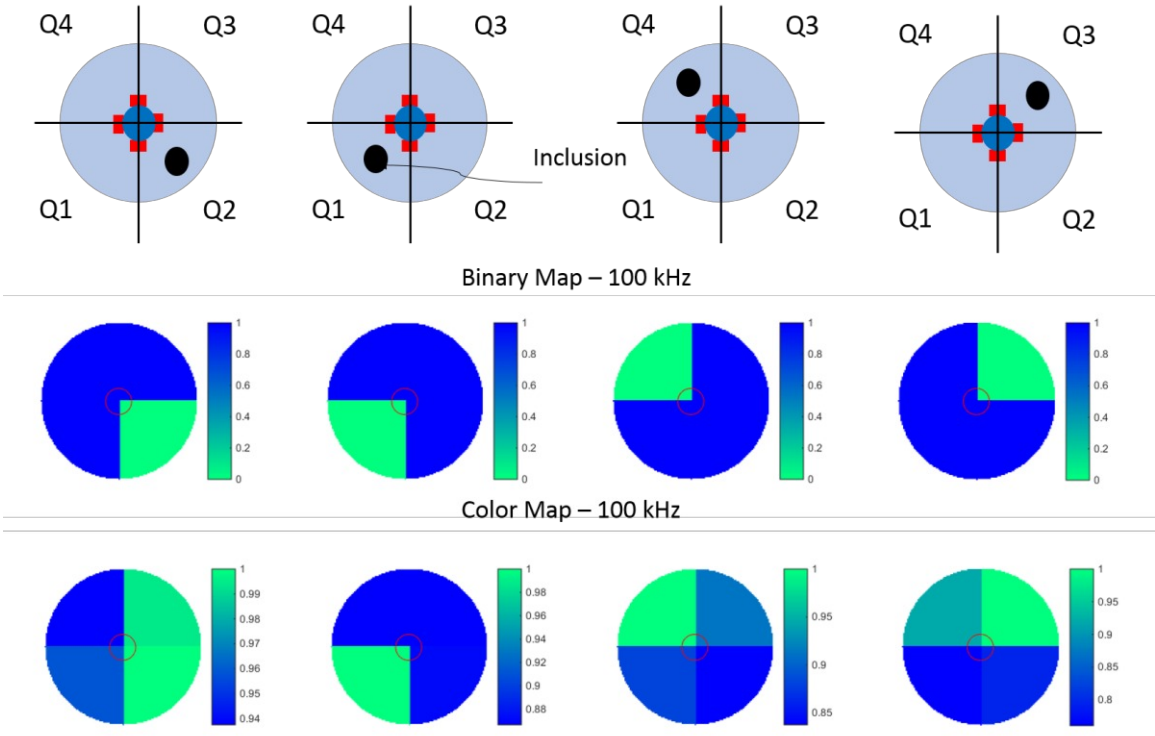

Figure 8 – Phantom with an insulative inclusion shows change of impedance as the inclusion rotates position. Both binary map (second row) and color map (third row) at 100 kHz can be seen here.

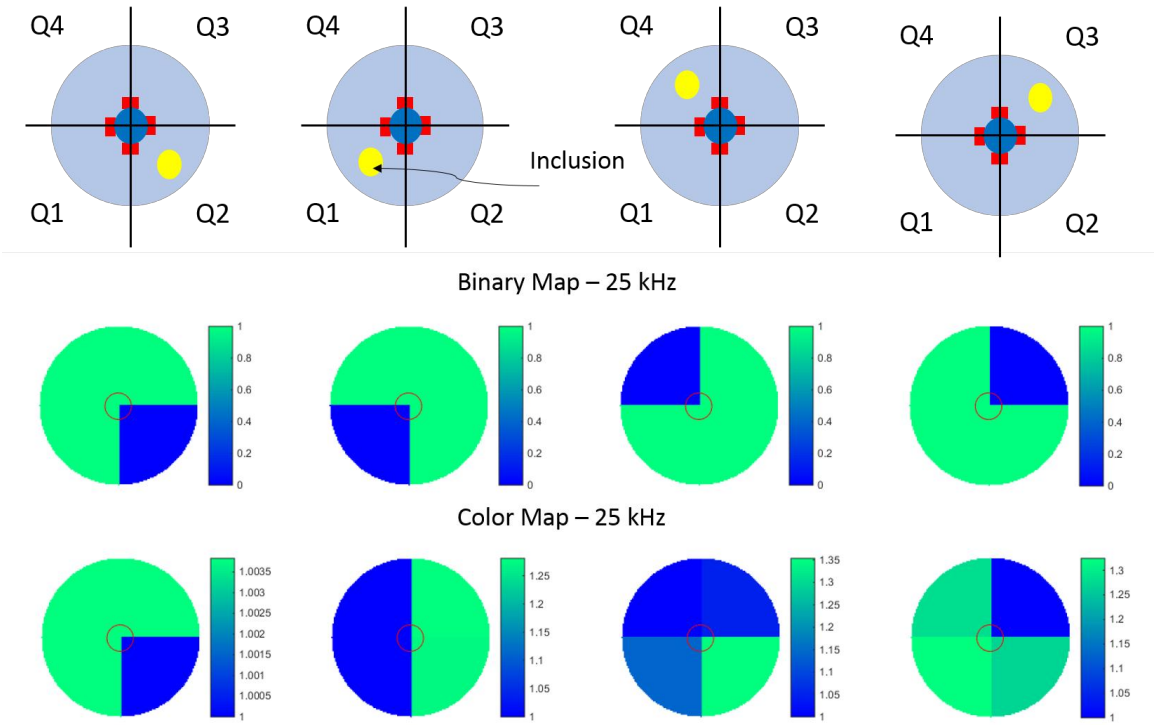

Figure 9 – Phantom with a conductive inclusion shows change of impedance as the inclusion rotates position. Both binary map (second row) and color map (third row) at 25 kHz can be seen here showing consistency across frequency.

Interesting to note is that the gradient color maps show potential sensitivity to a "nearby' inclusion. For example, when the inclusion was in a known quadrant the pixel farthest seems to be the least responsive to the inclusion conductivity. Additionally, the neighboring pixels show a value closer to the conductivity of the inclusion pixel. While this shows the exciting potential for neighboring bipolar spatial sensitivity, the trend was not consistent across all quadrants or all frequencies. We predict this was likely due to the manual control of the rotational stage for the inclusion. Small offsets in inclusion location could drive the pixel-to-pixel variability in a 4-bit impedance measurements. This suggests potential spatial sensitivity beyond an isolated bipolar electrode pair.

4. DISCUSSION

We have demonstrated for the first time an EIS-Bx device that enables real-time spatial sensitivity to a heterogeneous tissue sample surrounding a biopsy needle. Figure 10 shows the four electrodes around the needle and the resulting quadrants between them. By differentiating between measured conductivities of each quadrant we could provide real-time feedback to the clinician during the biopsy procedure. As an example, Figure 10c shows a scenario where green may represent high-likelihood of benign tissue, yellow represent potential risk of disease, and red represent high-suspicion of cancer present.

Real-time spatial impedance information could act as a "4-bit" imaging modality and direct subsequent biopsies to high-risk areas. False-negative biopsy results may be reduced by collecting additional biopsies from the informed image locations. The electrical properties from the surrounding tissue would provide increased information to the clinician for both diagnostics and treatment planning. Since the course of treatment can have a dramatic impact on the quality-of-life of a patient, more informed sampling would potentially enable more accurate diagnosis.

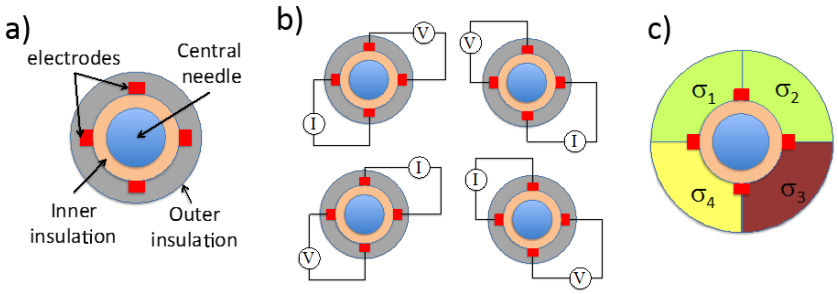

Figure 10 – (a) Cross-sectional view of needle where red squares represent each electrode, (b) tetrapolar electrode configurations for future work (c) potential quadrant specific real-time image provided to surgeon.

Successful implementation of the small form-factor impedance analyzer further demonstrates the feasibility of the EIS-Bx for clinical translation. The previous benchtop impedance analyzer was 50 cm X 70 cm X 15 cm, a significantly large form-factor in a space-constrained surgical setting and a limitation to adoption. By comparison the small form-factor analyzer is 10 cm X 3.25 cm X 1 cm, a size capable of incorporating into a single hand-held device. Furthermore, the characterization of the custom PCB resulted in ideal ranges of operation well within the expected bounds for *in-vivo* prostate applications.

Subsequent work will characterize the conditions of surrounding heterogeneity that the EIS-Bx will be capable of imaging. Increased electrode configurations, specifically tetrapolar measurements (Figure 10b), will be explored and range of degree of spatial sensitivity determined. The EIS-Bx and small form-factor AFE PCB will be used to investigate the device's ability to differentiate cancer from benign tissue in ex-vivo prostate with "4-bit" imaging capabilities.

5. CONCLUSION

A custom electrical impedance sensing biopsy needle could enable real-time investigation of prostate cancer. Further, the four electrodes on the custom needle create the potential to provide the surgeon with quadrant specific spatial information regarding the location of the tumor. Initial experiments show successful spatial sensitivity to a moving inclusion using the EIS-Bx device. A custom PCB was designed and used to gauge electrical properties. The successful implementation of the PCB impedance analyzer is a huge step forward as it allows the device to become fully handheld—which creates higher potential of clinical adoption. Future work will investigate the ability to differentiate cancer from benign tissue ex-vivo with quadrant specific resolution. The development, optimization and analysis of a real-time 4-bit imaging EIS-Bx has the potential to revolutionize diagnosis and treatment of prostate cancer. Our results presented here show the first steps towards realizing this exciting potential.

Acknowledgements

We would like to thank our funding sources NIH 1R41CA192502-01A1 and CDMRP W81XWH-13-1-0127 for their support in this work.

References

1. American Cancer Society. *Cancer Facts & Figures*.; 2016. https://www.cancer.org/content/dam/cancer-org/research/cancer-facts-and-statistics/annual-cancer-facts-and-figures/2016/cancer-facts-and-figures-2016.pdf. Accessed January 13, 2018.
2. Selley S, Donovan J, Faulkner A, Coast J, Gillatt D. Diagnosis, management and screening of early localised prostate cancer. *Health Technol Assess*. 1997;1(2):i, 1-96. http://www.ncbi.nlm.nih.gov/pubmed/9414541. Accessed January 12, 2018.
3. McClure P, Elnakib A, El-Ghar MA, et al. In-Vitro and In-Vivo Diagnostic Techniques for Prostate Cancer: A Review. *J Biomed Nanotechnol*. 2014;10(10):2747-2777. doi:10.1166/jbn.2014.1990.
4. Heidenreich A, Bastian PJ, Bellmunt J, et al. EAU Guidelines on Prostate Cancer. Part 1: Screening, Diagnosis, and Local Treatment with Curative Intent—Update 2013. *Eur Urol*. 2014;65(1):124-137. doi:10.1016/J.EURURO.2013.09.046.

5. Welch HG, Albertsen PC. Prostate Cancer Diagnosis and Treatment After the Introduction of Prostate-Specific Antigen Screening: 1986-2005. *JNCI J Natl Cancer Inst*. 2009;101(19):1325-1329. doi:10.1093/jnci/djp278.

6. Hayes JH, Barry MJ. Screening for Prostate Cancer With the Prostate-Specific Antigen Test. *JAMA*. 2014;311(11):1143. doi:10.1001/jama.2014.2085.

7. Jemal A, Fedewa SA, Ma J, et al. Prostate Cancer Incidence and PSA Testing Patterns in Relation to USPSTF Screening Recommendations. *JAMA*. 2015;314(19):2054. doi:10.1001/jama.2015.14905.

8. Drummond FJ, Carsin A-E, Sharp L, Comber H. Trends in prostate specific antigen testing in Ireland: lessons from a country without guidelines. *Ir J Med Sci*. 2010;179(1):43-49. doi:10.1007/s11845-009-0376-7.

9. Bell KJL, Del Mar C, Wright G, Dickinson J, Glasziou P. Prevalence of incidental prostate cancer: A systematic review of autopsy studies. *Int J cancer*. 2015;137(7):1749-1757. doi:10.1002/ijc.29538.

10. Dimakakos A, Armakolas A, Koutsilieris M. Novel tools for prostate cancer prognosis, diagnosis, and follow-up. *Biomed Res Int*. 2014;2014:890697. doi:10.1155/2014/890697.

11. Harnden P, Naylor B, Shelley MD, Clements H, Coles B, Mason MD. The clinical management of patients with a small volume of prostatic cancer on biopsy: What are the risks of progression? *Cancer*. 2008;112(5):971-981. doi:10.1002/cncr.23277.

12. Serefoglu EC, Altinova S, Ugras NS, Akincioglu E, Asil E, Balbay MD. How reliable is 12-core prostate biopsy procedure in the detection of prostate cancer? *Can Urol Assoc J*. 2013;7(5-6):E293-8. doi:10.5489/cuaj.11224.

13. Fuchsjäger M, Shukla-Dave A, Akin O, Barentsz J, Hricak H. Prostate cancer imaging. *Acta radiol*. 2008;49(1):107-120. doi:10.1080/02841850701545821.

14. Hricak H, Choyke PL, Eberhardt SC, Leibel SA, Scardino PT. Imaging Prostate Cancer: A Multidisciplinary Perspective. *Radiology*. 2007;243(1):28-53. doi:10.1148/radiol.2431030580.

15. Mulasi U, Kuchnia AJ, Cole AJ, Earthman CP. Bioimpedance at the Bedside. *Nutr Clin Pract*. 2015;30(2):180-193. doi:10.1177/0884533614568155.

16. Khalil SF, Mohktar MS, Ibrahim F. The theory and fundamentals of bioimpedance analysis in clinical status monitoring and diagnosis of diseases. *Sensors (Basel)*. 2014;14(6):10895-10928. doi:10.3390/s140610895.

17. Sun T-P, Ching CT-S, Cheng C-S, et al. The use of bioimpedance in the detection/screening of tongue cancer. *Cancer Epidemiol*. 2010;34(2):207-211. doi:10.1016/J.CANEP.2009.12.017.

18. Morimoto T, Kinouchi Y, Iritani T, et al. Measurement of the Electrical Bio-Impedance of Breast Tumors. *Eur Surg Res*. 1990;22(2):86-92. doi:10.1159/000129087.

19. Aberg P, Nicander I, Hansson J, Geladi P, Holmgren U, Ollmar S. Skin Cancer Identification Using Multifrequency Electrical Impedance—A Potential Screening Tool. *IEEE Trans Biomed Eng*. 2004;51(12):2097-2102. doi:10.1109/TBME.2004.836523.

20. Kimura S, Morimoto T, Uyama T, Monden Y, Kinouchi Y, Iritani T. Application of Electrical Impedance Analysis for Diagnosis of a Pulmonary Mass. *Chest*. 1994;105(6):1679-1682. doi:10.1378/CHEST.105.6.1679.

21. Halter RJ, Schned A, Heaney J, Hartov A, Schutz S, Paulsen KD. Electrical Impedance Spectroscopy of Benign and Malignant Prostatic Tissues. *J Urol*. 2008;179(4):1580-1586. doi:10.1016/j.juro.2007.11.043.

22. Khan S, Mahara A, Hyams ES, Schned AR, Halter RJ. Prostate Cancer Detection Using Composite Impedance Metric. *IEEE Trans Med Imaging*. 2016;35(12):2513-2523. doi:10.1109/TMI.2016.2578939.

23. Mishra V, Bouayad H, Schned A, Hartov A, Heaney J, Halter RJ. A Real-Time Electrical Impedance Sensing Biopsy Needle. *IEEE Trans Biomed Eng*. 2012;59(12):3327-3336. doi:10.1109/TBME.2012.2213599.